Delft University of Technology

Experimental investigation of overflowing over river groyne exposed to primary ship-induced waves

Master of Science Thesis

T.V. van Batenburg

TU Delft

BAW
Bundesanstalt für Wasserbau

Deltares

Experimental investigation of overflowing over river groyne exposed to primary ship-induced waves

Master of Science Thesis

by

T.V. van Batenburg

in partial fulfilment of the degree of Master of Science
at the Delft University of Technology,
defended publicly on Wednesday 11 October, 2023 at 14:00.

Student number:	4578929	
Project duration:	November 1, 2022 – October 11, 2023	
Thesis committee:	Dr. ir. B. Hofland	TU Delft, chair committee
	Dr. ir. S. Memar	TU Delft, daily supervisor
	Dr. ir. O. Morales Napoles	TU Delft, supervisor
	Dr. A. alYousif	Kuwait University, supervisor
	Dr. ir. G. Melling	Bundesanstalt für Wasserbau, supervisor
	ir. W. Bakker	Deltares, supervisor
	Prof. Dr. ir. M van Gent	TU Delft, supervisor

An electronic version of this thesis is available at http://repository.tudelft.nl/.
Cover: Groynes in Lower Elbe Estuary, Germany (BAW, 2019).

TUDelft

Preface

This is the Master's thesis 'Experimental investigation of overflowing over river groyne exposed to primary ship-induced waves' of Tobias van Batenburg. It has been written to fulfil the requirements for the degree of Master of Science in Hydraulic Engineering at the Civil Engineering Faculty of the Delft University of Technology. This thesis was made possible by the Bundesanstalt für Wasserbau and includes physical modelling experiments performed at the Hydraulic Engineering Laboratory at the Delft University of Technology.

This thesis would not have been possible without the support and guidance of the seven supervisors in my thesis committee, to whom I would like to express my gratitude. First of all, I would like to thank Bas Hofland for putting me in touch with Sargol Memar after an oral exam in one of his courses, for chairing my thesis committee, and for your important input during the meetings. Prior to that exam, I didn't expect to find a topic for a Master's thesis. Sargol Memar introduced me to the world of hydraulic experiments and guided me through this thesis as my daily supervisor, for which I am very grateful. During the flow experiment, I worked with guest researcher Ahmad AlYousif from Kuwait University. We spent some long days in the lab to ensure accurate measurements and produce reliable results. Thank you Ahmad for this fruitful collaboration.

Furthermore, I would also like to thank Wout Bakker, a researcher at Deltares who developed the PIV setup used during the flow experiments. His guidance during this experiment was particularly helpful and it wouldn't have been possible without him. Moreover, I would also like to thank you for introducing me to Deltares and allowing me to present this thesis to your research group.

Next, I would like to express my gratitude to Oswaldo Morales Napoles, Gregor Melling and Marcel van Gent for being part of my thesis committee and guiding me throughout the thesis process. Furthermore, I would also like to thank Jennifer Rodriguez for manually controlling the reflection during the damage experiment. And finally, I would like to thank everyone who somehow helped (constructing the physical models, providing assistance, discussing results, etc.) throughout this 10-month journey. Without your contributions, the completion of this work wouldn't have been possible.

T.V. van Batenburg
Delft, September 2023

Summary

Groynes in the Lower Elbe estuary in Germany are subject to attack from overflowing long-period primary ship-induced waves. Damage can occur on the crest and lee side of the structure due to the high turbulent overflowing flow velocities. The Bundesanstalt für Wasserbau (BAW) constructed two different groyne designs based on local experience and due trial and error. One showed minor erosion, whereas the other groyne showed large areas of erosion. Although one of the two new groynes showed a good response against erosion, an actual design tool (probabilistically or deterministically) is not yet present. Therefore, experimental research is performed to determine a relationship between the damages and corresponding overflowing primary ship waves, which can be used as a design tool.

The experimental campaign is divided into two separate experiments: the flow experiment and the damage experiment. Due to the long-period characteristics and the relatively shallow water at the prototype groyne, the overflowing wave can be described as a quasi-steady flow. This approximation implies that the flow can be modelled as a steady free overflow. These conditions represent the maximum flow velocities for a wave with the same wave height as the tested free-flow water level and were used during the flow experiment. During the damage experiment, long-period ship waves were simulated because the duration of the maximum overflow velocity is expected to be related to the amount of damage to the structure.

During the flow experiments, four physical models were tested and scaled according to Froude with a scaling ratio of 13. The models differ in slope (Θ = 1:3 and 1:4) and armour rock diameter (d_{n50} = 0.013m and 0.019m). All models had an impermeable core, a fixed filter and an armour layer with thicknesses of 1 and 2 rock diameters respectively. Four overflowing water levels based on the hydraulic head at the crest (h) were tested without an initial preset lee side water level resulting in supercritical flow conditions. Measurements were conducted using Particle Image Velocimetry. Velocity fields were obtained from the crest to 70% of the lee side slope measured from the crest. This resulted in a dimensionless depth-averaged flow velocity equation, in which the flow velocity (U) is positioned at the theoretical assumed freeboard level (R_c) on the lee side slope and can be used for supercritical flow.

$$U/\sqrt{(gh)} = 1.95 - 0.88exp(-0.51\Theta R_c/d_{n50}) \tag{1}$$

During the damage experiment, the damage due to overflowing waves was measured at the crest and lee side using Structure from Motion principles. A physical model with dimensions based on the prototype groyne was tested for a scaling ratio of 13. The rock material used is basalt with a rock diameter of d_{n50} = 0.019m on a slope (Θ) of 1:4. The core of the structure is impermeable with a single filter layer and an armour layer of two rock diameters thick. The damage parameters S, E_{2D} and E_{3D} were measured for single overflowing waves. Different wave heights and lee side freeboard values were tested. This led to the observation that damage increases significantly with increasing lee side freeboard. An increase in damage was also observed with increasing wave height, although this effect was smaller than the effect of increasing the freeboard.

The corresponding damage limits for overflowing long-period waves on the lee side of a groyne structure with a 2 d$_{n50}$ thick rock layer, are presented in Table 1. The damage limits are described as initial, intermediate and failure. These are defined as respectively a 1 d$_{n50}$ wide hole of 1 d$_{n50}$, 1.5 d$_{n50}$ and nd$_{n50}$ deep. Here, n is the number of rock layers in the armour layer.

Table 1: Damage limits at lee side of rubble mound structure for overflowing long period waves

Damage concepts	**E$_{3D,1}$**	**S** $(\mu \pm 2\sigma)$	**E$_{2D}$** $(\mu \pm 2\sigma)$	**E$_{3D,5}$** $(\mu \pm 2\sigma)$
Damage initiation	1.0	1 ± 0.9	0.2 ± 0.1	0.3 ± 0.2
Intermediate damage	1.5	4 ± 0.9	0.4 ± 0.1	0.7 ± 0.2
Failure	2.0	9 ± 0.9	0.9 ± 0.1	1.2 ± 0.2

The dimensionless flow velocity equation describes the flow along the lee side structure for supercritical free-flow conditions. As the overflowing primary ship waves are quasi-steady, the measured flow velocities for continuous free flow represent the maximum flow velocities of an overflowing wave. Therefore, the damage due to overflowing waves can be expressed in terms of flow velocities measured during the flow experiment. These maximum flow velocities are expected to cause the most damage to the structure. Most damage occurs mainly around the lee side freeboard level. Only at small freeboard levels in combination with wave heights larger than measured at the prototype, the maximum erosion is positioned significantly lower than the freeboard water level. As a result, the damage parameters S, E$_{2D}$ and E$_{3D,5}$ are expressed by the measured super-critical flow velocities at the freeboard levels expressed by the dimensionless flow equation. The dimensionless flow equation is in this case rewritten in dimensional form. It is recommended to express the damage to the structure in the E$_{3D,5}$ parameter. This parameter presents the actual erosion and the damage limits are similar to wind wave loads. Therefore, this parameter can be applied in a more general manner without the risk of errors by determining the damage levels of a groyne exposed to wind or overflowing primary ship waves.

$$E_{3D,5} = 3.4 * 10^{-2} * \left(\frac{U(z_{max}, R_c, \Theta, d_{n50})}{\sqrt{\Delta g d_{n50} K_s}} \right)^{3.2} \tag{2}$$

This damage equation describes the damages due to overflowing when the overflow is in supercritical conditions. For subcritical conditions, the damage equation can be used as a design tool for the construction of groynes exposed to overflowing waves which the quasi-steady approximation can describe. The flow velocities expressed by the dimensionless flow equation are based on supercritical conditions and are therefore the maximum occurring flow velocities. Supercritical conditions could occur when the lee side freeboard levels are significant. Based on the prototype, these supercritical conditions are relatively rare compared to subcritical conditions, which indicates that this damage equation is a conservative but safe approach when used as a design equation. In case it is known that the overflowing at a structure is in supercritical condition or when the effects of supercritical conditions are studied, the damage equation as well as the dimensionless flow equation can also be used in a probabilistic manner.

Contents

1

Introduction

This introduction outlines the reasoning behind the start of the experimental investigation on the overflowing flow velocities and damage at groynes exposed to primary ship wave loadings. Section 1.1 starts with the motivation for the research and presents the background and problem description. This is followed by Section 1.2 Research objectives, Section 1.3 Research methodology and Section 1.4 Research Scope. The final Section 1.5 presents the structure of the report.

1.1. Motivation for the research

In the last two decades, there has been a rise in damage to groynes and training walls covered with rip-rap in the Lower Elbe Estuary. This damage is attributed to long-period waves caused by ships that overflow the structures (Melling et al., 2020). The cause of this trend is the growing size of ships navigating the river, particularly the New Panamax and Ultra Large Container Vessels. Consequently, it is expected that primary ship waves will continue to increase. This results in greater wave loads and an elevated risk of damage to rock structures. This report focuses on the physical modelling of a prototype river groyne structure situated in the Lower Elbe Estuary. The study aims to assess the overflowing phenomenon, determine the damage caused to the groyne and express these into a design tool.

1.1.1. Background

A river groyne is a man-made structure that is designed to protect the riverbanks from erosion, maintain water level by deflecting flow directions, and ensure navigation safety (Xiang et al. (2020), Ahmad et al. (2010),Uijttewaal (2005)). It is built perpendicular to the riverbank and is usually made of materials such as rock, concrete or wood. Generally, these groynes are only subjected to loads due to flow velocities around the structure or small waves interacting with the sides. Without a groyne structure, these loads could result in large drag forces that cause erosion at the river bed and banks. This could lead to the failure of the riverbanks, resulting in a risk to the surrounding area. By constructing a groyne structure perpendicular to the flow direction, the effective cross-section of the water body becomes smaller. This results in a reduction of the flow velocities directly behind the structure. The main flow in the river is kept at a distance from the banks and erosion is therefore reduced or even prevented (Krishna et al., 2016).

Figure 1.1: River groynes perpendicular along the Lower Elbe Estuary in Germany (Melling et al., 2020)

As the main flow is kept at a distance, the velocity of the flow increases in the centre of the river. Consequently, erosion rates in the middle of the river increase, resulting in a deeper channel. Therefore, groyne structures are also used to control the channel depth in navigation channels (Malik & Pal, 2019).

As stated, the groynes in the Lower Elbe Estuary are experiencing damage and deformations. The Bundesanstalt für Wasserbau (BAW) did a study into the cause of the damages to the groyne structures in the Lower Elbe Estuary, which demonstrated that these were mainly caused by the long-period ship wave loadings BAW (2010). The period of stern wave to bow wave (T_{Hp}) ranges from 60 seconds to 120 seconds. The primary waves propagate toward the shore and cause an overflowing over the groynes, leading to damage to the crest and lee side of the groyne structures.

These primary waves are generated by the vessels sailing through the estuary. This estuary is located in the northern part of Germany and connects the Wadden Sea to the Port of Hamburg and is therefore heavily used by large dimensioned container vessels such as Ultra Large Container Vessels (ULCV) of the New Panamax and Triple E categories. These vessel dimensions are relatively new and are expected to increase even further, resulting in potentially larger wave loadings to the groynes.

Figure 1.2-left illustrates primary and secondary wave systems for ships sailing in narrow and shallow waterways. The primary wave systems consist of the bow wave, drawdown and stern wave, marked by 1, 2 and 3 in the figure. Furthermore, the time between maximum primary wave height (H_s) and maximum drawdown (z_a) is presented as T_{ST}. The pictures on the right side represent the interaction of the ship wave with the groyne in the Elbe estuary at three time moments. Picture A was taken when there was no interaction between waves and the groyne, picture B shows the exposed groyne during the drawdown and picture C depicts the maximum overflowing caused by the stern wave. The damage at the groyne is caused by this overflowing flow and is observed at the crest and lee side (non-wave-facing side) of the groyne.

To reduce these damages to the groynes, different measures were taken by the BAW. These included shallower slope angles, smaller crest widths, wider groyne root areas and smoother revetment transitions (WSABhv (2021), WSACux (2009), Melling et al. (2020)). This led to the construction of two new configurations of the groynes to observe their response to the loading that caused the damage. One of these groynes had a recessed root and was resistant to the primary ship-induced wave loading and no severe damage has been observed. The other groyne had a large radius root and was destroyed under the same conditions (Melling et al., 2020). However, despite the implementation of these measures and the fact that one of the new groyne designs has remained stable, the present design knowledge is based on local experience and due to trial and error. Actual design tools (probabilistically nor deterministically) to design groynes against overflowing primary waves are still not present.

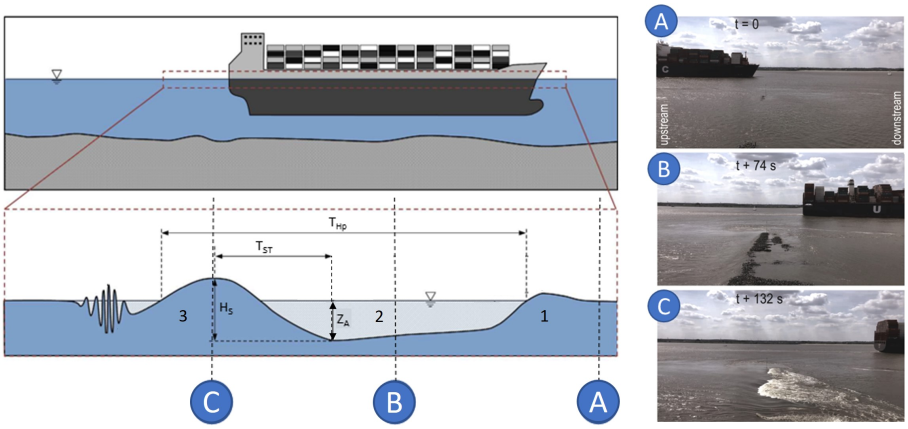

Figure 1.2: Schematic illustration of the ship-generated wave system in narrow shallow water interacting with groyne (modified from Melling et al., 2020)

1.1.2. Problem description

The overflowing due to the long period primary ship induced waves are the cause of damage to the lee side of the groyne structures. The two different groyne designs in the Lower Elbe Estuary were constructed based on local experience and trial and error. Probabilistic or deterministic design tools are not present yet.

During the field measurements at the groynes at the Lower Elbe, pressure sensors were placed at the head, foot, root and crest areas of the groynes. Unfortunately, no measuring devices could be placed on the lee side of the structures. As a result, flow velocities or water levels on the lee side of the groyne are unknown. However, these flow velocities are expected to cause the damage occurring on the lee side.

As part of the same study, a damage assessment was carried out and showed that one of the new groyne designs had only minor eroded areas. As this groyne is located in the estuary, it is difficult to determine which combination of long-period wave height, the corresponding overflowing velocity and the lee side water level is critical for the groyne design. Therefore, the BAW and the Delft University of Technology collaborated to define a relation to determine the damage on the lee side of the groyne due to overflowing as a consequence of long-period primary ship-induced waves, which can be used as a design tool.

1.2. Research objectives

The knowledge gaps identified in the previous section show the demand for the research carried out in this thesis. Hence, the main objectives of this research are:

- Flow velocity measurements at the lee side of a groyne exposed to long-period primary ship-induced wave loadings via physical modelling.
- Damage assessment at the crest and lee side of a groyne exposed to long-period ship-induced wave loadings via physical modelling.

Experiments are conducted in the Hydraulic Laboratory of the Delft University of Technology. Physical models of the groyne with minor erosion are tested. Overflowing velocity and damage at the lee side and crest due to ship-induced primary wave loadings are investigated and are related to each other. The corresponding main research question and sub-questions are as follows:

Main research question

How can the overflowing velocity at the lee side of a groyne structure and the corresponding damage caused by primary ship-induced wave loadings be determined?

Sub-questions

1. How could a Particle Image Velocimetry (PIV) setup be applied to measure the flow velocity at the lee side of the groyne?
2. How could the flow velocity at the lee side of a groyne structure be expressed in a mathematical equation under free flow conditions?
3. How could the damage due to groyne overflowing caused by long-period primary ship wave loadings be expressed in terms of damage parameters S, E_{2D} and E_{3D}?
4. How to characterize damage limits (initial damage, intermediate damage, and failure) for groynes exposed to long-period primary ship wave loadings in shallow and confined waterways?
5. How could the overflow velocity equation be linked to the damage profile at the crest and lee side for a groyne exposed to primary ship wave loadings?

1.3. Research methodology

The research objectives and corresponding questions are answered via physical modelling. The wave-structure interaction can be schematised as shown in Figure 1.3a and all important corresponding parameters are presented in Table 1.1. Since the overflow velocity and the damage are two different phenomena, two experimental setups were prepared. The first part of the experiments is performed to measure the flow velocities, called the 'Flow experiment'. During this experiment, the flow velocities are measured using Particle Image Velocimetry. The second part of the experiment is conducted to measure the occurring damage called the 'Damage experiment'. Structure from Motion principle is used to measure the damage.

The long-period primary ship waves can be approximated using the quasi-steady approximation due to their long wave period characteristics in shallow water depths. Although the flow is unsteady throughout the entire primary wave period, the flow variations are insignificant within a small time step. Therefore, the force of inertia within the wave is minimal and the flow instantly adjusts to the upstream and downstream boundary conditions. As a result, the maximum flow velocities in an overflowing wave are approximately equivalent to the flow velocities of a constant water level with the same height as the maximum height of a long-period wave. The Flow experiment re-creates maximum flow velocities through free-flow conditions and a fixed water level on the wave-facing side, which mimics those of an overflowing primary ship wave with the same wave height. No initial lee side water level is present. Flow velocities are measured at the position where the lee side free-board level would have been at the lee side slope during the Damage experiment. This is presented in Figure 1.3b.

The Damage experiments, on the other hand, are carried out by generating the primary ship waves with an initial lee side water level. No constant free flow is used because the level of damage is expected to be related to the duration of the overflowing. This is presented in Figure 1.3c.

a) Long-period wave – structure interaction

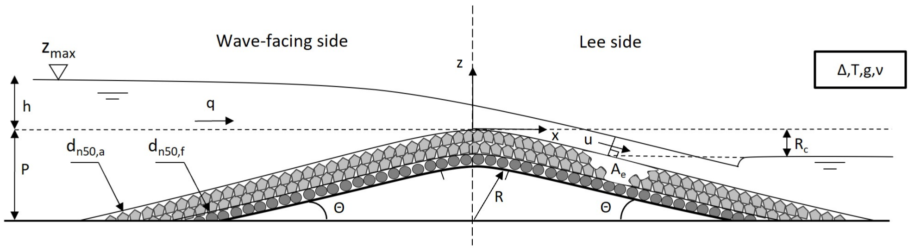

b) Flow experiment

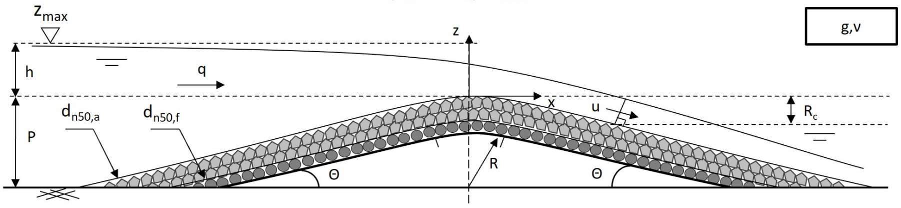

c) Damage experiment

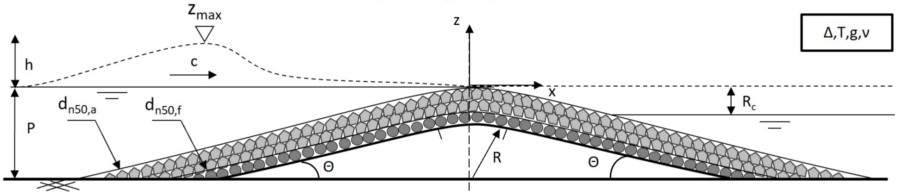

Figure 1.3: a) Schematic representation of overflowing long-period wave and groyne interaction. b) Flow experiments for continuous free flow conditions. c) Damage experiments by generating overflowing long-period waves.

Table 1.1: Most important parameters during overflowing long period primary ship waves.

Parameter	Description
h	Upstream water level above crest level [m]
P	Groyne height [m]
$d_{n50,a}$	Nominal rock diameter of armour layer [m]
$d_{n50,f}$	Nominal rock diameter of filter layer [m]
q	Specific discharge [m/s^2]
Θ	Slope [-]
R	Radius crest [m]
u	Flow velocity along lee side [m/s]
A_e	Damage area [m^2]
R_c	Freeboard due to ship drawdown [m]
z_{max}	Maximum water level above crest level [m]
Δ	$\frac{\rho_s-\rho_w}{\rho_w}$ Specific density [-]
T	Wave period [s]
ρ_s	Rock density [kg/m^3]
ρ_w	Water density [kg/m^3]
ν	Kinematic viscosity [m^2/s]

This experimental study consists of four main sections: literature review, experimental tests, results, and conclusion.

Part I: Literature study - The initial stage of the study is a literature review to present the state of the research. The physics of primary ship waves is presented. Next, the literature covers flow velocity investigations at rock structures with a downward slope, as well as damage parameters and damage limits for rubble mound structures.

Part II: Experimental tests - In this section, the experimental setups and tested conditions are outlined. The prototype groyne's geometry is introduced, followed by the flow velocity equations that are going to be used. Afterwards, Particle Image Velocimetry and Structure from Motion measuring techniques are introduced. This is followed by introducing the physical models and the corresponding experimental setups. This part addresses the answer to sub-research question 1.

Part III: Results - The third section involves analysing the results of the two types of experiments. The results of the flow velocity experiments yield an equation for velocity measurements at the lee side of the groyne and address sub-question 2. The damage experiment results are utilized to answer the research's sub-questions 3 and 4.

Part IV: Interpretation of results - The interpretation of the results forms the final part. Here, the determined flow velocity equation is linked to the damage measurements. This section addresses the answer to the research sub-question 5. The relation between damage and the corresponding flow velocities is shown.

1.4. Research scope

As outlined in the Research objective in Section 1.2, a physical model is designed based on the prototype groyne structure situated at the Lower Elbe Estuary, for which no significant damage has been observed so far. However, for the flow experiments, various dimensions of the model are modified, resulting in a universal flow velocity equation for groynes. In contrast, for the damage experiment, one physical model which is based on the prototype groyne was tested. This research focuses on the effect of the groyne overflowing velocities due to primary long-period ship waves. The physical model's core will be impervious to accurately reflect the maximum flow velocity and damage that occurs at the armour layer. This approach excludes internal pressures during a passing wave, and all damages will be determined for a single wave period.

1.5. Report structure

The structure of this report is presented below and schematically shown in Figure 1.4. In addition, a brief summary per chapter is given.

Chapter 1: Introduction This chapter introduces the problem providing background information, research objectives and questions, methodology and an overview of the report's structure.

Chapter 2: Literature review This chapter describes the current knowledge on the basics of primary ship wave systems, flow velocity equations for downward-sloped structures, damage parameters, characterization limits for rubble mound structures and essential aspects of physical modelling.

Chapter 3: Physical modelling: Theory This chapter presents the relevant parameters of the prototype groyne, describes the corresponding hydraulic conditions at the prototype, outlines the derived flow velocity equation to be used and explains the important aspect of measuring techniques to be used for the experiments.

Chapter 4: Physical modelling: Experiments The chapter outlines the dimensions of the physical model and the experimental setups, including the tested hydraulic conditions.

Chapter 5: Flow velocity experiments results The results of the flow velocity experiment are analysed. The flow velocity equations are compared with the literature.

Chapter 6: Damage experiments results The results of the damage experiments are analysed. The measurements are expressed in the damage parameters and the damage limits are determined.

Chapter 7: Flow velocity and damage interpretation The resulting damage during the damage experiment is connected to the determined flow velocity equation during the flow experiments. This results in an equation expressing the damage due to the overflowing velocities for different wave heights, lee side freeboard levels and geometry of the structure.

Chapter 8: Conclusion and recommendations The final chapter provides the overall conclusions of the research, summarizes the answers to the sub-questions, and addresses the main research question. The final section of the chapter provides recommendations for future research.

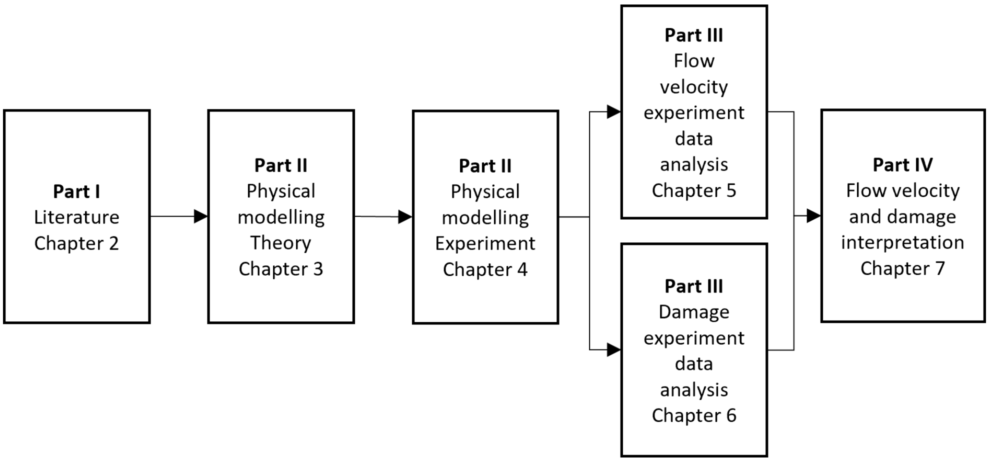

Figure 1.4: Outline of the structure of the report and chapters

2

Literature

This chapter presents the literature review to identify the knowledge gaps. Section 2.1 starts with an introduction to primary ship waves. Section 2.2 presents the existing knowledge of overflowing velocities. This is followed by Section 2.3 which presents the knowledge on damage measurements for rubble mound structures. The chapter ends with Section 2.4, which presents the physical modelling guidelines.

2.1. Primary induced ship wave systems

2.1.1. Ship - waves systems

When a ship moves through the water, the resistance of the hull creates disturbances in the water level consisting of primary and secondary waves (Bertram, 2011). The primary wave system includes a bow wave in front of the ship, a stern wave behind and a drawdown wave along the ship in between the two waves. The primary wave system can be explained as the result of the ship pushing water in front of itself while moving forward (Bhowmik et al., 1981). This pushing results first in the bow wave in front of the ship. The pushed water must return along the sides and under the ship to compensate for the drop in water level, resulting in an increase in velocities. The higher velocity near the ship creates a hydrodynamic pressure field that results in a drop in the water level along and away from the ship's hull, referred to as drawdown. For smaller cross-sections, the velocities and therefore the drop in water level are enhanced. When the ship has passed, the drawdown is compensated by the stern wave. Figure 2.1 illustrates a side view of a passing ship and the generated ship wave systems around the ship's hull. Point 1 indicates the bow wave in front of the ship, followed by the drawdown along the ship's hull marked by point 2 and point 3 indicates the stern wave. Point 4 presents the secondary waves.

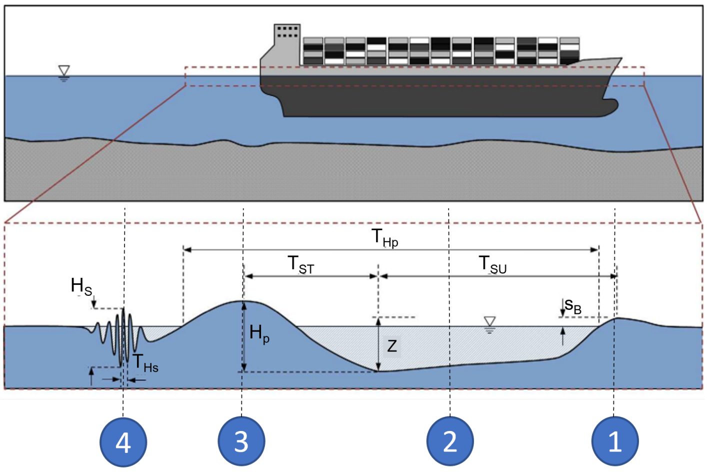

Figure 2.1: Side view of the primary wave system (1,2,3) and secondary wave (4) of a vessel, modified from Melling et al., 2020.

Table 2.1: Important parameters of Figure 2.1

H_p	Wave height primary wave [m]	T_{Hp}	Primary wave period [s]
H_s	Wave height secondary waves [m]	T_{SU}	Time from bow wave to drawdown [s]
z	Drawdown [m]	T_{ST}	Time from drawdown to stern wave [s]
s_B	Bow wave height [m]	T_{Hs}	Secondary wave period [s]

2.1.2. Primary wave concepts

The primary wave system consists of a bow wave, a stern wave and the drawdown along the length of the ship's hull. These elements have been calculated for many years and depend on a large number of variables, resulting in large analytical equations. Therefore, this section presents two ways of describing the primary wave systems, both of which rely on some important assumptions and simplifications to achieve a smaller analytical equation.

Method of Schijf (1949)

The primary wave of a ship in a relatively narrow and shallow channel is directly dependent on the ship's speed and its wet cross-sectional area. In such cases, the flow around a ship can be approximated by the Bernoulli equation (Schijf, 1949), also known as the 1-dimensional approach. Schijf made the following assumptions. A ship travelling in the centre of the channel has a prismatic hull cross-section. It is positioned horizontally. The channel cross-section is prismatic and the backflow including drawdown is constant.

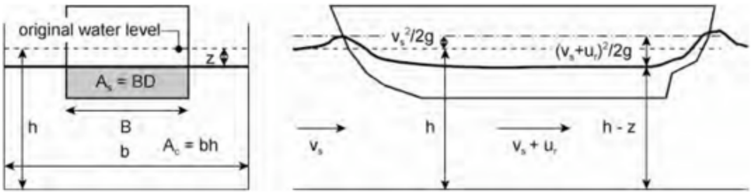

Figure 2.2: Definitions of Schijfs method to determine flow around a ship's hull (Schiereck & Verhagen, 2012)

Figure 2.2 depicts all parameters of the primary wave systems based on the method of Schijf. By substituting these parameters in the Bernoulli and continuity equations, and taking into account Schijf's assumptions, the following equations are resulted:

$$h + \frac{v_s^2}{2g} = h - z + \frac{(v_s + u_r)^2}{2g} \tag{2.1}$$

$$bhv_s = (bh - BD - bz)(v_s + u_r)) = Q \tag{2.2}$$

With:

h = water depth [m]
b = channel width [m]
B = ship width [m]
D = ship draught [m]
z = drawdown [m]
v_s = flow velocity [m/s]
u_r = backflow velocity [m/s]
Q = discharge of return flow [m^3/s]

The maximum vessel velocity V_l is reached when the backflow becomes critical or when the derivative of the backflow with respect to the drawdown is zero. This can be combined with the Bernoulli's equation 2.1 which gives the equation that can be used to determine the maximum flow and vessel velocity. Furthermore, Schijf derived the drawdown (z) by combining Equations 2.1 and 2.4 and wrote it in the dimensionless form.

$$\frac{A_c}{A_s} + \frac{V_l^2}{2gh} - \frac{3V_l^{\frac{3}{2}}}{2(gh)^{1/3}} = 1 \tag{2.3}$$

$$\frac{v_s^2}{gh} = \frac{2z/h}{(1 - A_s/A_c - z/h)^{-2} - 1} \tag{2.4}$$

Field experiments were performed to evaluate the previous equations. Van der Wal (1990) found a standard deviation of the drawdown which is defined by the following equation:

$$\sigma(z) = 0.01 * \frac{v_s}{V_l}\frac{A_c}{b} \tag{2.5}$$

If the dimensions of the vessel and the fairway are known, the drawdown derived by Schijf depends only on the velocity of the vessel. Usually, the authorities set a limit on the ship's speed on waterways, which can be used to determine the actual maximum drawdown of the ship. However, the set of equations by Schijf are derived for idealised conditions greatly simplifies the flow conditions. He assumed that the water level during the drawdown was uniform and that the backflow was depth-averaged. However, the drawdown is in practice non-uniform and the backflow varies with depth.

Method of Lap (1956)
To compensate for the non-uniformity, a more fundamental equation is made by Lap (1956). He used a correction factor α_u, introduced by Jansen and Schijf (1953), which compensates for the non-uniformity of the velocities and is empirically derived as:

$$\alpha_u = 1.4 - 0.4 * \frac{V_s}{gh^{0.5}} \tag{2.6}$$

Next, the geometries of the channel and ships can be made dimensionless in order to determine a more fundamental equation for ships travelling in shallow confined waterways. Factor K represents the dimensionless blockage and the factor β is the dimensionless width of the free surface.

$$K = A_s/A_c \tag{2.7}$$

$$\beta = B_{f,s}/B \tag{2.8}$$

Lap (1954) combined the Bernoulli and continuity equations 2.1 & 2.2 with the dimensional factors (Equations 2.7 & 2.8) into a single fundamental equation of ship travelling through a river or channel, presented in Equation 2.9. Using this equation, the return current U_r can be derived given a certain water depth h, ship velocity V_s and the dimensions of the vessel and waterway. The corresponding drawdown z can be determined by implementing the determined backflow velocity U_r, water depth h, and ship velocity V_s using the momentum balance, as shown in Equation 2.10.

$$\frac{V_s}{gh^{0.5}} = \frac{V_s + U_r}{gh^{0.5}} * \left\{1 - K - \frac{\alpha_u \beta}{2}(\frac{V_s + U_r}{gh^{0.5}})^2 - (\frac{V_s}{gh^{0.5}})^2\right\} \tag{2.9}$$

$$\frac{1}{2}\rho V_s^2 + \rho g h = \frac{1}{2}\rho \alpha_u (V_s + U_r)^2 + \rho g (h - z) \tag{2.10}$$

Approximation of stern wave height
The methods of Lap (1954) and Schijf (1949) describe an equation that can be used to determine the drawdown of a passing ship based on simplifications. If the ship is not at the centre of the canal or river, the drawdown can be corrected as shown in Equation 2.11. Here, y is the distance between the centre axis and the vessel's position. The height of the stern wave is determined by the following approximation:

$$z_{ecc} = (1 + \frac{2y}{B}) * z \tag{2.11}$$

$$H_p = 1.5 z_{ecc} \tag{2.12}$$

2.2. Overflowing flow velocities

The long-period primary ship-induced waves overflow the groynes in the Lower Elbe estuary. As stated in Section 1.2 Research objectives, one of the objectives of this research is to determine a flow velocity equation on the lee side of the groyne structure. Therefore, a literature review will be carried out to find equations that can describe this overflowing flow velocity.

2.2.1. General concepts of overflowing structures

A groyne structure can be described as a rubble mound or rock structure, as the structure can be constructed almost entirely from loose rock. As stated in Section 1.4 Research scope, this research focuses on the armour layer and the first filter layer of the groyne structure. The core will be impermeable and therefore the overflow will be outside the structure. Furthermore, the overflow will be investigated at the trunk of the groyne. For these reasons, the flow over the structure will behave like the flow over a weir-type structure.

Flow theory

Water flows when there is a difference in piezometric head between two points. The velocity of the flow depends on the difference in piezometric head and the resistance of the water path, which is influenced by friction or objects. Flow over objects and structures can be described by a form of the Bernoulli equation. This equation describes the relationship between pressure, velocity and head of a fluid in a system. It is based on the principle of energy conservation, which states that the total energy of a system remains constant over time. For an open and incompressible flow, the Bernoulli equation can be described as follows:

$$z_1 + h_1 + \frac{\overline{u_1}^2}{2g} = z_2 + h_2 + \frac{\overline{u_2}^2}{2g} + h_L \tag{2.13}$$

With:
z_1 = water elevation at location 1 [m]
z_2 = water elevation at location 2 [m]
h_1 = water depth at location 1 [m]
h_2 = water depth head at location 2 [m]
h_L = head loses [m]
$\overline{u_1}$ = averaged flow velocity at location 1 [m/s]
$\overline{u_2}$ = averaged flow velocity at location 2 [m/s]

The state of the flow between two points in a free surface system can be described by the Froude number, given by Equation 2.14. This number expresses the inertial force of the flow relative to the gravitational force and describes the flow velocity of the water relative to the wave celerity. A free surface system can have three types of flow conditions, namely supercritical (Fr > 1), critical (Fr = 1)and subcritical (Fr < 1). In supercritical conditions, waves only travel downstream and downstream actions don't influence upstream flow. During subcritical conditions, a wave can move downstream and upstream, resulting in upstream changes if there are downstream changes.

$$Fr = \frac{u}{\sqrt{gh}} \tag{2.14}$$

Overflow weir types
Flow over structures can be described as flow over weir structures. These are generally divided into two groups: sharp-crested weirs and weirs of finite crest length, as shown in Figure 2.3. This second group can be subdivided into three groups; broad-crested, long-crested and narrow-crested weirs, depending on the h/L ratio (Azimi et al., 2013). Where h is the water depth measured from the crest at a distance in front of the structure and L is the length of the crest. The range for long weirs is about 0-0.1, for broad-crested weirs 0.1-0.4 and for narrow-crested 0.4-2.0. Ratios greater than 2.0 result in flow characteristics similar to those of a sharp-crested weir.

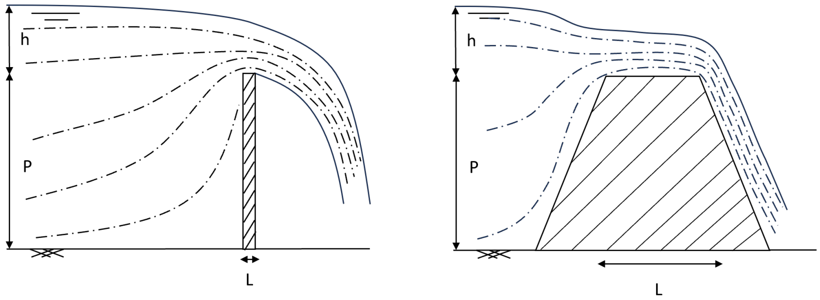

Figure 2.3: Overflow over weir structures with corresponding streamlines. Left: Example of a sharp-crested weir where h/L > 2.0. Right: example of a finite crested weir where h/L < 2.0

Normally a weir is constructed to control upstream water levels by changing the flow in the waterways. For finite crested weirs, this discharge depends mainly on the upstream and downstream water levels. As the water approaches the weir, shown right in Figure 2.3, the flow starts to accelerate from the start of the structure and the streamlines contract until it reaches the crest. Here, the flow has increased in velocity and approaches critical flow conditions. The streamlines become parallel. This results in a decrease in water level at the top of the crest. Depending on the water levels behind the structure, the critical conditions are met at the crest. Suppose the water levels behind the structure are significantly lower than the crest of the weir. In that case, the flow at the crest becomes critical and even supercritical until it interacts with the downstream water levels. This condition is also known as the free flow condition. On the other hand, if the water levels behind the structure are close to, equal to or greater than the crest level, subcritical conditions will result.

The approach of the flow to the crest of a sharp-crested weir is almost the same as for a finite crested weir. The main difference is that at the crest of the sharp-crested weir, the flow is unattached from the structure. There is a critical flow condition as long as the downstream water level is lower than the crest level. The streamlines above the crest are curved which results in most cases in a larger discharge and velocity compared to a finite crested weir.

As long as there are free-flow conditions (critical flow conditions at the crest), the weir discharge relation can be used for both types of weirs (Poleni, 1717):

$$Q = C_d B \sqrt{\frac{8}{27}} \sqrt{g} h^{\frac{3}{2}} \tag{2.15}$$

Where:
Q = discharge [m^3/s]
C_d = discharge coefficient [-]; finite crested weir C_d < 1.0 and sharp-crested weir C_d > 1.0
B = width of weir [m]

2.2.2. Overflowing over other structures: velocity equations

As shown in the previous section, the discharge over a weir-type structure can be described by Equation 2.14, which depends on the geometry of the structure and the hydraulic conditions. The flow on the downward slope is described by the Froude number, where subcritical, critical and supercritical flow conditions can be defined. Although this gives a first insight into the flow conditions at the slope, it remains unclear what flow velocities occur. Therefore, a review was conducted to find an analytical velocity equation at the downward slope of rock structures.

In the course of this study, it became evident that there is still a need for further research, as there are only a few sources that provide a flow velocity equation for downslope structures. In particular, rock structures are not yet included in the downward flow velocities. Biabani et al. (2021) performed an experimental study in which velocity measurements were done at the crest and bottom of several configurations of a gabion weir. However, no velocity equation was presented. Accordingly, other types of structures were evaluated; embankment weirs, trapezoidal weirs and spillways. Kindsvater (1964) and Fritz & Hager (1998) carried out physical modelling experiments for embankment and trapezoidal weir and measured flow velocities. Velocity equations were determined at the crest and behind the structure, but not at the downward slope. Other studies of weirs have all focused on determining the discharge coefficient. The last structure examined is a spillway structure since its function is to discharge water down a slope. However, the same observation was made for this structure as for the rock structures and weirs: Very few studies have been carried out to describe the velocity equation on a sloping structure. Most researchers presented a numerical model to describe the overflow. Cheng and Gulliver (2011) presented a study in which a model was developed to determine the flow velocities along the slope of a stepped spillway. The model is based on the log-wake law and reads:

$$\frac{u}{u_*} = \left(\frac{1}{\kappa} ln \frac{yu_*}{\upsilon} + B\right) + \frac{2\prod}{\kappa} sin^2 \frac{\pi\xi}{2} - \frac{\xi^3}{3\kappa} \tag{2.16}$$

Where u = time-averaged velocity, u_* = shear velocity, κ = von Karman constant, y = distance to the structure, υ = kinematic viscosity of the fluid, B = wall roughness constant, $\prod$ = Coles wake strength and ξ = normalized distance relative to the dip. This equation describes a turbulent flow along a downward slope but depends on many assumptions and structure-dependent constants, therefore Cheng and Gulliver (2011) used this equation in a numerical way.

Due to the lack of research in flow velocity equations along a downward rock slope, the theoretical maximum mean flow velocity is determined by assuming developed flow conditions for slopes with a large length. The Manning formula with the Strickler coefficient for the riprap is used to determine the theoretical maximum velocity.

$$u_d = k_s * R_h^{\frac{2}{3}} * \theta^{1/2} \tag{2.17}$$

$$k_s = \frac{b_1}{k^{b_2}} \tag{2.18}$$

Here, u_d is the mean developed flow velocity along a slope. R_h is the hydraulic radius and θ is the slope. k_s is the Strickler coefficient with $k = \theta * d_{50}$, b_1 = 12.21 and b_2 = 0.159 for crushed dumped rocks after Abt et al. (1987).

Seemann and Melling (2021) assumed that the developed flow at the lee side slope is reached when the slope length (L_s) between the crest and lee side water level is larger than the theoretical developing length (L_d). Velocities for smaller slope lengths than the developing length are based on linear interpolation for ratio L_s and L_d, presented by Equation 2.19.

$$u = u_{crest} + \frac{L_s}{L_d}(u_{crest} - u_d) \tag{2.19}$$

$$L_d = \frac{1}{8} * cot(\alpha)(20h_d - 33k) \tag{2.20}$$

2.3. Damages assessments on rubble mound structures

The overflowing of groynes caused by primary ship-induced waves results in damage and deformation to the crest and lee side of the structure. This section discusses the general concepts of damage to rock structures and reviews the known literature on damage due to overflowing.

2.3.1. General concepts stability and damage on rock structures

Slope stability wave facing side

A structure must remain stable in order to perform its function. For wave-loaded rock structures, this stability can be expressed in terms of the stability number N_s and has been defined by the CIRIA et al. (2007).

$$N_s = \frac{H}{\Delta D} \tag{2.21}$$

With:
H = Wave height [m]
Δ = Relative density (see Equation 2.22) [-]
D = Diameter of rock [m]

$$\Delta = \frac{\rho_s - \rho_w}{\rho_w} \tag{2.22}$$

Where ρ_s is the density of the rock [kg/m^3] and ρ_w is the density of the water [kg/m^3].

The rock's diameter can be expressed in d_{50} or d_{n50}. The first parameter represents the median grain size for a normal grain size distribution, where 50 % of the rocks are larger than the d_{50} value. For larger rocks this is more difficult to measure, so the d_{n50} is used. Instead of measuring the diameters, the weight of the stones is determined. The parameter is called the nominal diameter and is defined as follows :

$$d_{n50} = \sqrt[3]{\frac{W_{50}}{\rho_s}} \tag{2.23}$$

As rocks have approximately the same shape, a relation between d_{50} and d_{n50} exists:

$$d_{n50} = 0.84 d_{50} \tag{2.24}$$

One of the first design formulae for wave-attacked rock structures was developed by Irribaren (1938) and focuses on the impact of waves on the wave-facing side. The formula uses the equilibrium of forces combined with a correction coefficient determined by a physical model test with regular waves. Hudson (1953) carried out further tests on the Irribarren equation and proposed a different formula:

$$N_s = \sqrt[3]{K_D cot(\alpha)} \tag{2.25}$$

The Hudson formula is a simple and effective way of determining stability. However, due to its simplicity, it has limitations as important wave and structure parameters are missing: Wave period, permeability of structure (P), number of waves (N) and the damage parameter (S).

Therefore, new research has been carried out to overcome these limitations. Van der Meer (1988) presented the following stability equation for plunging breakers and surging breakers respectively:

$$N_s = 6.2 P^{0.18} (\frac{S}{\sqrt{N}})^{0.2} \xi^{-0.5} \tag{2.26}$$

$$N_s = 1.0 P^{-0.13} (\frac{S}{\sqrt{N}})^{0.2} \xi^{P} \sqrt{cot\alpha} \tag{2.27}$$

Slope stability due to overflowing

The Hudson and Van der Meer equations are used to determine the stability of rubble mound structures subjected to wave loading on the wave-facing side. The groyne investigated in this study is overflown by the primary ship waves causing damage to the lee side of the structure. Therefore the Hudson and Van der Meer equation is not applicable. The damage caused by the overflowing waves occurs due to high flow velocities. The first research into the stability of rockfill structures due to overflow was carried out by Izbash (1935). Rockfill dams were tested in shallow water under steady-state overflowing conditions and the following stability relationship was obtained:

$$\frac{u_c}{\sqrt{\Delta g d}} = K \tag{2.28}$$

Where:
u_c = Critical flow velocity of the rock [m/s]
Δ = Relative density [-]
g = Gravitational constant $[m/s^2]$
d = Diameter of the rock [m]
K = Izbash constant (a first approximation is 1.7 [-])

The Izbash equation doesn't include the slope of a structure. However, it can be expected that a steep slope can influence the stability significantly compared to a mild slope. To compensate for this effect the slope factor K_s can be applied. It expresses the influence of the slope in degrees (α [deg]) and the angle of repose of the material (ϕ [deg]) for flow going down the slope.

$$K_s(\alpha) = \frac{sin(\phi - \alpha)}{sin(\phi)} \tag{2.29}$$

More research on overflowing and corresponding stability was performed. Abt et al. (2013) collected 21 stability equations for riprap subjected to continuous overflow. Three of these are highlighted. Abt and Johnson (1991) derived a regression-based stability expression which uses the slope θ and q_{design} = 1.35 * $q_{failure}$ [ft^2/s].

$$D_{50} = 5.23\theta^{0.43} q_{design}^{0.56} \tag{2.30}$$

The best overall performing stability equation for rubble mound structures given by Abt et al. (2013), was derived by Khan (2011) using a full empirical regression approach. Their equation uses the number of layers in the armour layers (n), slope θ, C_u as the coefficient of uniformity and q_f as the failure unit discharge.

$$D_{50} = 0.66(n * d_{50})^{0.58} \theta^{0.22} C_u^{-0.45} q_f^{0.21} \tag{2.31}$$

Thornton et al. (2014) used the equation of Khan (2011) and introduced the specific stone gravity (SG) to influence the diameter of the rocks:

$$D_{50} = 0.57\theta^{0.20} C_u^{-0.28} q_f^{0.21} t^{0.62} \frac{1.16}{(SG - 1)^{0.30}} \tag{2.32}$$

All these equations are based on continuous overflow. No stability equation was found in the literature that expresses the stability due to overflowing long-period waves. This indicates the need for research on this topic.

2.3.2. Damage parameters and limits

As one of the objectives of this research is to determine the damage, it is important to explain the methods used to quantify damage. In the Van der Meer equation (2.26 & 2.27) one damage parameter, namely the S-parameter, is already briefly mentioned. This is an internationally recognised damage parameter and is used in many applications to determine damage to erodible structures. To determine when damage has occurred, the damage limits of a structure must be defined. These are the limits of certain damage phases: damage initiation, intermediate damage and failure.

Past research first focused on damage parameters. Before the S-parameters, several other damage parameters were introduced. One of the first damage parameters was introduced by Hudson (1953) when he needed to calibrate his stability equation (Equation 2.25) for wind waves. Hudson defined the damage characteristic as 'damage initiation' when 1 % of the armour units have been moved due to wave loads. Therefore, he introduced damage parameter D.

$$D(\%) = \frac{Number\ moved\ armour\ units}{Total\ number\ armour\ units} \tag{2.33}$$

The next iteration into a new damage parameter was presented by Thompson and Shuttler (1975). They studied the stability of rip-rap structures and found that damage was caused by a statistically random attack by wind waves. As a result, a new damage parameter was presented which defined: 'number of d_{50} sized spherical stones eroded from a width of 9 d_{50}'. Next, the corresponding damage limits were given, with 'damage initiation' defined as the point at which the damage increases significantly with increasing wave height. The 'failure' limit was defined as when the filter layer was exposed through a hole with a diameter of d_{50}/2.

$$N_\Delta = \frac{V_e \rho_B}{\rho_s (\frac{1}{6} \pi d_{50}^3)} \tag{2.34}$$

In which:
V_e = Eroded Volume $[m^3]$
ρ_B = bulk density of eroded volume $[kg/m^3]$
ρ_s = mass density of rock $[kg/m^3]$

The damage parameter S was introduced by Broderick and Ahrens (1982), and van der Meer (1988) applied the parameter. The damage parameter S was defined as 'eroded volume made dimensionless by the nominal mean diameter'. The damage initiation limit was used to describe the onset of damage and was applicable to values of S = 1 - 3, based on the Hudson damage limits for wind waves. The failure limit is defined as the value of S at which the filter layer is exposed, giving S = 8 - 17.

$$S = \frac{A_e}{d_{n50}^2} \tag{2.35}$$

In which:
A_e = Eroded area $[m^2]$

Although the S-parameter is still used today, new damage parameters have been introduced. Melby and Kobayashi (1998) showed three dimensionless damage parameters: Erosion Depth E, Erosion Length L and Cover Depth C. They further stated that the failure damage limit occurs when a hole of diameter d_{n50} is observed from the armour layer to the filter layer.

$$E = \frac{d_e}{d_{n50}},\ L = \frac{l_e}{d_{n50}},\ C = \frac{d_c}{d_{n50}} \tag{2.36}$$

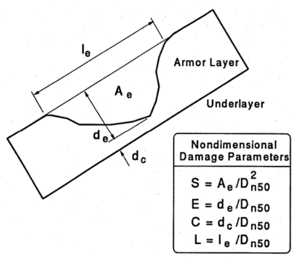

Figure 2.4: Dimensionless damage parameters defined by Melby and Kobayashi (1998)

Following the non-dimensional damage parameters of Melby & Kobayashi, Hofland et al. (2011) developed an additional concept of the dimensionless erosion depth parameter (E) by measuring it in 2D or 3D. This resulted in E_{2D}, which can be obtained by measuring the initial and the final alignment of a straight element of a structure. E_{3D} is used for non-straight structures, such as the head of a groyne. It can be measured by a three-dimensional survey which is averaged with a circular moving area width m times d_{n50} in diameter. The corresponding damage limits have been defined as follows: The 'damage initiation' limit occurs when one armour unit is moved in a strip of 1 d_{n50} wide. Failure occurs when a local armour thickness of 0 is measured.

$$E_{2D} = \frac{\max \langle e \rangle_w}{d_{n50}} \tag{2.37}$$

$$E_{3D,m} = \frac{\max \langle e \rangle_{md_{n50}}}{d_{n50}} \tag{2.38}$$

In which:
$\langle e \rangle_w$ = erosion depth-averaged over width [m].
$\langle e \rangle_{md_{n50}}$ = erosion depth-averaged over a circular area with diameter m times d_{n50} [m].

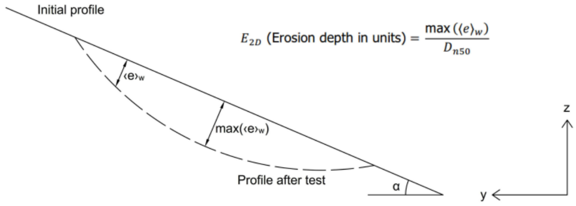

Figure 2.5: Schematic view of the damage parameter E_{2D} from de Almeida et al. (2019)

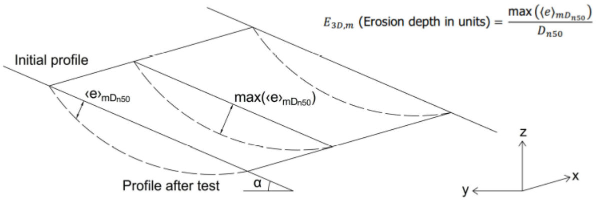

Figure 2.6: Schematic view of the damage parameter $E_{3D,m}$ from de Almeida et al. (2019)

2.3.3. Damage measurements in past researches

This section examines damage limits and parameters that were applied in past research involving damage assessments on rock structures subjected to wave loads. Since this research focuses on groyne structures, the aim is to find past research that also focuses on groynes.

N. Allsop and Jones (1994) & (1995) published two papers on damage assessment of groyne structures. In both papers, physical models of roundhead, L-shaped and inclined groyne structures were used to determine the S-parameter as defined by Van der Meer (1988). The structures were subjected to 1000 to 3000 wind waves and after each test, the structures were photographed. The tests were stopped when the structures had to be rebuilt. These two studies focused only on the damage parameter and did not define additional damage limits. It is therefore assumed that the damage limits defined by Van der Meer were used in these studies.

Other groyne-like rock structures are also considered. Vidal (1995) was among the first to use the S-parameter to measure the stem damage of a detached rubble mound breakwater. In the same year, Franco and Tomsicchio (1992) determined the same damage parameter for historic and modern seawalls. In a follow-up study on breakwaters, Vidal et al. (1995) carried out the same measurements to determine the S-parameter using an electromechanical profiler. In the following years, the damage parameter S was increasingly used by many researchers for rubble mound breakwaters. The main difference between all these studies was the profiling technique used. Kramer and Burcharth (2004) and Burcharth (2006) started to use digital photographs to investigate the stability of low-crested rubble mound breakwaters. This led to more reliable results as there was no physical interaction with the damaged structures during the determination of displacements.

One of the more recent studies on the damage characterisation limits of rubble mound structures for the damage parameters S, E_{2D} and $E_{3D,m}$ was carried out by de Almeida et al. (2019). He used the two new damage parameters, introduced by Hofland et al. (2014) to measure the damage on detached breakwaters attacked by irregular waves. The characterisation limits damage initiation, intermediate damage and failure expressed in S, E_{2D} and $E_{3D,5}$ where calibrated by using $E_{3D,1}$ values. The failure limit was defined as the point at which the filter layer was exposed. For a 2 d_{n50} thick armour layer the $E_{3D,1}$ characterisation limits were 1.0, 1.5 and 2.0 for damage initiation, intermediate damage and failure, respectively. This resulted in the following characterisation limits for damage parameters S, E_{2D} and $E_{3D,5}$:

- Damage initiation: defined as the condition where a circular hole of $1d_{n50}$ in diameter and a depth of $1d_{n50}$ is observed in the armour layer: $E_{3D,1}$ = 1, $E_{3D,5}$ = 0.3, E_{2D} = 0.2, S = 1.
- Intermediate damage: defined as the condition where a circular hole of $1d_{n50}$ in diameter and a depth of $1.5d_{n50}$ is observed in the armour layer: $E_{3D,1}$ = 1.5, $E_{3D,5}$ = 0.7, E_{2D} = 0.5, S = 4.
- Failure limit: defined as the condition where a circular hole of $1d_{n50}$ in diameter and a depth of nd_{n50} is observed in the armour layer, with n equal the number of rock layers in the armour layer: $E_{3D,1}$ = 2.0, $E_{3D,5}$ = 1.1, E_{2D} = 0.9, S = 11.

All of the mentioned studies in Section 2.3 determine damage limits and parameters for structures subjected to wave action on the wave-facing side. No studies were found that describe the damage at the lee side of the structure for overflowing waves for rubble mound structures. Therefore, additional damage measurements and damage limits need to be determined for structures subjected to lee side damage from overflowing waves.

2.4. Physical modelling guidelines

As described in Chapter 1, physical modelling experiments are performed to measure overflowing flow velocities and to assess the corresponding damage. Physical models are used to test the response of the structure under controlled conditions, providing insight into unexplained phenomena and avoiding simplifying assumptions present in analytical or numerical models (W. Allsop et al., 2007).

'A physical model is a reproduced physical system (usually at a reduced size) so that the major dominant forces acting on the system are represented in the model in correct proportion to the actual physical system' (Hughes, 1993).

Chanson (2004) stated that in a physical model the flow conditions are considered to be similar to those in the prototype if the model has geometric similarity (form), kinematic similarity (motion) and dynamic similarity (forces). Hughes (1993) presented 5 scaling requirements that consider these three types of similarities for the design of a physical model that consists of loose rocks.

Requirement 1
The geometric properties of the physical model must be undistorted. This implies that the ratios of the prototype characteristics' length to the model lengths are equal:

$$L_r = \frac{l_p}{l_m} = \frac{d_p}{d_m} = \frac{H_p}{H_m} \tag{2.39}$$

Requirement 2
Kinematic properties must be modelled using the Froude similarity.

$$Fr_p = Fr_m : \left(\frac{U_w}{\sqrt{g l_a}}\right)_p = \left(\frac{U_w}{\sqrt{g l_a}}\right)_m \tag{2.40}$$

Requirement 3
The turbulent flow conditions at the prototype must be the same as the model throughout the primary armour.

$$Re_p = Re_m : \left(\frac{U_w l_a}{\mu \rho_w}\right)_p = \left(\frac{U_w l_a}{\mu \rho_w}\right)_m \tag{2.41}$$

Requirement 4
The relative mass density of the material used in the prototype must be equal to the relative mass density of the model.

$$\Delta_p = \Delta_m : \left(\frac{\rho_w}{\rho_s - \rho_w}\right)_p = \left(\frac{\rho_w}{\rho_s - \rho_w}\right)_m \tag{2.42}$$

Requirement 5
The surface roughness of the armour in the prototype must be the same as in the model.

$$\left(\frac{\epsilon_a}{l_a}\right)_p = \left(\frac{\epsilon_a}{l_a}\right)_m \tag{2.43}$$

Table 2.2: Parameters for physical modelling requirements

L_r	scaling ratio [-]	H	wave height at the structure [m]
l_a	a linear dimension of an armour unit [m]	U_w	flow velocity of water [m/s]
l_p	a linear dimension of the prototype characteristic [m]	g	gravitational constant [m/s^2]
l_m	a linear dimension of the model characteristic [m]	μ	dynamic viscosity [kg/m/s]
d	water depth at the structure [m]	ϵ_a	surface roughness [m]

3

Physical modelling: Theory

This chapter presents the elements that need to be understood before designing the experimental setups. Section 3.1 presents the dimensions and hydraulic conditions of the prototype. Section 3.2 introduces two new flow equations. Section 3.3 explains the measurement methods to be used during the experiments.

3.1. Deriving relevant parameters

3.1.1. Prototype dimensions

The prototype groyne structure in the Lower Elbe estuary has been renovated and renewed several times during its lifetime (Melling et al., 2020). The core material therefore consists of remnants of historic groyne structures. The most recent improvements are a new armour layer of LM$_{b5/50}$ high-density iron silicate rock. The slope has also been changed from 1:3 to 1:4. The nominal rock diameter d$_{50}$ of the LM$_{b5/40}$ rocks is about 0.20 metres with a corresponding rock density ρ_s of 3.7 - 3.9 ton/m^3.

The BAW has provided a cross-section of the prototype groyne, which is used to determine its dimensions. The cross-section, shown in Appendix B, shows the profile of 32 measurements taken approximately every 13 days from 22 December 2017 to 31 January 2019. To extract the dimensions, an approximation was made by assuming a constant profile. The width (W) of the groyne was set at 19 metres. The length of the slope (W$_s$) and the width of the crest (W$_c$) were 8.5 and 2.0 metres respectively. The total height of the groyne (P) is set to 2.33 metres. The corresponding radius R is 3.91 metres and the slope θ is 1:4 (α = 14°) and angle of repose (ϕ = 40 °).

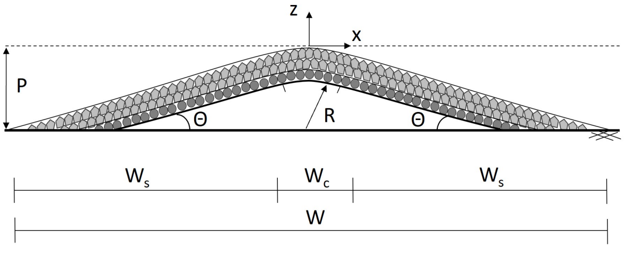

Figure 3.1: Cross-section of prototype groyne

Prototype dimensions		
P	Crest height	2.33m
W_c	Crest width	2.0m
W_s	Length of slope	8.5m
W	Total width	19m
θ	Slope	1:4
R	Radius top	3.9m
ϕ	Angle of repose	40°

3.1.2. Hydraulic conditions prototype

Hydraulic conditions were determined during a field study on both concept groynes, carried out by the BAW. Wave data measured on the crest of the structure was used to determine the hydraulic conditions. Melling et al. (2020) stated that over 90 % of the primary waves were smaller than 0.5 metres. Primary waves greater than 1.0 metres were defined as ‘large waves’ and occur only at 1% of the waves. The maximum primary wave height recorded at the crest is 1.40 meters. To summarise the data, a dimensionless range of hydraulic head (h) to groyne height (P) at the top of the groyne is given by:

$$0 < \frac{h}{P} < 0.6 \tag{3.1}$$

The change in water level due to the drawdown of the passing ship was only measured on the wave-facing side. Although these measurements were conducted on the opposite side of the structure compared to the location of the damage, it is assumed that the difference in drawdown is small. Therefore the drawdown measured at the wave facing side is used. The range of maximum freeboard (R_c) caused by the drawdown compared to the groyne height (P) is as follows:

$$0 < \frac{R_c}{P} < 0.46 \tag{3.2}$$

During the same field study, the flow velocities on the crest were recorded. In total 1850 primary wave events were measured. The flow velocities at the crest were usually less than 0.5 m/s. About 27% of the flow velocities were greater than 1.0 m/s, often reaching 2.0 m/s. Only in rare cases were overflow velocities recorded at the crest exceeding 3.0 m/s.

3.2. Additional overflow velocity equations

As presented in the literature review in Chapter 2, the flow velocity on the lee side of the groyne was only analytically described by the theoretical maximum developed flow velocities based on the Manning equation (Equation 2.17). This equation can be used for slopes of great lengths. However, it is unexpected that the flow over the groynes reaches the fully developed state. Consequently, two additional equations are formulated. First, an equation based on the Bernoulli equation was developed. Second, a dimensional analysis was performed to obtain a dimensionless flow equation on the lee side of the groyne. Both equations are based on the parameters shown in Figure 3.2.

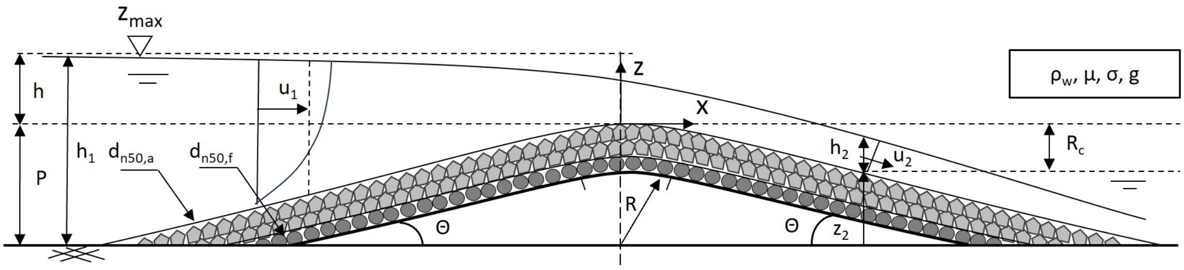

Figure 3.2: Side view groyne during continuous overflow. u_2 is determined at the position where the theoretical lee side freeboard (R_c) interacts with the armour layer.

3.2.1. Dimensional flow equation

The first additional flow equation is based on the Bernoulli equation. The system where the energy is assumed to be equal is set from the toe at the wave-facing side to toe at the lee side and results in the following adjusted Bernoulli equation:

$$P + h + \frac{u_1^2}{2g} = z_2 + h_2 + \frac{u_2^2}{2g} + h_L \tag{3.3}$$

With:
P = groyne height [m]
h = water depth above the crest height [m]
h_2 = water depth lee side [m]
z_2 = structures height along the lee side slope [m]
h_L = head loses [m]
u_1 = initial flow velocity [m/s]
u_2 = flow velocity at lee side [m/s]

This equation is rewritten in a corrected equation assuming the initial flow velocity (u_1) and head losses (h_L) to be expressed by a correction factor α.

$$u_2 = \alpha\sqrt{2g((h_1 - (h_2 + z_2))} \tag{3.4}$$

The equation is simplified by expressing the overflow velocity entirely in terms of the lee bed level (z_2), i.e. no overflow depth h_2 is taken into account. This results in the overflow velocity being expressed as the difference between the wave-facing water level (h_1) and the lee side bed level (z_2). The same difference can also be expressed as the difference between the wave-side water level and the lee side bed level, measured from the top of the groyne, resulting in an equation that is independent of the groyne height P.

The overflow will accelerate along the slope until it reaches the lee side water level. As there is no initial lee side water level during the flow experiment, a notional lee side water level is positioned to extract the flow velocities. This corresponds to the position at which the water level would have been at the bed level. The lee side water level measured from the crest is expressed as the theoretical free board (R_c) resulting from the subsidence of the primary ship wave. Taking these steps into account, the following equation is going to be used to express the overflowing flow velocities for a water depth above crest level (h) and fictional freeboard level (R_c).

$$u(h, R_c) = \alpha\sqrt{2g(h + R_c)} \tag{3.5}$$

3.2.2. Dimensionless flow equation

A dimensional analysis is performed to express the flow velocity on the lee side of the groyne structure in a dimensionless form, based on the Buckingham-Pi theorem. This mathematical theorem relates the dimensionality of a physical system to the number of dimensionless groups that can be formed from different independent variables. The theorem states that for a physical system with n variables, n - k dimensionless groups can be formed. Where k is the number of dimensions that are independent. In this case, a function (f) based on a continuous flow over groynes is determined by the following variables:

$$f(u, h, R_c, g, \mu, \rho_w, \sigma, d_{n50,a}, \theta) \tag{3.6}$$

Where u = flow velocity along lee side [m/s], h = water depth at wave facing side above crest level [m], R_c = freeboard due drawdown [m], μ = dynamic viscosity of water [kg/m^2/s], ρ_w = water density [kg/m^3], σ = surface tension [N/m^2], $d_{n50,a}$ = nominal stone diameter armour layer [m], θ = slope of structure [-].

The parameters h, ρ_w and g are used as dimensional independent variables in the Buckingham-Pi analysis, as these parameters describe the length, fluid and flow characteristics. This resulted in 6 dimensionless groups, all of which are presented in Appendix A, including the determination. These groups can be reduced to just 2 independent dimensionless groups which form the second additional flow velocity equation.

$$\frac{u}{\sqrt{gh}} = f(\frac{R_c}{d_{n50,a}}, \theta) \tag{3.7}$$

3.3. Measurement techniques during experiments

3.3.1. Flow experiment: Particle image velocimetry

The first experiment is conducted to measure the overflow velocities at the lee side by means of a constant overflow. The measurement technique used is Particle Image Velocimetry (PIV). This method is an optical measurement technique in which the velocity field of an entire region within the flow is measured simultaneously by measuring the displacement of particles that are assumed to follow the flow (M.D. Atkins, 2016).

The main advantage of PIV measurements over traditional point measurement devices is that PIV is a quantitative flow field mapping technique that can provide insight into the flow behaviour of an entire region. Whereas the flow measured by point measurement devices must be approximated between two measurement locations. In addition, PIV can facilitate both the extraction of measurement data and the visualisation of flow by illuminating flow particles in the fluid. This optical measurement device avoids the physical interaction between the fluid and a physical measurement device (such as pitot tubes, micro-propellers or anemometers), which eliminates corresponding distortions in the flow. For this reason, a PIV measurement gives a more realistic result compared to a point measurement device and is used during the flow experiments.

The PIV setup Planar-PIV is used to measure a two-dimensional velocity field. A typical PIV setup includes a high speed camera, a high power light source, tracer particles and an optical arrangement to convert the light output into a light sheet. This light sheet is pointed to the region of interest. The light source is reflected by the tracer particle with diameter d_τ and is captured by the camera. A corresponding location can be assigned to the particles per frame. By taking two consecutive frames, recorded at t_0 and $t_0 + \Delta t$, the displacement and velocity are obtained. These two frames are called a frame pair. Each of the frames is completely divided into smaller sections, called interrogation windows with squared dimensions D_I. Each of these windows is compared to the other frame within a frame pair. In each interrogation window within a frame pair, a displacement and velocity vector are assigned based on cross-correlation. This results in an overall two-dimensional velocity field for each frame pair. Figure 3.3 gives an impression of the PIV setup and analysis.

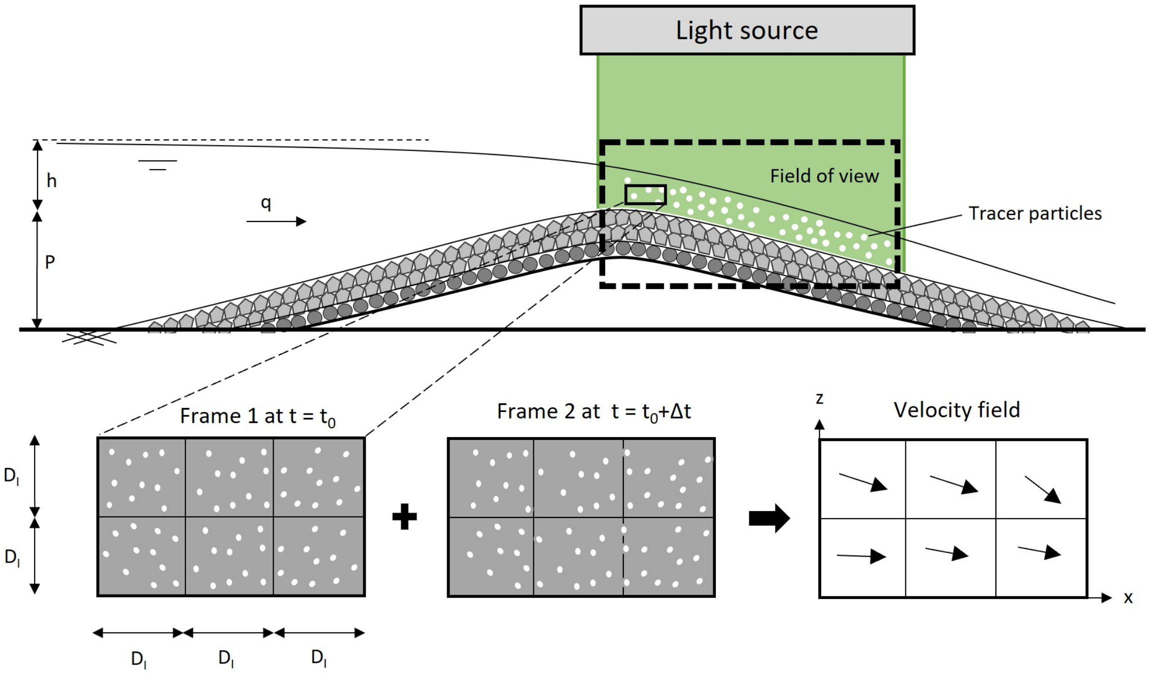

Figure 3.3: Impression of PIV setup with a corresponding field of view of the camera and close-up view of two frames within a frame pair leading to the velocity field.

To perform the PIV measurement, the following four design rules have to be considered. These four rules are introduced by Adrian and Westerweel (2011) and are used to design the flow experiments setup:

1. High image density: The number of tracer particles within an interrogation window (N_I) should be larger than 10: $N_I > 10$.
2. In-plane pair loss: During the time between two frames (Δt) within a frame pair, particles could leave or enter the interrogation area. This in-plane loss is limited by the in-plane quarter rule: $X_p < D_I / 4$.
3. Out-plane pair loss: Particles could leave the light sheet during Δt and can be limited by $Z < z_0 / 4$. Where Z is the distance travelled perpendicular to the light sheet and z_0 is the thickness of the light sheet.
4. Spatial gradients: local variation of the image displacement of the particles during Δt should be smaller than the image particle size d_τ. This can be limited by: $M_0 u_p \Delta t < d_\tau$. With M_0 as the magnification of the lens.

3.3.2. Damage experiment: Structure from Motion

The damage experiment will be carried out to assess the damage caused by long-period ship waves. The measurement technique to measure the damage is called Structure from Motion (SfM). This technique estimates three-dimensional positions from two-dimensional image sequences. By taking two or more images from different positions (P$_n$) of the same structure, a three-dimensional model can be created. This method is based on triangulation, a geometric principle that finds the three-dimensional position of a point in space by intersecting the corresponding rays of light captured in multiple camera views. By identifying the same features between images, SfM triangulates these points to estimate their three-dimensional coordinates. This can be done for every single pixel captured by the camera, resulting in a three-dimensional point cloud of the structure. An impression of the estimation of the position of the unique feature x_1 with three images is shown in Figure 3.4.

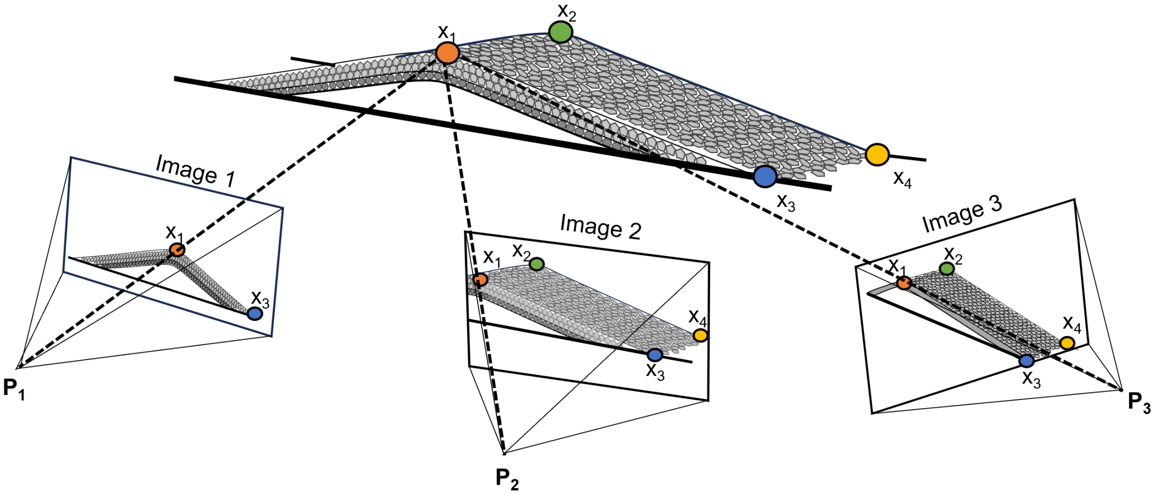

Figure 3.4: Structure from motion principle by three images taken from the physical groyne model. Unique features x_1 to x_4 are marked. Feature x_1 is captured at all images, and its location can be estimated.

During the damage experiment, the point clouds are generated by the SfM software package Agisoft Metashape in three stages. First, the software uses the supplied images and tracking algorithms to identify those unique that were captured. The features are used to link the images to each other. Ground Control Points (GCPs) are used to increase the accuracy of these unique features. These points are pre-defined markers that are placed at fixed positions around the model, resulting in the same known locations for each point could model.

The second stage of the point cloud construction is to determine the camera's intrinsic (focal length, focal point and lens distortion) and extrinsic (projection centre location and six orientation parameters) parameters by determining the optimal camera positions. Once the second stage is complete, a sparse point cloud can be constructed. The third stage uses the previously determined camera positions and the sparse point cloud to combine it with each pixel of the provided images to produce a final dense point cloud. This dense cloud is shown in Figure 3.5 as the initial profile and the damaged profile.

To measure the actual damage to the structure, two point clouds are created. The first point cloud is made from the initial profile, while the second cloud is made from a damaged profile. The differences between these clouds show the eroded and accreted areas. The initial and the damaged profiles are transferred from the Agisoft Metashape software into the computational point cloud processing software CloudCompare, to get the changes in the profile which is shown in Figure 3.5.

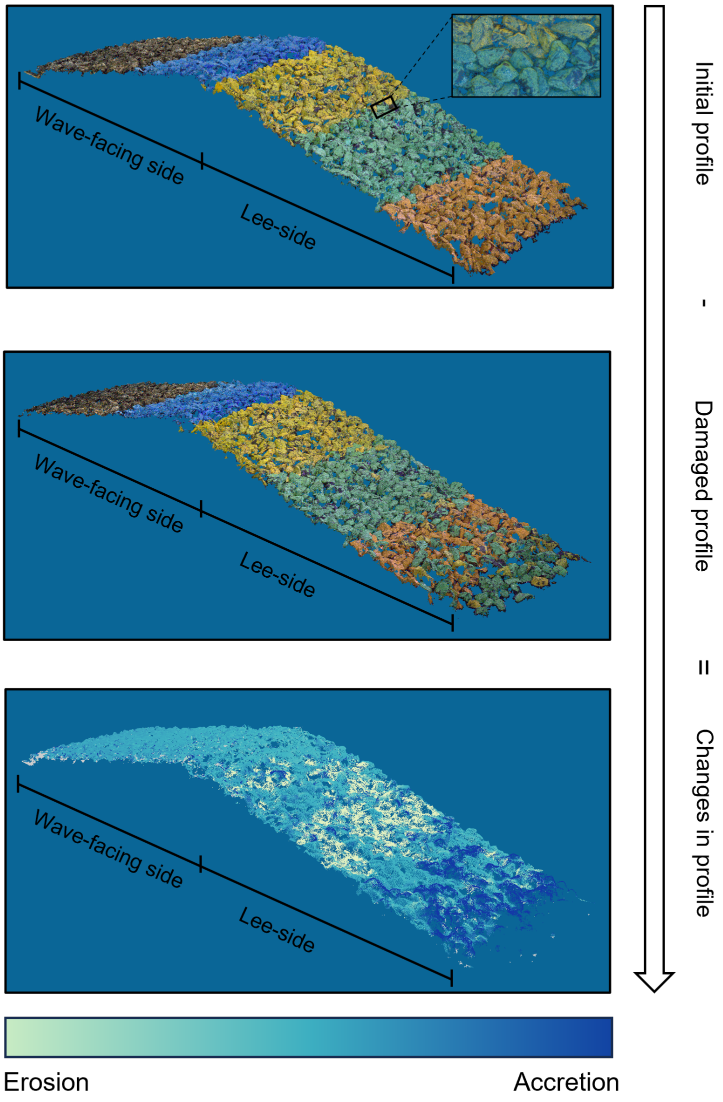

Figure 3.5: Point clouds from the initial, damaged and changes in the two profiles. Initial and damaged profiles are constructed in Agisoft Metashape. The differences between the models are obtained in CloudCompare.

.

4

Physical modelling: Experiment

Chapter 4 presents the setups of experiments. Section 4.1 introduces the testing facility and explains what is going to be measured. Section 4.2 presents the dimensions of the physical models and is followed by Section 4.3 which shows the table of measurements per experiment. The actual experimental test setups are presented in Section 4.4.

4.1. Experimental description

This section introduces the test facility where the flow and damage experiments will be conducted. This is followed by a description of the two experiments and the dimensions of the physical model.

4.1.1. Testing facility

The flow and damage experiments are conducted at the Hydraulic Engineering Laboratory of the Delft University of Technology. A tilted flume of 14.3 metres in length and 0.4 metres in width and height is used to test the behaviour of the physical models subjected to the hydraulic test conditions. The flume is shown in Figure 4.1 and consists of the experimental flume and a return flume. All physical models for each experiment are placed at a distance of 7.15 metres from the inlet of the flume. The inlet flow can be manually controlled by the inlet valve using water from the central basin of the laboratory. The water level in the flume is controlled by the manually operated weir at the end of the flume. The flow over the moveable weir flows into the return flume which returns the water back to the central water basin.

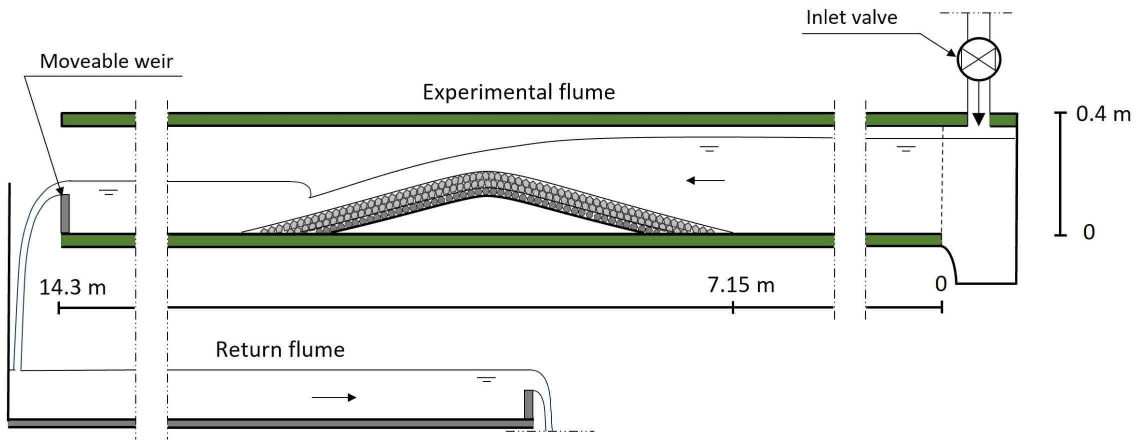

Figure 4.1: The operated tilted flume in Hydraulic Engineering Laboratory in Delft

4.1.2. Experimental descriptions and tested physical models

As stated in the Chapter 1.3 Methodology, the occurring overflowing long-period ship waves are split into two experiments: flow experiments and damage experiments.

The first experiment to be conducted is the flow experiment. The aim of this experiment is to measure the flow velocities on the lee side of the physical model and express these in a general flow velocity equation. The overflow due to primary waves is reproduced in the flume by a constant flow, as the long-period primary ship waves can be described by the quasi-steady approximation. The flow velocities measured at the tested fixed water level represent the maximum flow velocities during the wave for the same wave height. These maximum velocities are expected to cause the most damage and, therefore, gaining knowledge about these is essential. The second experiment, the damage experiment, is carried out by simulating the overflowing waves. Both experiments on physical models and the wave-structure interaction on the prototype are shown in Figure 4.2.

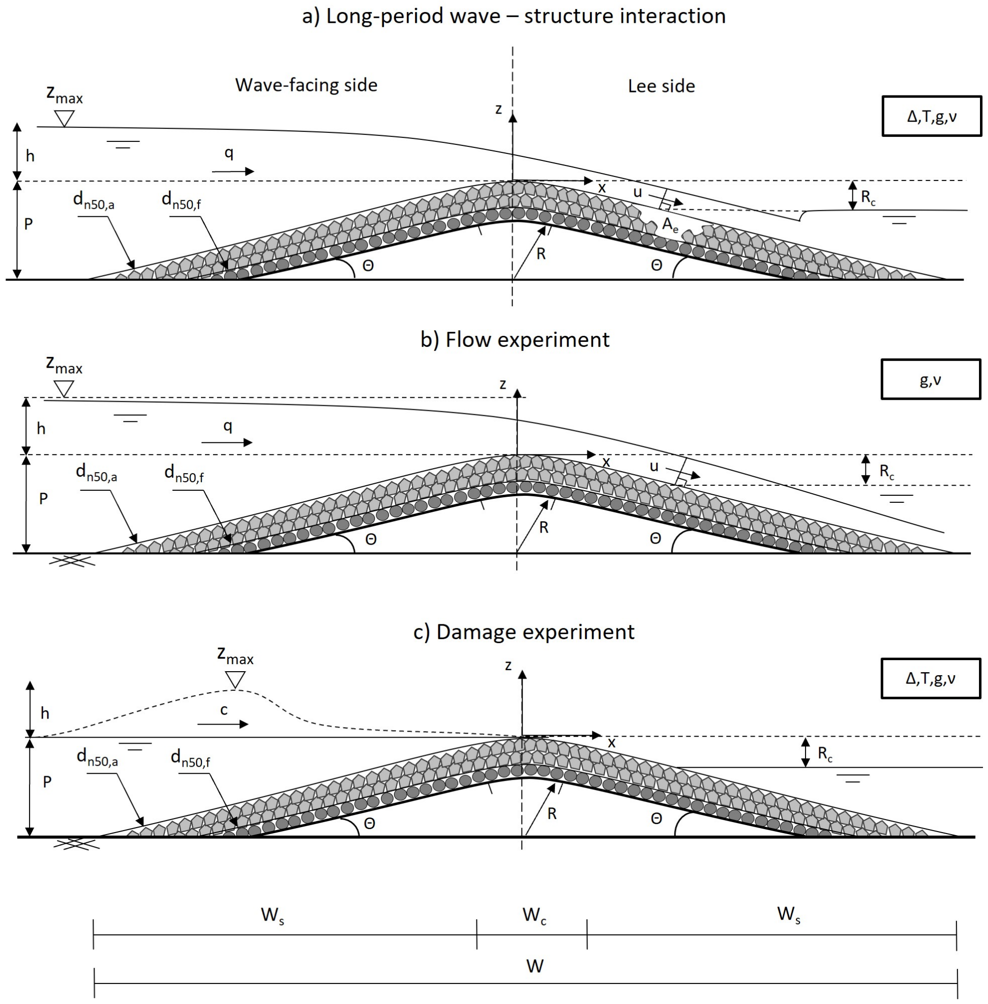

Figure 4.2: a) overflowing long-period primary wave at the prototype. b) Flow experiment with constant free flow conditions and no initial lee side water level. c) Damage experiment with recreated long-period primary waves and initial lee side water level.

Figure 4.2b shows a cross-section of a physical model during the flow experiments by a continuous overflow. The water depth above the crest height far from the structures (h) is expected to be equal to the hydraulic head at the crest. As presented in Equation 3.1, the hydraulic head ranges between $0 < h/P < 0.6$ at the prototype. To provide a more general flow velocity equation the upper limit of the h/P ratio is increased by 50% and therefore becomes $0 < h/P < 0.9$. For the same reason, the number of physical models tested during the flow experiments is increased to 4:

1. Model 1: The physical model is based on the dimensions of the prototype with a fixed armour layer consisting of rock diameter $d_{n50,a}$ = 0.019 m and slope θ = 1:4.
2. Model 2: The physical model is based on the dimensions of the prototype with a fixed armour layer consisting of rock diameter $d_{n50,a}$ = 0.013 m and slope θ = 1:4.
3. Model 3: The physical model is based on the same height as the prototype with a steeper slope θ = 1:3. The fixed armour layer consisting of rock diameter $d_{n50,a}$ = 0.019 m.
4. Model 4: The physical model is based on the same height as the prototype with a steeper slope θ = 1:3. The fixed armour layer consisting of rock diameter $d_{n50,a}$ = 0.013 m.

During the flow experiments, no initial lee side water depth is present because this interferes with the flat water surface of the overflowing flow. This is necessary for the PIV light source to penetrate the water. No lee side initial water level leads to supercritical conditions, which represent the most extreme conditions of overflowing waves.

The second experiment is the damage experiment. The aim of this experiment is to assess the damage caused to the physical groyne model by the simulated long-period primary ship waves. During this experiment, the long-period ship waves are simulated in the flume by manually varying the inlet discharge. When the target wave height is reached, the discharge is reduced until there is no overflow. The increase and decrease of the discharge are performed in the scaled primary ship wave period of T = 25 sec. Figure 4.2c shows a cross-section of this damage experiment for a long-period primary ship wave. Physical model 5 is tested in this experiment and has the same dimensions as model 1 but the attached armour layer is loose. During these tests, an initial lee side water level is preset to represent the drawdown of a passing ship.

All models have a wooden core covered with a single sheet of aluminum. A single layer of filter layer rocks is glued on top. One difference between the models of the two experiments is the armour layer. For the flow experiment, a 2 $d_{n50,a}$ thick armour layer is glued together to ensure the same model dimension per test run. On the other hand, the 2 $d_{n50,a}$ thick armour layer of the model for the damage experiment consists of loose stones, as damage should be possible. This results in a total of 5 different configurations of physical models, which are presented in the next section.

4.2. Physical model dimensions

This section presents all the dimensions of the 5 physical models that are going to be created. All calculations for the specific dimensions per diameter are presented in Appendix C.

Physical model dimensions

The largest scale ratio must be used to obtain the least scale distortions during the experiments, as stated by Chanson (2004). In addition, the physical models must meet the requirements found during the literature review in Section 2.4. The physical model is scaled according to Froude similarity, which means that the Froude number of the prototype is equal to the Froude number of the physical model.

$$Fr_p = Fr_m \rightarrow \left(\frac{u}{\sqrt{gL_r}}\right)_p = \left(\frac{u}{\sqrt{gL_r}}\right)_m \tag{4.1}$$

This results in a scaling ratio of L_r = 13, which is the largest dimension that would fit in the flume in combination with the desired hydraulic conditions that can be tested. All dimensions per model are presented in Table 4.1.

Rock dimensions armour layer

The prototype rock grading used in the armour layer is $LM_{B5/40}$ with a corresponding d_{50} of 18-23 cm. The material of the prototype rock is iron-silicate which has a specific density of about 3800 kg/m^3. This material is relatively rare for the construction of rock structures in the Netherlands. Therefore, in addition to the Froude scaling, an additional scaling method based on the Izbash equation is used. The use of this equation makes it possible to have a different rock material.

This scaling method is important for the damage experiment to achieve the same stability as the prototype. The armour layer of model 5 is therefore scaled by using the Izbash equation. To research the effect on flow velocity over the differently scaled rock size, models 1 and 3 are equipped with this rock size as well. The Izbash stability equation includes the densities of the rock and water, by the relative density $\Delta = (\rho_s - \rho_w)/\rho_w)$, rock diameter ($d_{50}$) and critical flow velocity (u_c). The unknown model rock diameter is determined by equalizing the Izbash formula of the prototype to the model, as shown in Equation 4.2. The unknown critical velocities are expressed using the scaling ratio, based on Froude similarities.

$$\left(\frac{u_c}{\sqrt{\Delta g d_{50}}}\right)_p = \left(\frac{u_c}{\sqrt{\Delta g d_{50}}}\right)_m \tag{4.2}$$

As mentioned above, the prototype rock material iron-silicate (ρ_s = 3800 kg/m^3) is unavailable to use for the physical model of the groyne structure. Normally a standard rock material such as granite has a specific weight of around 2600 kg/m^3. An available material with a higher specific weight compared than normal stone material is Basalt, which has a specific weight of approximately ρ_s = 2800 kg/m^3. This results in a model rock diameter $d_{50,m,basalt}$ = 0.022m to be applied as rock armour for the physical models 1, 3, and 5 when using the basalt rock material.

The Froude similarity is still used to scale the rock sizes for models 2 and 4. These models are tested during the flow experiments and the density of the rock is not important due to the glued armour layer. The rock armour of models 2 and 4 is made of the rock material granite and scaled by Froude similarity. This results in the $d_{50,m,a,granite}$ = 0.015m.

Rock dimensions filter layer

The prototype rock grading used in the filter layer is CP 90/250 with a corresponding d_{50} of approximately 17 cm. The material of these rocks is also iron-silicate which has a specific density of approximately 3.8 t/m^3. The model filter layer is going to be glued to the aluminum sheet of all models, so specific density is unimportant for the scaling. Therefore, this filter layer is scaled using Froude similarity, which results in a rock diameter of the filter material at the model of $d_{50,f}$ = 0.013 meters.

All dimensions of all models are summarized in Table 4.1.

Table 4.1: Dimension of parameters of the physical models with nominal stone diameter.

	Prototype [-]	Model 1 Flow	Model 2 Flow	Model 3 Flow	Model 4 Flow	Model 5 Damage
P [m]	2.33	0.179	0.179	0.179	0.179	0.179
W_c [m]	2	0.154	0.154	0.154	0.154	0.154
W_s [m]	8.5	0.654	0.654	0.508	0.508	0.654
W [m]	19	1.462	1.462	1.170	1.170	1.462
θ [-]	1:4	1:4	1:4	1:3	1:3	1:4
R [m]	3.9	0.3	0.3	0.3	0.3	0.3
Armour material	Iron silicate	Basalt	Granite	Basalt	Granite	Basalt
ρ_s [kg/m^3]	3800	2800	2600	2800	2600	2800
$d_{n50,a}$ [m]	0.168	0.019	0.013	0.019	0.013	0.019
$d_{n50,f}$ [m]	0.143	0.010	0.010	0.010	0.010	0.010
Attachment	Loose	Fixed	Fixed	Fixed	Fixed	Loose

4.3. Hydraulic conditions experiments

A table of tested hydraulic conditions has been prepared for both experiments. For the flow experiment, models 1, 2, 3 and 4 are tested for the increased hydraulic condition 0.3 < h/P < 0.9 and there is no initial lee side water level. The minimum value is increased because too low water levels will not meet the physical modelling requirements, as described in Chapter 2.3. For the damage experiment, model 5 is tested for the hydraulic condition 0.2 < h/P < 0.8 with a lee side water level of 0 < R_c/P < 0.61.

4.3.1. Hydraulic conditions flow experiment

Flow velocities at the lee side of models 1, 2, 3 and 4 are measured using the PIV system. Six different hydraulic heads at the crest level are tested for the corresponding flow velocities. Three runs of 20 seconds each are carried out for each hydraulic head in order to determine potential false measurements. As there are four models, this leads to a total of 60 individual measurements. The first three hydraulic heads tested are based on field measurements as described in Chapter 3.1.2 and are extended by two additional hydraulic heads to account for potential increased wave heights in the future. Table 4.2 presents an overview of the tests for the flow experiments.

Table 4.2: Table of hydraulic conditions for flow experiment for models 1 to 4

			Measured range			Extended	
			0.3 <h/P <0.6			0.6 <h/P <0.9	
			h (cm)			h (cm)	
		Model dimension	5.4	8.1	10.8	13.5	16
		Prototype dimension	70.2	105.3	140.4	175.5	208
Model 1,2,3,4	Run	1					
		2					
		3					

4.3.2. Hydraulic conditions damage experiment

The lee side damage of model 5 is measured using the Structure from Motion principles. First, the damage is assessed for four measured wave heights and four measured freeboard water levels R_c on the wave-facing side. These are based on the field measurements at the actual prototype. The ranges are extended to observe the effects of increased loads that could occur in the future. Table 4.3 shows all the hydraulic conditions tested during the damage experiment.

Table 4.3: Table of hydraulic conditions for damage experiment for Model 5

					Measured range				Extended	
					0.2 <h/P <0.6 h (cm)				0.7 <h/P <0.8 h (cm)	
			Model		3.6	5.4	8.1	10.8	12.5	14.3
				Prototype	46.8	70.2	105.3	140.4	162.5	185.9
Extended	R_c / P = 0.61	R_c (cm)	10.9	141.7						
Measured range	0 <R_c / P <0.46	R_c (cm)	8.2	106.6						
			5.5	71.5						
			2.7	35.1						
			0.0	233						

4.4. Experimental setups

Both experiments are conducted in the same tilted flume at the Hydraulic Engineering Laboratory at the Delft University of Technology. The setups of both experiments are presented in this section.

4.4.1. Test setup flow experiments

The flow velocities at the lee side of the physical models are measured by using PIV and the four corresponding PIV design rules should be fulfilled. These rules are described in Chapter 3.3. A CMOS camera (FLIR Oryx 2448 x 2048 pix^2, pixel size d_τ = 3.45 μm) is positioned perpendicular to the glass sidewall. Attached to the camera is the Fujinon TV Lens HF12.5SA-1 with an aperture of F1.8 and a focal length of 12.5 mm. The distance between the camera chip and the LED light sheet is 1.0 metres, providing a field of view of approximately 535 x 445 mm in width and height. The LED light sheet is placed in the centre of the flume, where there is the least interaction of the flow with the side wall. It shines from the top onto the armour layer of the models illuminating 600 mm in length and 6 mm in width. The light sheet illuminates 77 mm in front of the crest top and 523 mm of the lee side slope of models 1, 2, 3 and 4. The entire setup is covered to block ambient light. The flow is seeded with tracer particles Vestosint 1101 (d_p = 100 μm and ρ_p = 1060 kg/m^3). A separate seeding device is designed to inject the tracer particles into the flowing water and is called the Seeding device. It consists of a container of water with a concentration of 50 g/L of particles, a mixer, a pump and an outlet. The device is placed vertically from the top into the water directly at the toe of the structure. It injects the particles directly into the same direction as the flow by 16 horizontal tubes of 19 cm. By using this concentration, all the tested hydraulic conditions fulfilled the first PIV rule to have more than 10 tracer particles per interrogation window sized D_I = 32 pix (0.007 m). The operated PIV setup elements are presented in Table 4.4 and the setup is shown in Figure 4.3. The wave-facing side water levels are measured by a point needle at 1.0 meters in front of the toe of the structure and marked by M in the figure. Furthermore, the water levels were measured at the crest by a point needle before a PIV measurement was performed and a calibration procedure as explained in Appendix F was followed. All PIV setup details are presented in Appendix F.

Table 4.4: PIV setup elements used during the flow velocity experiment

PIV setup Element	Product name
LED light	DrewLear VLX2-500 600mm
Tracer Particles	Vestosint 1101 100 µm
Lens	Fujinon TV Lens HF12.5SA-1 1:1.4/12.5mm
Camera system	Oryx ORX-10GS-51SM-C
Data analysing program	MatLab package PIVLab

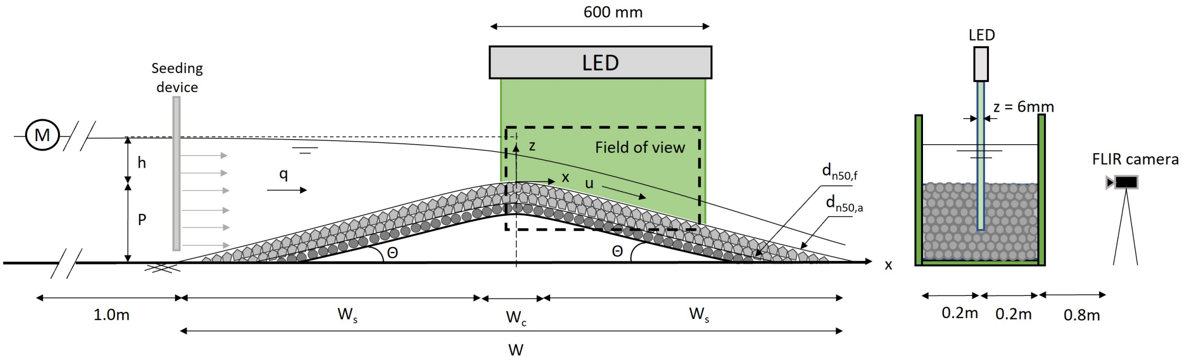

Figure 4.3: Side view of the test setup in the flume during the flow experiments. Left: Side view of the physical model with the light sheet (green) and the seeding system at the toe of the structure. Right: Front view of the flume with the distances between the LED light source and camera.

The camera and LED light sheet are triggered at the same frequency of 20 Hz. A single measurement run is 20 seconds and results in 400 single frames and therefore 200 frame pairs. To comply with the second PIV rule: 'In-plane pair loss', the time between two taken frames within a frame-pair is changed per tested hydraulic depth, due to the larger travelled particle distance at larger hydraulic heads. The travelled distance of the particles must be smaller than 1/4 of the size of the interrogation window. During the experiment, the time between two light pulses (Δt) varied from 1300 μs for the smallest hydraulic heads up to 800 μs for the largest. The illumination time per frame was set to 100 μs to have sufficient light intensity to observe the particles meanwhile the movement of the particles during a light pulse was too small to observe by the camera. The third PIV rule: 'Out plane pair loss' states that the travelled distances of the particles perpendicular to the light sheet must be smaller than 1/4 of the width of the sheet. This light sheet is 6 mm in width, which is approximately the same width as the used interrogation window of 7 mm. The main flow is significantly larger in the parallel direction and therefore it is presumed that the third PIV rule is fulfilled. The last PIV rule: 'Spatial gradients' is satisfied when the local variation of the image displacement during Δt is smaller than the image particle size (d_τ). During all the experiments the spatial gradient was equal to or smaller than 2.6 μm whereas the image particle size was constant 2.7 μm. Therefore the last PIV rule is fulfilled. All specific conditions and corresponding parameters per test are presented in Appendix F.

The duration of each test run is set to 20 seconds, as the moving average of the flow velocity approaches the average within a deviation of less than 0.5 % after 8 seconds, as shown in Figure 4.4. The figure shows the normalized flow velocities based on the crest flow velocity of model 2 for the tested hydraulic heads. To ensure this level of accuracy, the total measurement duration is increased to 20 seconds per run.

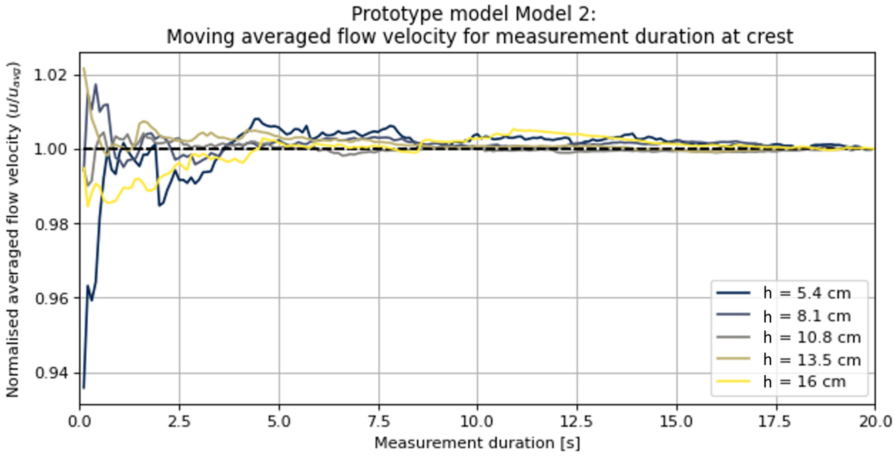

Figure 4.4: The normalised average flow velocity of the different tested hydraulic heads at the crest of physical model based on the prototype: Model 2.

4.4.2. Test setup damage experiment

Physical model 5 is tested for occurring damage caused by overflowing primary ship waves. The damage is measured based on Structure from Motion principles as described in Chapter 3.3. The tested physical model is divided into five zones, which are given different colours to make it easier to identify the stone displacements, and is shown in Figure 4.5. The first and second zones are marked by the orange and green stones respectively and start from the toe at the lee side of the structure. The third and fourth zones are marked in yellow and blue respectively. These zones cover the crest. The fifth zone remains uncoloured as the damage is expected to be on the lee side and is therefore of no interest in this zone. The wave heights are measured at the same location as water depth measurements during the flow experiments, namely 1.0 metres in front of the toe of the structure.

A Canon EOS 2000D camera (6020 x 4015 pix^2) is used to capture at least 21 images from above, perpendicular to the armour layer of the models. These images are used to perform the Structure from

Motion principles. All images per model had an overlap of at least 50%. The corresponding positions of the images are marked by the red crosses in Figure 4.5. The EFS 18-55mm lens was used and fixed at a focal length of 29mm in combination with an aperture of F/22. Pictures were taken at ISO 1600 with a shutter speed of 1/10th of a second. All images were taken handheld in RAW format and converted to TIFF files with no loss of quality. This conversion improves the reconstruction of the images into a three-dimensional model using the Agisoft Metashape software.

To increase and check the accuracy of the Structure from Motion models, twenty different Ground Control Points (GCPs) are placed in pairs around the physical model. The GCPs are printed on aluminium plates with a polymer core that is waterproof and has high rigidity. Therefore, eight GCPs (GCP1, 2, 7, 8, 21, 22, 23 & 24) are placed at the bottom of the flume in front and behind the structure. The advantage of this location is that the GCPs are better in focus as the height difference between the structure and these GCPs is small. However, the disadvantage of these locations is the potential scratching of the GCPs by the moving rocks due to an overflowing wave. Therefore, twelve GPCs (GCP3, 4, 5, 6, 9, 10, 13, 14, 15, 16, 17 & 18) are fixed to the upper sides of the flume. These GCPs remain dry, and untouched and are less likely to move over time. However, due to this height difference between the GCPs and the model, it is harder to get the model and the GCPs in focus. Therefore, all GCPs are combined to improve the construction of the three-dimensional point cloud. Combining the GCPs at the flume bed and the ones above the model results in a reduced calculated averaged position error of 0.171 pixels (0.582 mm). All errors per individual model including the position of the GCPs are presented in Appendix G.

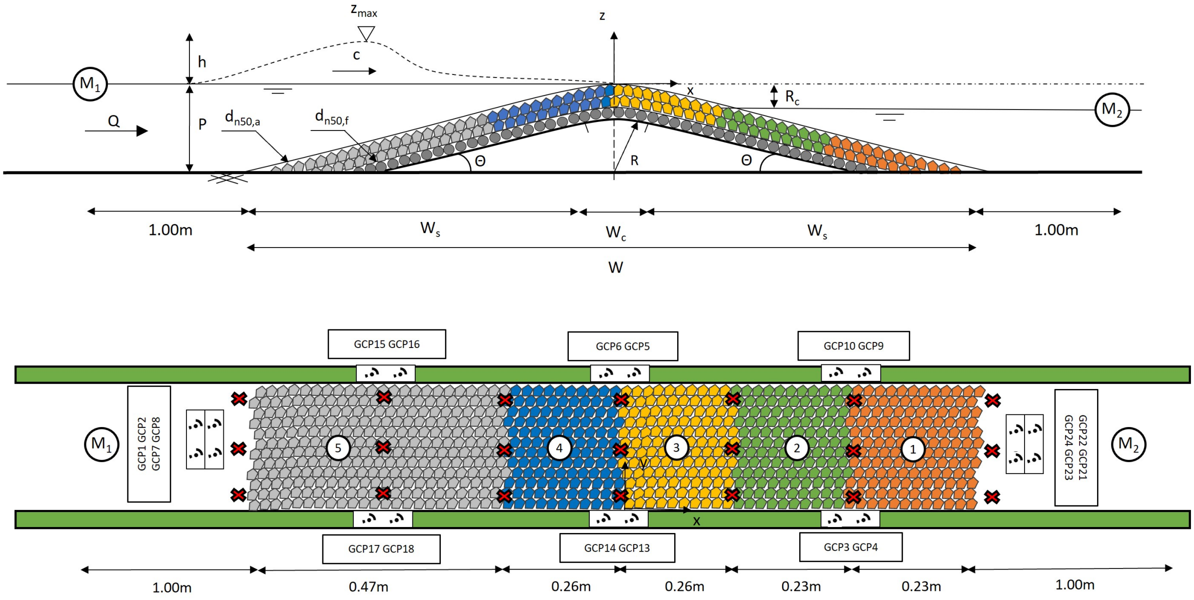

Figure 4.5: Side view of the test setup in the flume during the damage experiment. Top: side view of model 5 with the assigned colours at different locations. Bottom: Top view with an overview of the Ground Control Points (GCP) and camera positions (red crosses).

5

Flow experiment test results

This chapter presents the analysis and results of the measurements made during the flow velocity experiment. First, the method used to analyse the PIV images is explained in Section 5.1. In combination with section 4.4.1, this leads to the answer to sub-question 1: 'How could a Particle Image Velocimetry (PIV) setup be applied to measure the flow velocity at the lee side of the groyne?'. Sections 5.2 and 5.3 present the results of the flow experiments and show the corresponding flow equations leading to the answer to sub-question 2: 'How could the flow velocity at the lee side of a groyne structure be expressed in a mathematical equation under free flow conditions?'. Section 5.4 presents the applicability of the theoretically developed flow velocities. Finally, in Section 5.5 the answers to questions 1 and 2 are summarised and discussed.

5.1. Flow velocity analysis

To analyse the flow velocities, five locations along the lee side were used to extract the flow velocity profiles. The first extraction line (L_c) is positioned at the crest of the models. The other four extraction lines are placed perpendicular along the lee side slope ($L_{s1,2,3,4}$), as shown in Figure 5.1. At each of these locations, the flow velocity is extracted over the water depth. This results in a flow velocity profile per position perpendicular to the armour layer. The coordinates of the lines at the armour layer are given in Table 5.1, including the assumed corresponding freeboard R_c. The depth-averaged velocity is used to determine the flow velocity equations presented in Chapter 3.2.

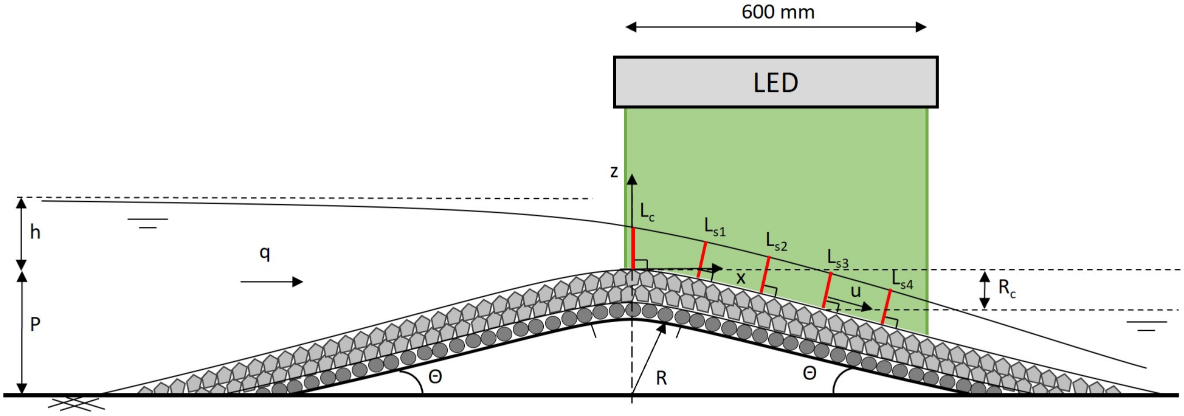

Figure 5.1: Side view of the physical model in the flume during flow velocity experiment with locations of the extracted lines marked in red.

Table 5.1: Coordinates of the extraction lines at the armour layer and corresponding assumed freeboard R_c [m]

	Model 1		Model 2		Model 3		Model 4	
Line	(x,z)	R_c [m]	(x,z)	R_c [m]	(x,z)	R_c [m]	(x,z)	R_c [m]
L_c	(0,0.0)	0	(0,0)	0	(0,0)	0	(0,0)	0
L_{s1}	(0.076,-0.005)	0.005	(0.078,-0.006)	0.006	(0.064,-0.002)	0.002	(0.066,-0.001)	0.001
L_{s2}	(0.188,-0.030)	0.03	(0.172,-0.027)	0.027	(0.162,-0.020)	0.020	(0.165,-0.022)	0.022
L_{s3}	(0.332,-0.075)	0.075	(0.282,-0.063)	0.063	(0.274,-0.116)	0.116	(0.290,-0.067)	0.067
L_{s4}	(0.477,-0.119)	0.119	(0.463,-0.112)	0.112	(0.445,-0.125)	0.125	(0.433,-0.119)	0.119

The captured frames are processed using the MATlab package PIVLab. All four physical models were tested for five different hydraulic heads. Each hydraulic head was tested in three runs for 20 seconds at a frame rate of 20 Hz, resulting in 400 frames and thus 200 frame pairs. In approximately 1% of the frames captured, a frame was not saved or not processed. This resulted in not all frame pairs being valid and therefore had to be removed. However, the number of frame pairs in a single run was never lower than 198. The correct frames were imported to PIVLab and pre-processed applying Contrast Limited Adaptive Histogram Equalization (CLAHE) and Auto-Contrast filters. The CLAHE filter increases the readability of the image data. Regions with low exposure and regions with high exposure are therefore optimized independently. CLAHE improves the probability of detecting valid displacement vectors in frames by 4.7 ± 3.2 % (Thielicke & Stamhuis, 2014). The Auto-Contrast filter automatically calculates the best contrast per frame to improve the visibility of the particles. The Discrete Fourier transform (DFT) method is used to calculate the correlation matrix in the frequency domain. This method uses 20% of the computational time compared to the Direct Cross Correlation (DCC) method (Thielicke & Stamhuis, 2014) and is preferred due to the large number of performed tests. A disadvantage of the DFT function is the increase in background noise as it uses a fixed interrogation window. To reduce the potential background noise, two passes are used with interrogation window sizes of 32x32 pixels and 64x64 pixels respectively. The Gaussian 2x3 point function is applied to determine the peak in the correlation matrix. After analysis, a certain amount of noise is unavoidable and therefore a standard deviation of 2 and a local median filter of 3 is applied during the post-processing.

5.2. Flow velocity results

The flow over the physical models is expected to behave differently due to the difference in slope (Θ) and stone size in the armour layer ($d_{n50,a}$). Figure 5.2 shows the mean velocity field for 20 seconds of data for each tested model at a hydraulic head of 10.8 centimetres. The figure shows the 45 millimetres in front of the crest and the 490 millimetres of the lee side slope. The flow velocity at the crest is about 0.8 m/s and accelerates along the slope up to 2.2 m/s. The corresponding measured water level at the crest h_c of each model is approximately 2/3 of the hydraulic head, which is to be expected as the flow is in critical conditions. After the crest, the flow accelerates and starts to be in the supercritical state (Fr > 1).

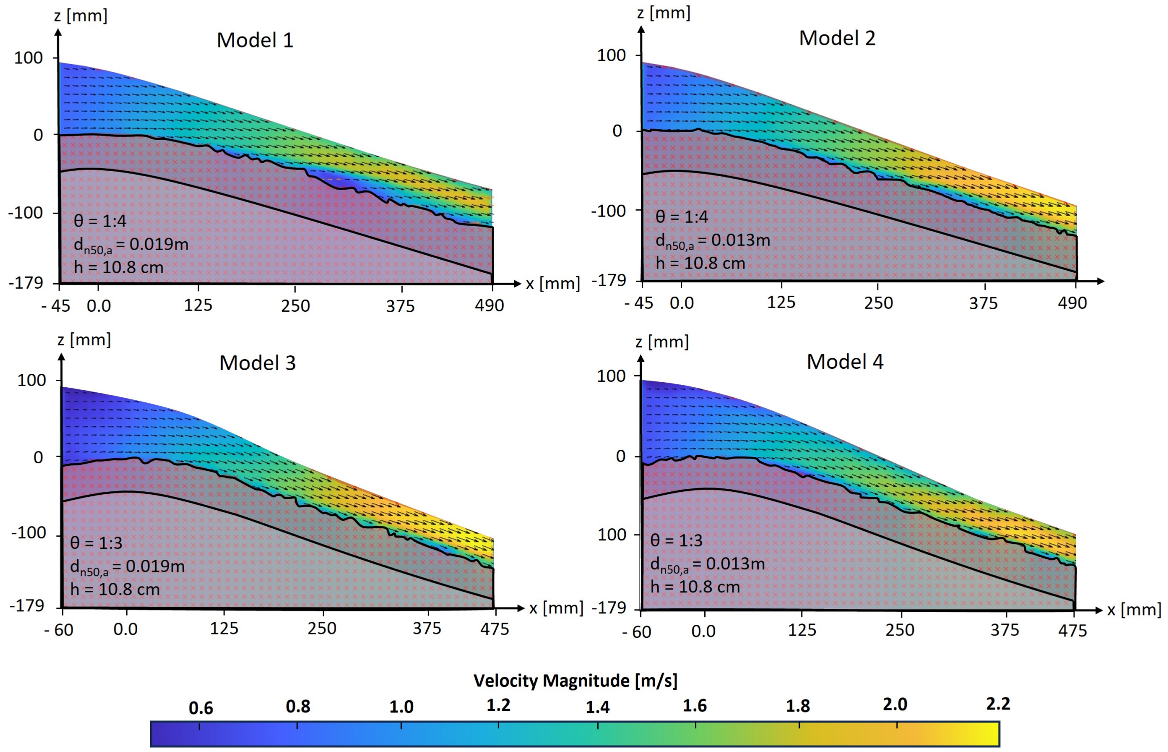

Figure 5.2: Flow velocity fields of models 1 to 4 for the hydraulic head of 10.8 cm.

5.3. Flow velocity equations

The depth-averaged flow velocity of the velocity profiles at L$_{s1,2,3,4}$ is calculated per run per tested water level. These are used to determine the first flow velocity equation, as presented in Chapter 3.2 and shown in Equation 5.1. h is the hydraulic head at the crest or water level above the crest height in front of the structure. At the bed level positions of L$_{s1,2,3,4}$ it is assumed to be the lee side water level, which is expressed in freeboard R_c.

$$u = \alpha\sqrt{2g(h + R_c)} \tag{5.1}$$

Figure 5.3 shows the results of the measured depth-averaged flow velocities for each tested water level per extraction line. A regression analysis is performed to determine the correction factor α of each equation. These factors are also shown in the figure as well. The α-factor expresses the influence of the different rock diameters and slopes on the flow velocity. Models 1 to 4 have an α-factor of 0.78, 0.86, 0.82 and 0.84 respectively. The increase in the α-factors of models 1 and 2 can be explained by the decrease in the rock size, possibly resulting in less friction and turbulence. The α-factors of models 3 and 4 show a slight increase as rock size decreases. This could mean that for slopes steeper than 1:4, the tested boulder sizes are less important for the alpha factor than the slope.

Nevertheless, all α values are close to each other and could be represented in a single flow equation. Furthermore, the used flow velocity equation including the square root correlation, presented in Equation 5.1, overestimates the velocities at the smaller $h + R_c$ values and underestimates the velocities at the larger $h + R_c$ values. Therefore, an optimised flow velocity equation for all 4 physical models is presented in Equation 5.2 and shown in Figure 5.4. For an α parameter of 0.67 and to the power b of 0.67, the R^2 value is increased to 0.90 instead of 0.81 for the square root flow equation.

$$U_{avg} = 0.67 * (2g(h + R_c))^{0.67} \tag{5.2}$$

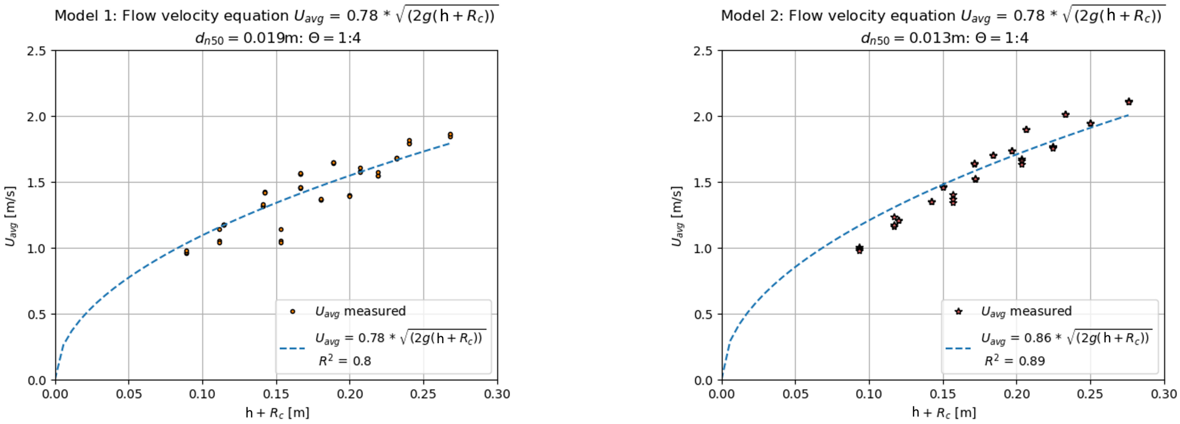

(a) Overflow velocities model 1

(b) Overflow velocities model 2 (represents prototype)

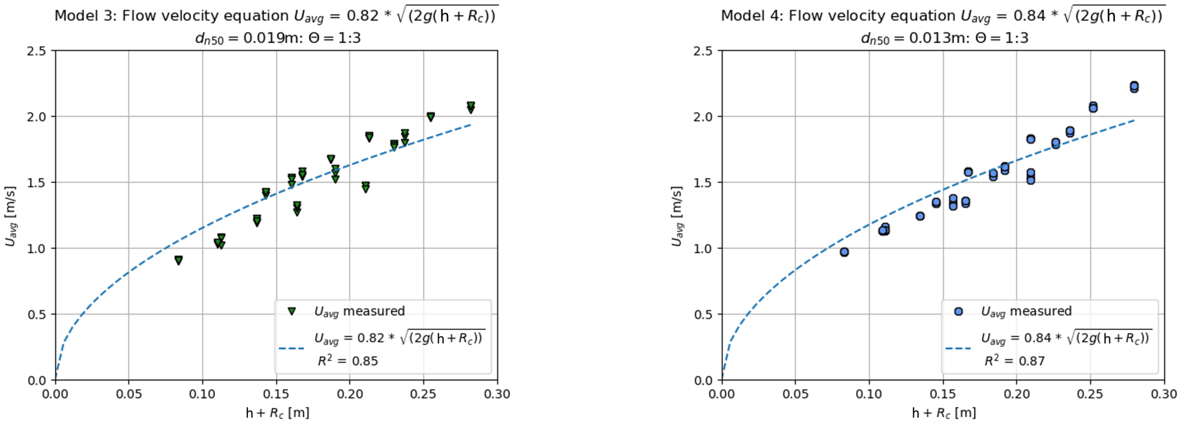

(c) Overflow velocities model 3

(d) Overflow velocities model 4

Figure 5.3: Depth averaged flow velocities measured at the extraction lines at lee side $L_{s1,2,3,4}$.

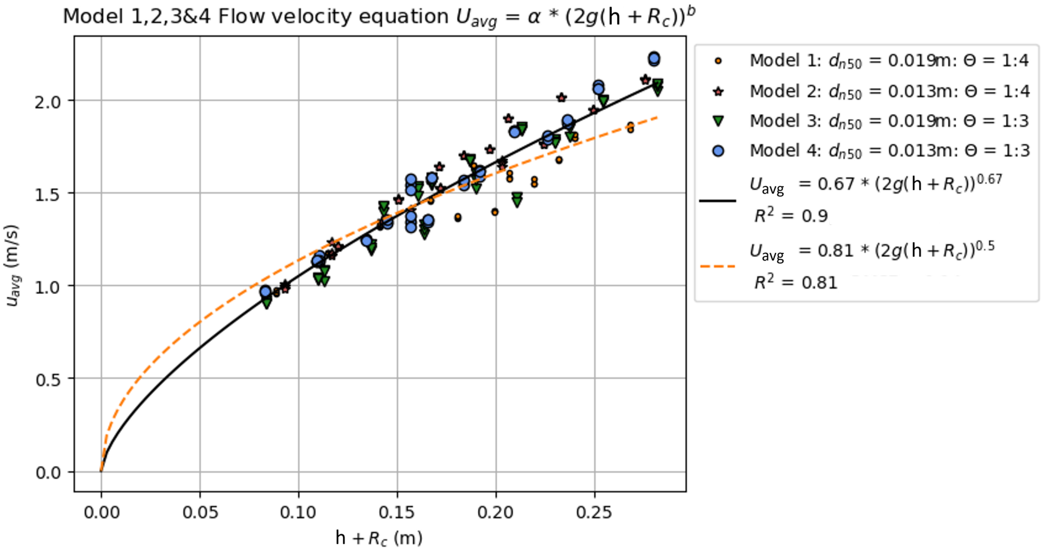

Figure 5.4: Optimised flow velocity equation and flow velocity equation based on the square root for all measurements at all models.

Equation 5.2 shows the flow velocity equation for two different rock sizes and slopes. To determine the velocities for possible other rock sizes and/or slopes, the flow velocities are expressed into a dimensionless equation. This determination of the equation has already been shown in Chapter 3.2. A dimensionless equation is constructed by plotting the dimensionless depth averaged velocity of each measured data point against the slope (Θ), nominal stone diameter (d_{n50}) and extraction location of each model (assumed freeboard level R_c). This regression is shown in Figure 5.5 and follows the dimensionless equation as presented in Equation 5.3.

$$U_{avg}/\sqrt{(gh)} = 1.95 - 0.88 * exp(-0.51 * \Theta R_c/d_{n50}) \tag{5.3}$$

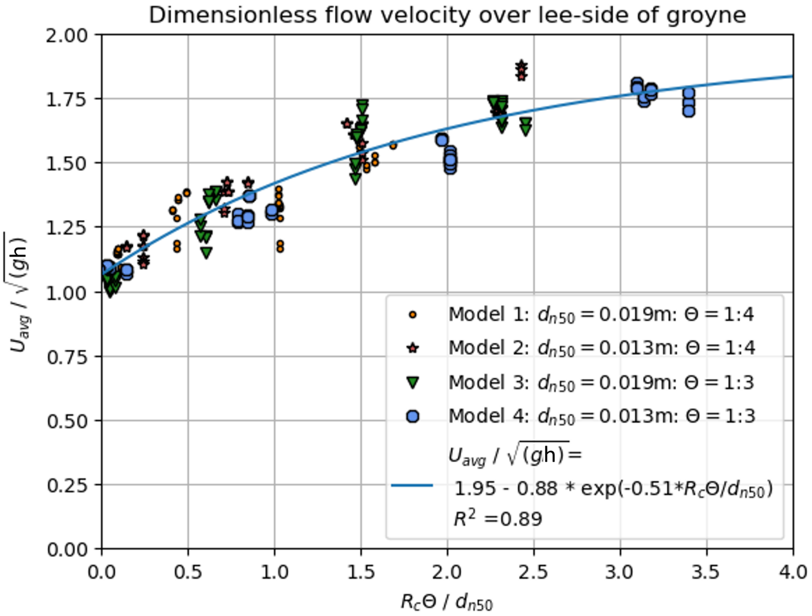

Figure 5.5: Dimensionless flow velocity equation in supercritical conditions for upstream water levels above crest level (h), assumed lee side water level (R_c), nominal stone diameters (d_{n50}) and slopes (Θ)

5.4. Developed flow velocity

The measured flow velocities at the crest and lee side slope are used to check the validity of the developed flow based on the Manning equation, presented during the literature review in Chapter 2.2.2. The equation is repeated in Equation 5.4. Here, u_d is the mean flow velocity for the developed flow along a slope based on the measured flow velocity at the crest of the structure. R_h is the hydraulic radius and θ is the slope. k_s is the Strickler coefficient with $k = \theta * d_{50}$, b_1 = 12.21 and b_2 = 0.159 for crushed dumped rocks according Abt et al. (1987).

$$u_d = k_s * R_h^{2/3} * \theta^{1/2} \tag{5.4}$$

$$k_s = \frac{b_1}{k^{b2}} \tag{5.5}$$

The result of the measured flow velocities per tested water level compared to the theoretically developed flow velocities is presented in Figure 5.6. All flow velocities are expressed in terms of the corresponding specific discharge (q). The measured flow velocities start at the crest and increase in velocity when they travel along the lee side slope. The theoretically developed flow velocity is not reached within the measured region of interest. The level of increase between the measured velocities along the slope for a single tested water level decreases before the theoretically developed flow is reached. This indicates that the theoretically developed flow velocity is probably too high to be reached along the groynes slope.

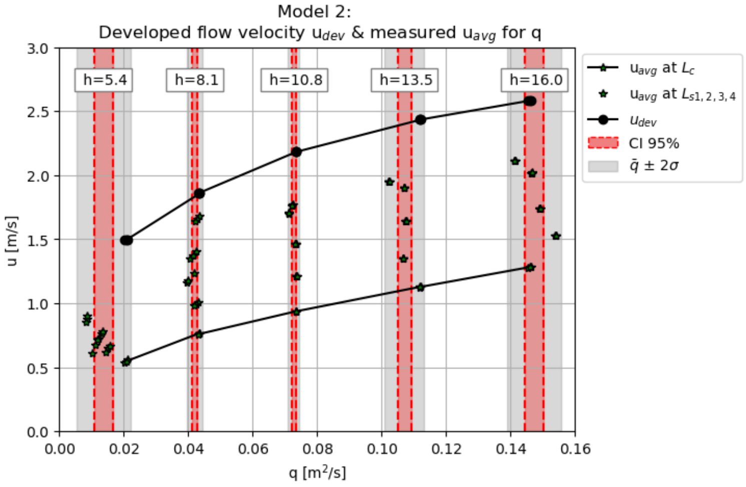

Figure 5.6: Measured flow velocities (u$_{avg}$) at the crest and lee side slope per tested h for Model 2, representing the prototype, compared to corresponding developed flow velocity (u$_{dev}$).

Next, per tested water level is a range of 2 standard deviations (σ) around the mean specific discharge ($\overline{q}$) presented in Figure 5.6. Furthermore, the 95% confidence interval based on the Student's t distribution is shown. Expressing the standard deviation divided by the mean specific discharge shows that the coefficient of variation (CV) around h = 5.4 cm is significantly larger than the other four tested h. Therefore, the h = 5.4 cm is discarded for all models and in any of the presented flow equations. Appendix H presents the expected cause for this problem.

Table 5.2: Measured mean specific discharge, standard deviation, coefficient of variation and developed flow velocity

h [cm]	$\overline{q}$ [m^2/s]	σ [m^2/s]	CV = σ / $\overline{q}$ [%]	u$_{dev}$ [m/s]
5.4	0.0136	0.0042	30.7	1.49
8.1	0.0421	0.0012	2.9	1.86
10.6	0.0727	0.0009	1.2	2.18
13.5	0.1070	0.0031	2.9	2.43
16	0.1473	0.0042	2.8	2.58

The flow within the field of view during the measurements is smaller than the developed flow velocity based on Equation 5.4. Therefore, the flow velocities of all models are normalised to their position at the lee side to check which length is needed to reach the developed flow velocity, as shown in Figure 5.7. All flow velocities were measured within 75% of the lee side slope and reached about 80% of the developed flow velocity. Based on extrapolation, the developed flow velocities are reached when the length of the lee side slope is 2 times greater than compared to its actual length. Therefore, by using the developed flow equation the maximum flow velocities are overestimated by about 10%.

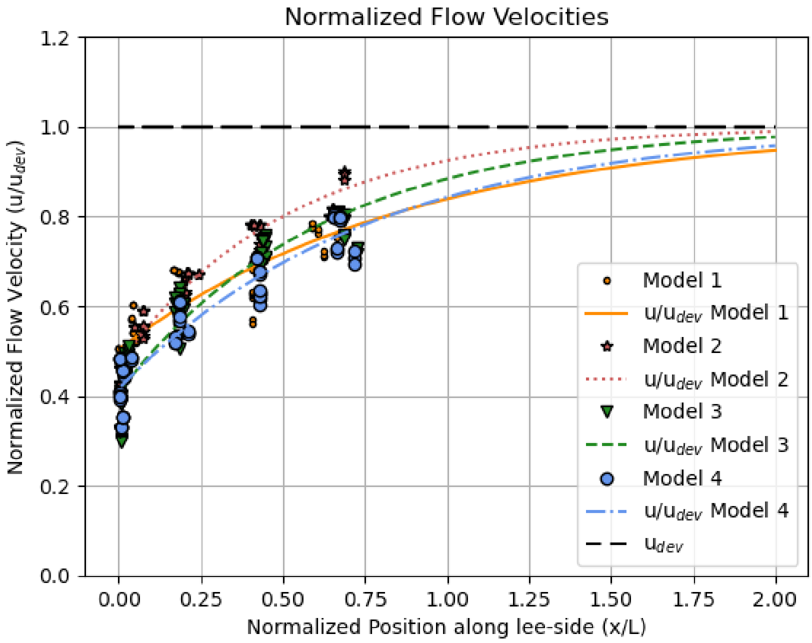

Figure 5.7: Normalized flow velocities and corresponding positions for all models measured along the lee side slope

5.5. Discussion of sub-question 1 & 2

The answer to research sub-question 1: *'How could a Particle Image Velocimetry (PIV) setup be applied to measure the flow velocity at the lee side of the groyne?'* was presented in two parts, namely in Section 4.4.1 and Section 5.1. The field of view used during the measurements covered the crest and 70% of the lee side slope of the models. The field of view was the maximum view within the light sheet. The lowest 30% of the lee side slope of the models were therefore not measured. Nevertheless, the lowest extracted flow velocities were measured at an assumed freeboard of 12.5 cm. This assumed freeboard is 2 cm greater than the maximum freeboard that is going to be tested during the damage experiment. As the flow can't accelerate freely when it interacts with the water level at the freeboard, it is expected that measuring flow velocities below the maximum tested freeboard during the damage test is not necessary. Therefore the last 30% of the lower lee side slope is unnecessary to measure.

The measurement of flow velocities along the measured slope are all without an initial pre-set lee side water level. If such a water level was preset, it resulted in an unstable water surface flowing over the structure. This led to refraction and blockage to the LED light sheet and therefore no measurement could be taken. By using no initial lee side water level, the overflowing water level remained stable and flat. It results in flow conditions that are super-critical, which are the upper bound of the flow velocities of an overflowing flow. Although a lee side water level can result in sub-critical flow velocities, the super-critical flow velocities provide a conservative yet safer approximation determining the stability of the structure.

Sub-research question 2: *'How could the flow velocity at the lee side of a groyne structure be expressed in a mathematical equation under free flow conditions?'* is answered in Section 5.3. Two flow velocity equations are determined: a dimensional flow equation with variables h and R_c and a dimensionless flow equation based on h, R_c, Θ and d_{n50}. Both equations can be used under free-flow equations and for waves that can be described by the quasi-steady approximation. The dimensional flow equation represents the flow velocities for two slopes and two rock sizes, indicating that the flow velocity difference between the overflowing of the four models is small. However, the dimensional and dimensionless equation must be tested for other rock diameters to check which limits the flow equation holds.

Besides the two designed flow velocity equations, the theoretically developed flow velocity is checked on its applicability to the overflowing flow. It is determined that at the toe of the lee side sloped structure, the velocities are reaching 90% of the developed flow. The structure lee side slope should be twice as long in order to reach the developed flow velocity. Furthermore, the developed flow is based on no lee side water level to reach the corresponding developed state. In the case of a lee side water level, the flow stops from accelerating when the overflow interacts with the lee side water level. Therefore, the flow velocities are expected to not reach the developed state at the current structure with a lee side water level.

6

Damage experiment test results

This chapter presents the results of the damage experiment. Section 6.1 presents the method that is used to determine damage parameters from the constructed 3D models. Section 6.2 shows the results of the experiments. This answers sub-question 3: 'How could the damage due to groyne overflowing caused by long-period primary ship wave loadings be expressed in terms of damage parameters S, E_{2D} and E_{3D}?'. Section 6.3 presents the damage limits leading to the answer to sub-question 4: 'How to characterize damage limits (initial damage, intermediate damage, and failure) for groynes exposed to long-period primary ship wave loadings in shallow and confined waterways?' In addition, the failure limits of the structure are presented in Section 6.4. Finally, the answers to sub-questions 3 and 4 are discussed in Section 6.6.

6.1. Damage experiment analysis

The damage during the damage experiment is measured by comparing the profile differences of the initial structure and the damaged structure using Structure from Motion principles (see Chapter 3.3.2). By taking 21 2D images perpendicular to the armour layer, a 3D point cloud model of the initial or damaged structure was reconstructed. The profile differences between the two point clouds are used to determine the damage parameters S, E_{2D}, $E_{3D,1}$ and $E_{3D,5}$. The non-dimensional damage parameter S, defined by Broderick and Ahrens (1982), uses the width-averaged profile of a structure. The eroded width-averaged area is divided by the d_{n50}^2 to express the S parameter.

$$S = \frac{A_e}{d_{n50}^2} \tag{6.1}$$

The damage parameters E_{2D} and $E_{3D,m}$ are respectively defined by Hofland et al. (2011) and Hofland et al. (2014). Both parameters determine the maximum erosion perpendicular to the slope. The damage parameter E_{2D} uses the same width-averaged profile as the S parameter but uses the maximum erosion within the profile. The $E_{3D,m}$ uses the maximum erosion measured over the whole structure. The erosion is averaged over a spatially moving area of diameter m*d_{n50}.

$$E_{2D} = \frac{\max(\langle e \rangle_w)}{d_{n50}} \tag{6.2}$$

$$E_{3D} = \frac{\max(\langle e \rangle_{md_{n50}})}{d_{n50}} \tag{6.3}$$

The determination of the damage parameters is presented in Figure 6.1a and b. All measurements start with obtaining the initial (undamaged) profile, followed by the execution of the test. Next, the damaged profile is measured. To obtain the S and E_{2D} parameters, shown in Figure 6.1a, both profiles are width-averaged and the width-averaged eroded profile is obtained. In the case of the $E_{3D,m}$ parameter, the initial and damaged profile measurements are used to determine the eroded volume. In this volume, the maximum erosion is measured for a circular moving area with diameter m*d_{n50} as shown in Figure 6.1b.

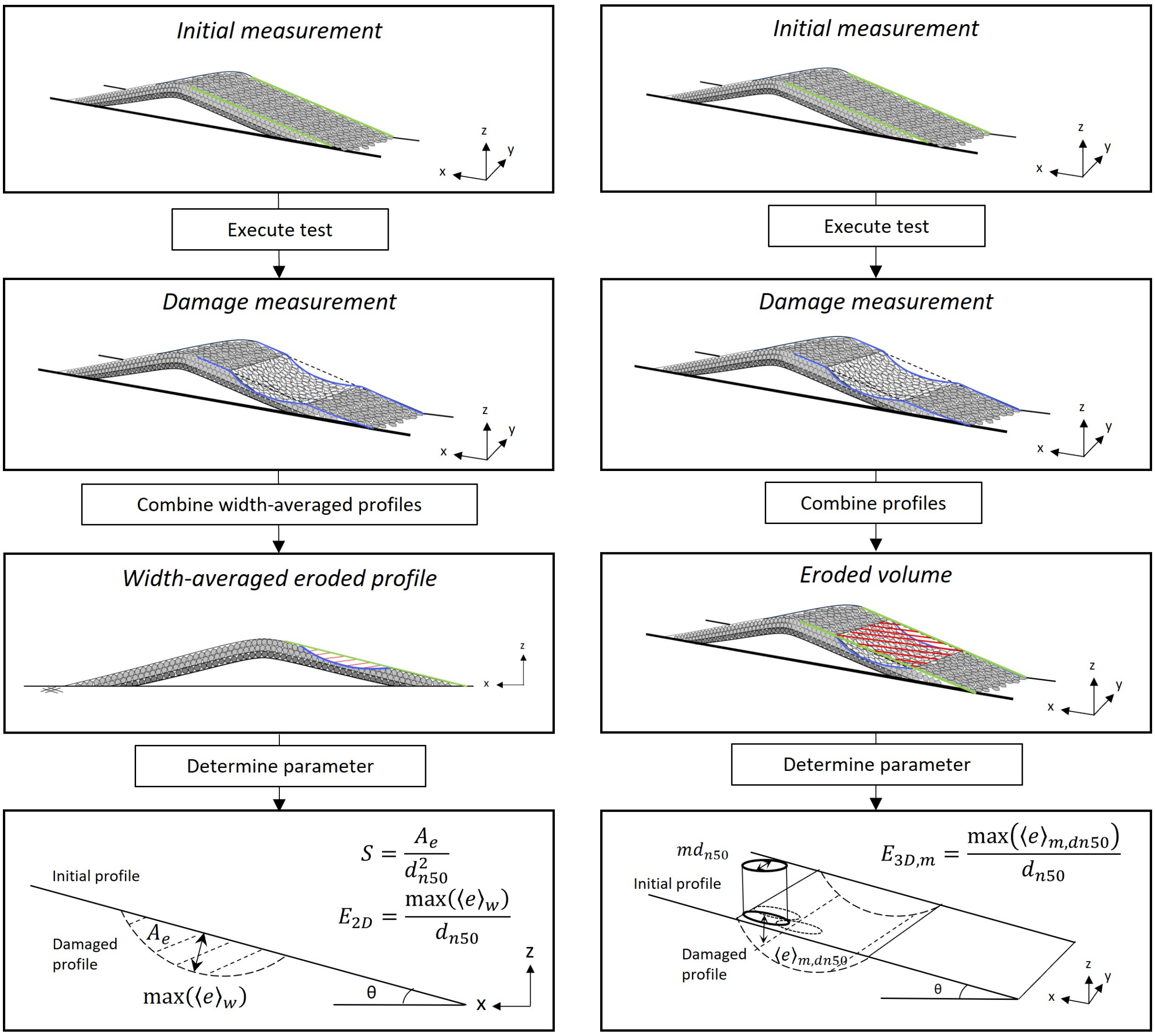

(a) Damage parameters S and E$_{2D}$

(b) Damage parameter E$_{3D,m}$

Figure 6.1: Acquisition of damage parameters S, E$_{2D}$ and E$_{3D}$.

The 3D point clouds are constructed from 21 2D images by using Agisoft Metashape Professional, resulting in point clouds containing approximately 10 million data points. This results in an average of 17 data points per millimetre^2. An accuracy of 0.15 pixels is achieved, which corresponds to 0.5 millimetres. Profile differences between models are measured by using the Multiscale Model to Model Cloud Comparison (M3C2) algorithm of the CloudCompare (Lague et al., 2013) software. The algorithm is used to determine the difference between point clouds by determining the normal directions of groups of points within a circular area with a diameter of 1/4 d$_{n50}$ = 4.8 millimetres. Next, the distance between each point group in the direction of the determined normal is calculated. This results in a new point cloud with one measured distance data point per 4.8x4.8 millimetre.

Figure 6.2 shows a point cloud result due to a single overflowing wave. The profile differences between the point cloud model of the initial and the damaged profile are presented in a 3D view, lee side top view, lee side side view and lee side spatially averaged top view. The side view shows the corresponding width-averaged damage curve (marked by the red crosses). The area between this curve and the horizontal line is the width-averaged eroded area used to determine the S parameter. The maximum depth of the eroded area is used to determine the E$_{2D}$ parameter. To determine the E$_{3D,m}$ parameters, the top view is averaged over a circular area of diameter md$_{n50}$.

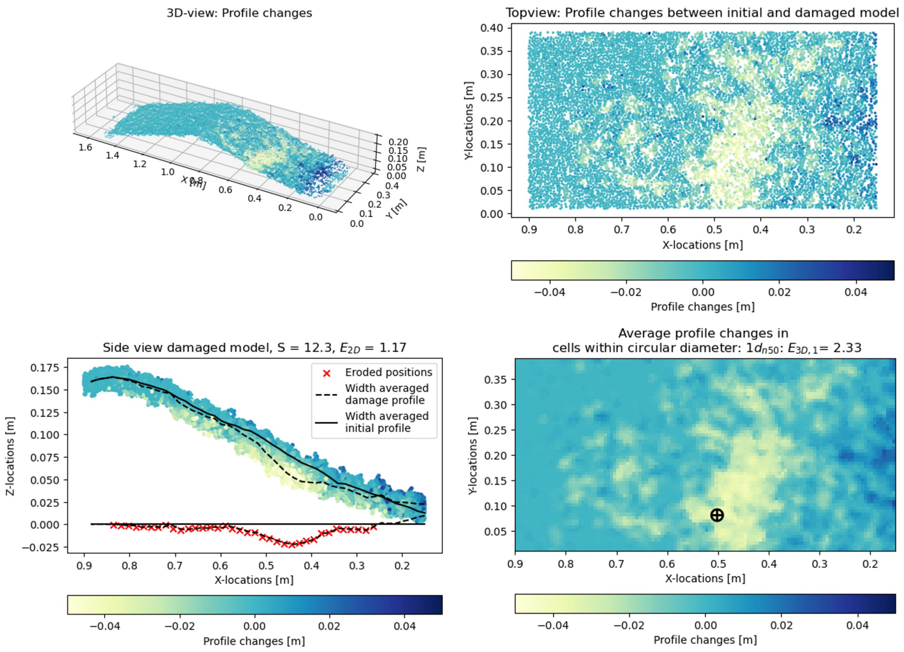

Figure 6.2: Profile changes and damage analysis for h_{target} = 5.4 cm and R_c = 10.9 cm. Left top: 3D view of profile changes in the model. Right top: Top view of changes on lee side. Left bottom: Width averaged side view with S and E_{2D}. Right bottom: Spatially averaged top view with $E_{3D,1}$.

6.2. Damage experiment results

Damage to the lee side of the structure is measured by using physical model 5. The primary ship waves were manually recreated by changing the discharge on the wave-facing side. As a result, the targeted wave height is in most cases within ± 1 cm of the measured wave height. Table 6.1 presents the measured damage expressed in S, E_{2D}, $E_{3D,1}$ and $E_{3D,5}$ for each combination of wave height and freeboard. The damage parameters were determined at the crest and lee side slope. According to de Almeida et al. (2019), a characterisation width of about 25 d_{n50} should be used. Therefore, the full width of the structure is used to determine the damage parameters, corresponding to a characterisation width of 21 d_{n50}. The time between the top of the single wave and the trough is presented by T_{ST}.

Table 6.1: Damage experiment test results model 5 for freeboard R_c 10.9 to 5.5 cm

h_{target} (cm)	R_c (cm)	$z_{max,meas}$ (cm)	T_{st} (sec)	S	E_{2D}	$E_{3D,1}$	$E_{3D,5}$
3.6	10.9	3.75	8.4	5.8	0.74	1.87	0.95
5.4	10.9	6.89	6.8	12.3	1.17	2.33	1.74
10.8	10.9	10.55	6.6	56.4	2.37	2.76	2.53
3.6	8.2	3.27	7.0	1.4	0.27	1.01	0.48
5.4	8.2	7.2	5.8	3.9	0.39	1.55	0.53
5.4	8.2	6.09	6.6	3.7	0.36	1.43	0.74
8.1	8.2	9.84	6.8	10.8	0.89	1.84	1.17
10.8	8.2	11.86	6.0	34.4	2.08	2.83	2.34
3.6	5.5	3.48	5.8	0.8	0.18	1.14	0.27
3.6	5.5	4.62	5.8	1.6	0.15	1.08	0.51
5.4	5.5	6.77	7.0	2.9	0.43	1.29	0.57
8.1	5.5	9.65	5.8	3.6	0.44	1.54	0.98
10.8	5.5	10.61	5.6	6.4	0.6	1.64	0.83
12.5	5.5	12.4	7.4	10.3	0.91	2.11	1.33

Table 6.2: Damage experiment test results Model 5 for freeboard R_c of 2.7 to 0 cm

h_{target} (cm)	R_c (cm)	$z_{max,meas}$ (cm)	T_{st} (sec)	S	E_{2D}	$E_{3D,1}$	$E_{3D,5}$
3.6	2.7	3.86	5.6	0.7	0.08	0.83	0.18
5.4	2.7	6.25	5.6	1.1	0.12	0.99	0.3
8.1	2.7	8.28	6.2	1.4	0.24	1.21	0.34
10.8	2.7	11.23	6.2	4.2	0.45	1.38	0.72
12.5	2.7	12.55	5.8	3.3	0.34	1.4	0.83
12.5	2.7	11.56	5.8	5	0.5	1.79	0.86
12.5	2.7	13.15	6.4	6.6	0.62	1.76	0.98
10.8	0	11.01	5.6	0.5	0.07	1.1	0.16
10.8	0	10.64	4.6	1.5	0.1	0.98	0.25
12.5	0	12.94	6.0	3.1	0.28	1.38	0.47

Each measured damage parameter is presented in Figure 6.3 for each measured wave height and corresponding freeboard. In all graphs, a regression curve per tested freeboard level is added. This represents the average expected damage level for an increasing wave height by a certain freeboard. It can be observed that these progression curves have a similar shape per freeboard, indicating that there is a correlation between the measured wave height, freeboard and damage level.

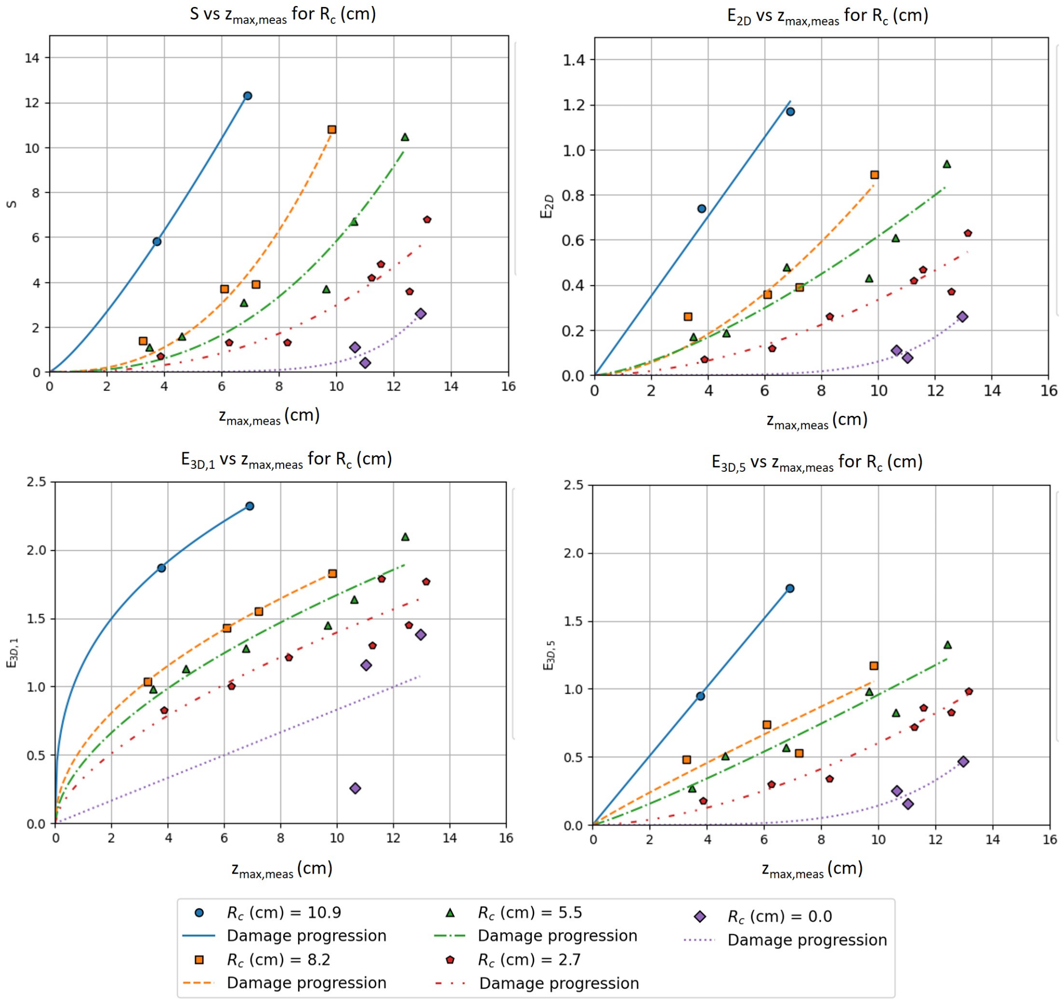

Figure 6.3: S, E_{2D}, $E_{3D,1}$ and $E_{3D,5}$ values for each measured $z_{m}ax$ and R_c

6.3. Damage limits for overflowing

Damage concepts of a rubble mound structure can be described by damage initiation, intermediate damage and failure. In the Literature review in Section 2.3, these are defined for structures attacked by wind waves by several researchers. Researchers Thompson and Shuttler (1975), van der Meer (1988), Melby and Kobayashi (1998) and de Almeida et al. (2019) state that a rubble mound structure has failed when the filter layer becomes exposed. One of the most recent studies into damage limits, carried out by de Almeida et al. (2019), defined the limits as follows:

- Damage initiation: defined as the condition in which a circular hole of $1d_{n50}$ diameter and a depth of $1d_{n50}$ is observed in the armour layer.
- Intermediate damage: defined as the condition in which a circular hole of $1d_{n50}$ diameter and a depth of $1.5d_{n50}$ is observed in the armour layer.
- Failure limit: defined as the condition where a circular hole of $1d_{n50}$ diameter and a depth of nd_{n50} is observed in the armour layer, with n equal the number of rock layers in the armour layer.

As these concepts apply to the damage to the rubble mound structures, they are also used to determine the damage limits for overflowing long-period primary ship waves over groynes. The $E_{3D,1}$ parameter is used as a calibration method to characterise the occurring damage to the groyne structure. This method has also been used by de Almeida et al. (2019) in the determination of the damage limits of rubble mound structures for wind waves. During the damage experiment, the tested physical model 5 has 2 d_{n50} layers in the armour layer, resulting in the damage limits of the damage parameter $E_{3D,1}$:

$E_{3D,1}$ damage limits:

- Damage initiation: $E_{3D,1}$ = 1
- Intermediate damage: $E_{3D,1}$ = 1.5
- Failure: $E_{3D,1}$ = 2.0

The damage limits of the parameters S, E_{2D} and $E_{3D,5}$ are calibrated based on the damage limits of $E_{3D,1}$. The relation between the parameters is shown in Figure 6.4. A bootstrapping confidence interval is used to determine the 90 % confidence interval for the regression curve and is indicated by the red band. The regression curves express a damage parameter in the power law equation $a * x^b$, in which a and b are parameters and x is another damage parameter. Bootstrapping was used to determine the a and b parameters, including the 90% confidence interval. A random-sized sample of the damage measurements was taken to determine a and b. By doing this 10000 times, distributions of parameters a and b were created. From these distributions were 1000 regression lines determined and the 95th percentile of the sorted regression lines was taken, resulting in the 90% confidence interval.

The bootstrapping interval is a way to estimate the confidence intervals without any assumption. However, in most past research into damage to rubble mound structures, the standard deviation (σ) and the mean value (μ) per damage concept for each damage parameter are determined. To compare the determined damage limits to other research, these are defined and presented in Table 6.3.

Table 6.3: Damage limits at lee side of rubble mound structure for overflowing long period waves

Damage concepts	**$E_{3D,1}$**	**S** ($\mu \pm 2\sigma$)	**E_{2D}** ($\mu \pm 2\sigma$)	**$E_{3D,5}$** ($\mu \pm 2\sigma$)
Damage initiation	1.0	1 ± 0.9	0.2 ± 0.1	0.3 ± 0.2
Intermediate damage	1.5	4 ± 0.9	0.4 ± 0.1	0.7 ± 0.2
Failure	2.0	9 ± 0.9	0.9 ± 0.1	1.2 ± 0.2

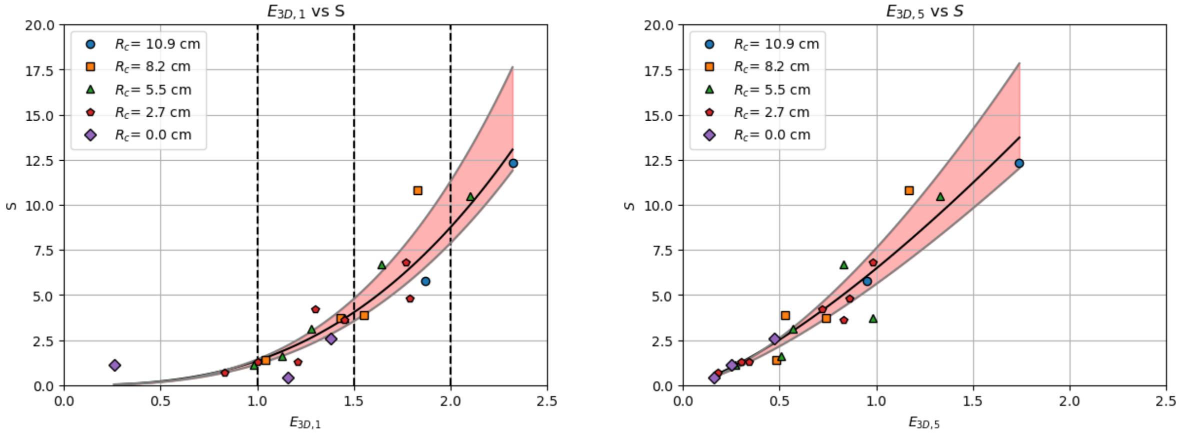

(a) E$_{3D,1}$ vs S

(b) E$_{3D,5}$ vs S

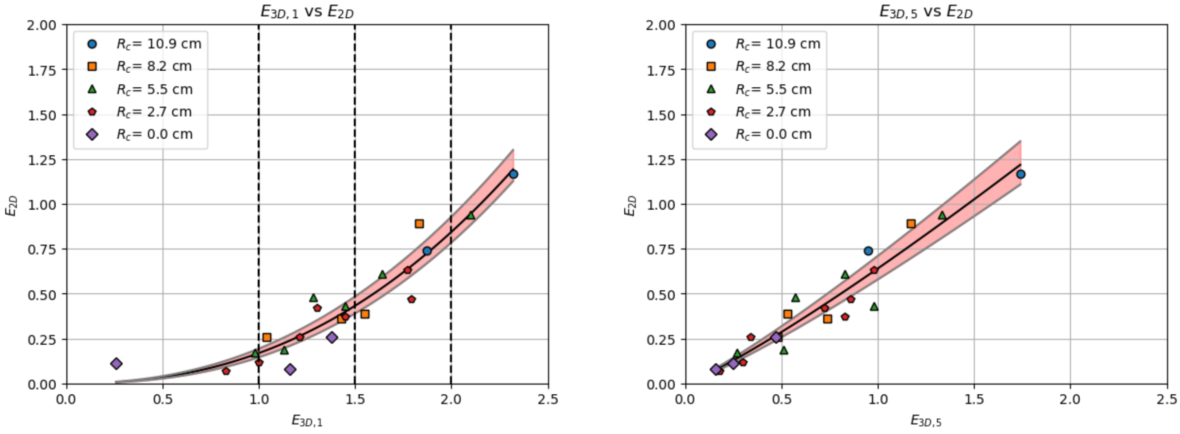

(c) E$_{3D,1}$ vs E$_{2D}$

(d) E$_{3D,5}$ vs E$_{2D}$

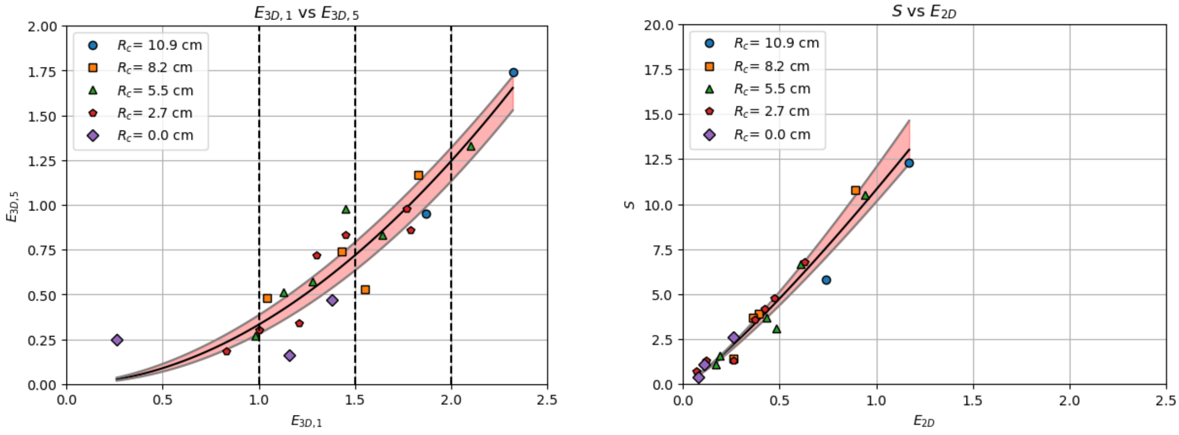

(e) E$_{3D,1}$ vs E$_{3D,5}$

(f) S vs E$_{2D}$

Figure 6.4: S, E$_{2D}$, E$_{3D,1}$ and E$_{3D,5}$ values related to each other with 90% bootstrap confidence interval.

The bootstrapped confidence interval shows the variation around the regression curve. The confidence bands around the regression curves are examined to determine the variability of each damage parameter. This is performed at the damage initiation, intermediate damage and failure limits per damage parameter. The values per damage parameter for the regression curve are shown in Table 6.4. Tables 6.5 and 6.6 show the values of the upper and lower 90% confidence intervals for the regression curve for each damage limit. Table 6.7 presents the relative variability around the regression curve by dividing the confidence bandwidth by the mean value of the regression curve per damage limit. It shows that the relative variability around the regression curve increases for the damage parameter S, but decreases for the parameters E$_{2D}$ and E$_{3D,5}$. This indicates that the E$_{2D}$ and E$_{3D,5}$ parameters can determine the damage more accurately for increasing damage levels. However, for smaller damage levels the S-parameter has a smaller variation. This suggests that the S-parameter indicates damage levels more accurately for smaller damage levels.

Table 6.4: Regression damage values per damage parameter for each damage limit (μ)

	Damage initiation	Intermediate damage	Failure
S	1.36	4.04	8.76
E$_{2D}$	0.169	0.433	0.846
E$_{3D,5}$	0.330	0.717	1.244

Table 6.5: Lower 90% confidence interval of the regression curve per damage parameter for each damage limit (Lower 90 % CI for μ)

	Damage initiation	Intermediate damage	Failure
S	1.15	3.58	8.01
E$_{2D}$	0.142	0.387	0.786
E$_{3D,5}$	0.290	0.643	1.12

Table 6.6: Upper 90% confidence interval of the regression curve per damage parameter for each damage limit (Upper 90 % CI for μ)

	Damage initiation	Intermediate damage	Failure
S	1.46	4.78	11.1
E$_{2D}$	0.197	0.486	0.923
E$_{3D,5}$	0.391	0.796	1.32

Table 6.7: Relative variation per damage parameter for each damage limit ((Upper - Lower 90% CI)/μ)

	Damage initiation	Intermediate damage	Failure
S	0.22	0.29	0.35
E$_{2D}$	0.33	0.23	0.16
E$_{3D,5}$	0.31	0.21	0.16

6.4. Critical wave-freeboard combination prototype

The critical limits of the prototype structure can be determined, now the damage parameters per wave and freeboard level are known in combination with the defined damage limits on the lee side of the groyne structure. Wave heights were tested within the measured range of z_{max}/P < 0.6. This range was extended to z_{max}/P < 0.8 during the damage experiment. The tests were conducted on a physical model based on the prototype which experienced a maximum wave height which corresponds to z_{max}/P = 0.5. Another design of groyne which has the same trunk dimensions as the prototype was designed next to the prototype, only the design of the root was different (Melling et al., 2020). This groyne showed severe erosion and had a measured maximum overflowing z_{max}/P = 0.6. The results of the wave height and freeboard combinations for the failure limits per damage characteristics are shown in Figure 6.5.

The tested freeboard levels were based on the drawdown at the wave-facing side of the prototype and ranged between 0 < R_c / P < 0.46. This range was increased during the experiment by testing an increased freeboard of R_c / P = 0.61. The freeboard levels are assumed to be similar for both prototype models. The corresponding damages due to the wave height per a freeboard level are presented in Section 6.2. Analysing the measured range of wave heights and freeboard levels, it can be observed that the physical model reaches the S - failure limit for relative wave heights z_{max}/P > 0.5 combined with relative freeboard levels 0.39 < R_c/P < 0.46. The E_{2D} failure limit is reached for z_{max}/P > 0.54 combined with relative freeboard levels 0.39 < R_c/P < 0.46. The $E_{3D,5}$ failure limit is reached for z_{max}/P > 0.52 in combination with relative freeboard levels 0.39 < R_c/P < 0.46. All observations are based on Figure 6.5, in which the measured ranges in wave heights and freeboard levels at the prototype are marked for the failure limits per damage parameter. Outside the measured ranges of wave height and freeboard, it is observed that the increased freeboard level results in failure for z_{max}/P = 0.25. For freeboard levels smaller than R_c/P = 0.39, it is observed that the critical wave height is larger than the maximum measured wave height of z_{max}/P = 0.6.

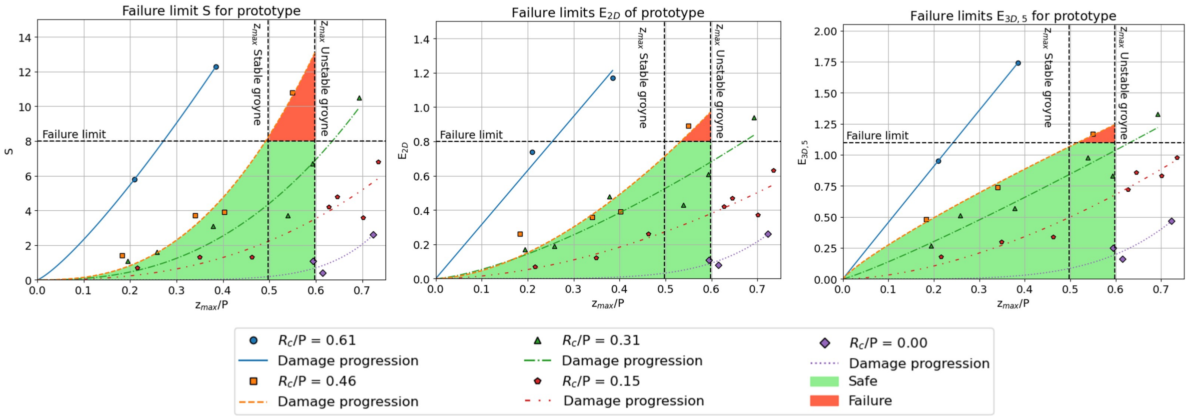

Figure 6.5: Failure limits per damage parameter due to overflowing long period waves. The measured range of freeboard and wave heights are marked in green when smaller than the failure limit and red when greater than the failure limit.

6.5. Discussion of sub-question 3 & 4

Sub-question 3: *'How could the damage due to groyne overflowing caused by long-period primary ship wave loadings be expressed in terms of damage parameters S, E_{2D} and E_{3D}?'* was addressed in this chapter in Section 6.1 and 6.2. Damage was measured by comparing 3D models of an undamaged and a damaged physical model. The damage to the structure was determined by testing single overflowing waves. The damage parameters based on the width-averaged profiles (S and E_{2D}) were measured for the maximum available characterisation width of 21 d_{n50}. The parameters based on the maximum eroded depth ($E_{3D,1}$ and $E_{3D,5}$) were measured over the whole lee side profile. Damage is mostly observed on the lee side slope, rarely on the crest and none on the wave-facing side.

Sub-question 4: *'How to characterize damage limits (initial damage, intermediate damage, and failure) for groynes exposed to long-period primary ship wave loadings in shallow and confined waterways?'* was answered in Section 6.3. The damage characterisation limits were described as follows:

- Damage initiation: defined as the condition in which a circular hole of 1 d_{n50} diameter and a depth of d_{n50} is observed in the armour layer.
- Intermediate damage: defined as the condition in which a circular hole of 1 d_{n50} diameter and a depth of 1.5 d_{n50} is observed in the armour layer.
- Failure limit: defined as the condition where a circular hole of 1 d_{n50} diameter and a depth of 2 d_{n50} is observed in the armour layer.

The damage limits of the lee side structure are determined for overflowing long-period waves using the $E_{3D,1}$ parameter as a calibration. This method was introduced by de Almeida et al. (2019) for the determination of damage limits for rubble mound structures attacked by wind waves. Table 6.8 shows the damage limits of the overflowing waves on the lee side of the structure. Table 6.8 gives the damage limits for wind waves on the wave-facing side. Both limits for wind waves and overflowing waves for the parameters E_{2D} and $E_{3D,5}$ are almost equivalent. The damage parameter S shows similar limits for damage initiation and intermediate damage but is smaller for the failure limits for overflowing waves. Nevertheless, a failure limit of S = 8 is in the range of the defined failure limit S = 8 - 17 by van der Meer (1988). Therefore, the critical wave can be defined for the groyne structure, by determining the critical combination of lee side freeboard and overflowing wave height. For the hydraulic conditions measured at the prototype, it is observed that the structure reaches the failure limits for conditions $z_{max}/P > 0.5$ in combination with freeboard levels of $0.39 < R_c/P < 0.46$.

The damage results were obtained for individual, manually created overflowing waves. Therefore, the damaged model had to be rebuilt after each individual wave. Although it was ensured that the armour layer was compressed, it cannot be ruled out that the rocks had settled completely. It is therefore likely that the measured damage is greater than it would have been if the rock had settled.

Table 6.8: Damage limits (μ) for overflowing waves at lee side of rubble mound structure and lower 90% failure band (μ-1.64σ)

Damage concepts	**$E_{3D,1}$**	**S**	**E_{2D}**	**$E_{3D,5}$**
Damage initiation	1.0	1	0.2	0.3
Intermediate damage	1.5	4	0.4	0.7
Failure	2.0	8 (90% conf.)	0.8 (90% conf.)	1.1 (90% conf.)

Table 6.9: Literature-based damage limits for wind waves at the wave-facing side of rubble mound structure (de Almeida et al., 2019)

Damage concepts	**$E_{3D,1}$**	**S**	**E_{2D}**	**$E_{3D,5}$**
Damage initiation	1.0	1	0.2	0.3
Intermediate damage	1.5	4	0.5	0.7
Failure	2.0	11 (90% conf.)	0.9 (90% conf.)	1.1 (90% conf.)

7

Flow and damage interpretation

This chapter expresses the link between the flow velocities measured in the flow experiments and the damage measured in the damage experiment. Section 7.1 starts with how these can be linked. Section 7.2 presents the location of the occurring damage, followed by the damage-flow relation in Section 7.3. This leads to the answer to sub-research question 5: 'How could the overflow velocity equation be linked to the damage profile at the crest and lee side for a groyne exposed to primary ship wave loadings?'. This answer is discussed in Section 7.4.

7.1. Flow and damage experiment link

The flow and damage experiments were conducted separately and differed in some respects. The flow experiment was conducted on physical models 1, 2, 3 & 4 to measure the flow velocities for continuous free-flow conditions with no preset lee side water level. During the damage experiment, physical model 5 was tested for damage occurrence by simulating long-period primary ship waves for different lee side water levels.

The waves at the prototype can be described by the quasi-steady approximation, see Chapter 1. The maximum flow velocity of an overflowing long-period wave is approximated by the flow velocities measured during the flow experiments. These maximum flow velocities are measured for water levels similar to the maximum wave height of the long-period waves tested in the damage experiment. As the flow accelerates along the slope, it is expected to reach a critical velocity at which it begins to move the rocks of the armour layer. This phenomenon has already been described by Izbash (1935) for free-flow conditions and is repeated in equation 7.1 from Chapter 2. However, the position of the critical velocity and hence the location of the onset of damage is still undefined by Izbash. It is therefore important to know the location of the damage.

$$\frac{u_c}{\sqrt{\Delta g d_{n50}}} = 1.84 \tag{7.1}$$

7.2. Location of damage

The damage profiles for all the tested wave heights per freeboard level are presented in Figure 7.1, including a 90% confidence interval for the mean damage profile. The mean damage was measured for the characterisation width of 21 d_{n50}. The corresponding upper and lower confidence intervals are obtained by dividing the width of the model into 21 equal sections of 19 mm, which is the same size as the 1 d_{n50}. The Student t-distribution is applied to the 21 corresponding profiles, resulting in the confidence band. It can be observed that the damage confidence band ranges within $\pm$ 0.1 e_w / d_{n50} around the mean damage curve.

The damage profiles present the lee side erosion for each freeboard. All profiles show a slow accumulation of erosion at the beginning, followed by a sudden increase in damage where the maximum erosion is located. The two largest tested freeboard levels (R_c = 10.9 cm and R_c = 8.2 cm) show that

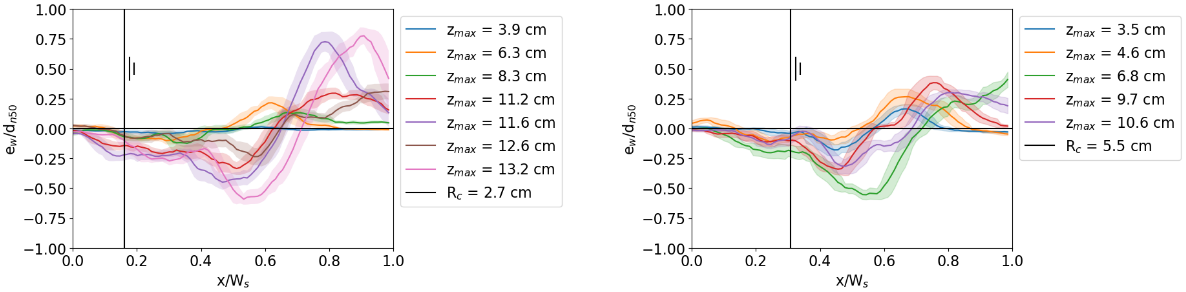

(a) R_c = 2.7 cm

(b) R_c = 5.5 cm

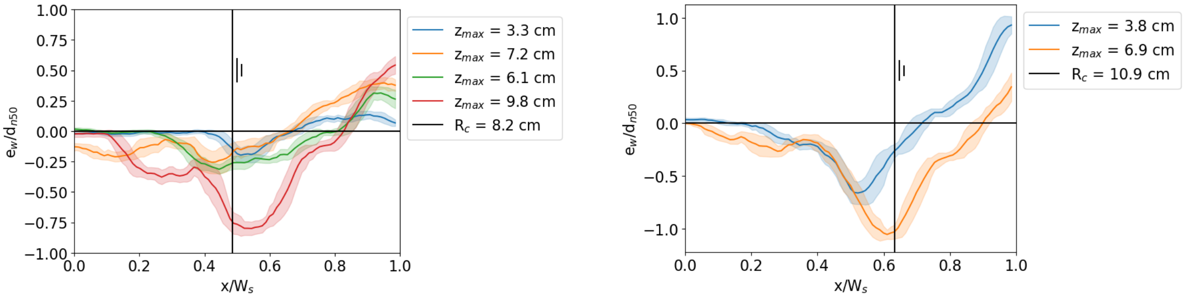

(c) R_c = 8.2 cm

(d) R_c = 10.9 cm

Figure 7.1: Damage profiles for different freeboard water levels and tested wave heights. All profiles are presented with a 95% confidence interval.

the maximum eroded positions are approximately equal to the freeboard levels. However, the smaller tested freeboard levels (R_c = 5.5 cm and R_c = 2.7 cm) show that the position of maximum erosion is going down along the leeward slope for increasing wave heights. For smaller waves (z_{max} < 10 cm), the damage is still around the freeboard water level. Figure 7.2 shows the positions of the maximum erosion per wave for each freeboard level. Here, the wave and freeboard values are made dimensionless. For the tested waves which are within the measured conditions at the prototype, it can be seen that the maximum damage is moving downward for large wave heights and small freeboard levels. However, for waves larger than the measured range, z_{max}/P > 0.6, it becomes apparent that the maximum damage is occurring at 0.5 X/W_s for all freeboard levels.

One explanation for the shifting location of the maximum damage at the smaller freeboard levels is the position of the occurring bore at the interaction of the overflowing and lee side water levels. When the freeboard is small and the wave height is large, the overflowing water 'pushes' the lee side water away from the slope. Eventually, the bore will develop at positions lower than the freeboard position, resulting in high flow velocities just in front and high turbulence at the bore. This increase in turbulence explains the sudden increase in erosion for the damage profiles.

7.3. Flow and damage equation

The flow velocity equation designed in Chapter 5, was constructed during free-flow conditions. Because the overflowing primary ship-induced waves can be described by the quasi-steady approximation, as stated in Chapter 1, the flow is considered to be in free flow until the overflowing flow interacts with the lee side water level. The maximum flow velocities occur at the interaction of the lee side water level. Therefore, the dimensionless flow velocity equation (Equation 5.3) is rewritten to describe these flow velocities:

$$U(h = z_{max}, R_c, \Theta, d_{n50}) = \sqrt{g z_{max}} * (1.95 - 0.88 * exp(-0.51 * \Theta R_c / d_{n50})) \tag{7.2}$$

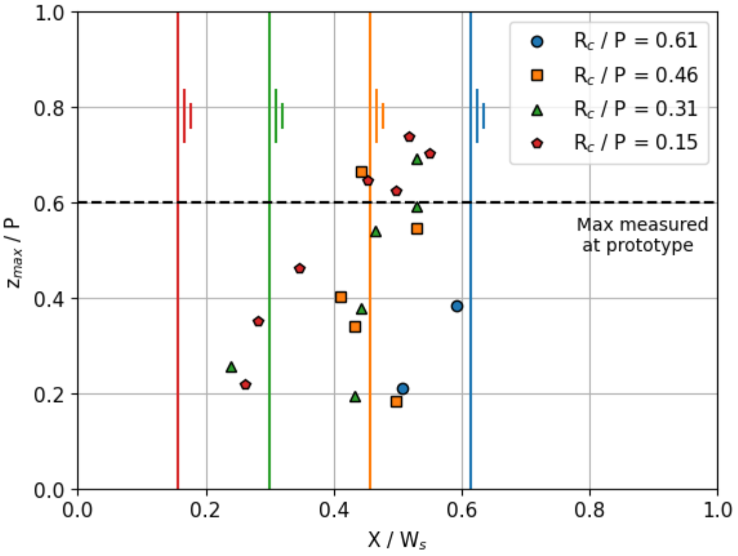

Figure 7.2: Position of maximum damage along lee side slope measured from crest for dimensionless wave height and freeboard

The equation describes the lee side flow velocities for a maximum water level above the structure crest height and the assumed freeboard. Damages are observed to occur around the lee side water level. For smaller waves (z_{max} < 10 cm) combined with small freeboard levels (R_c = 2.7 and 5.5 cm), the erosion starts and reaches its maximum around the lee side water level. For larger waves (z_{max} > 10 cm) combined with the same small freeboard levels, the damage also starts around the lee side water level. However, the maximum erosion is positioned further down the slope. All waves for larger freeboard levels (R_c = 8.2 and 10.9 cm) show the start and maximum damage around the lee side water level. So in all cases, the maximum or the start of damage is around the lee side water level.

Therefore, relations between the damage parameters S, E_{2D} and $E_{3D,5}$ and corresponding flow velocities (Equation 7.2) are created in dimensionless form. The flow velocities are determined at the freeboard level. The relations are presented in Equations 7.3, 7.4 and 7.5. Figure 7.3 depicts the corresponding regression curves with a bootstrapped 95% confidence interval and includes the defined failure limits. The relations express the level of damage by taking the slope factor (K_s), angle of repose (ϕ = 40 deg), slope (α (deg), θ [-]), rock size (d_{n50}) and relative density (Δ) of the groyne into account for flow velocities determined by the dimensionless flow equation based on the measurements during the flow experiment.

$$S = 1.1 * 10^{-2} * \left(\frac{U(z_{max}, R_c, \Theta, d_{n50})}{\sqrt{\Delta g d_{n50} K_s}} \right)^{6.1} \tag{7.3}$$

$$E_{2D} = 6.7 * 10^{-3} * \left(\frac{U(z_{max}, R_c, \Theta, d_{n50})}{\sqrt{\Delta g d_{n50} K_s}} \right)^{4.3} \tag{7.4}$$

$$E_{3D,5} = 3.4 * 10^{-2} * \left(\frac{U(z_{max}, R_c, \Theta, d_{n50})}{\sqrt{\Delta g d_{n50} K_s}} \right)^{3.2} \tag{7.5}$$

$$K_s = \frac{sin(\phi - \alpha)}{sin(\phi)} \tag{7.6}$$

Based on the presented relations and damages, it can be observed that the damage initiation starts when overflow velocities of 1.0 m/s are reached at the physical model. At the prototype, the damage initiation occurs when flow velocities of 3.7 m/s are reached at the position where the overflow interacts with the lee side water level.

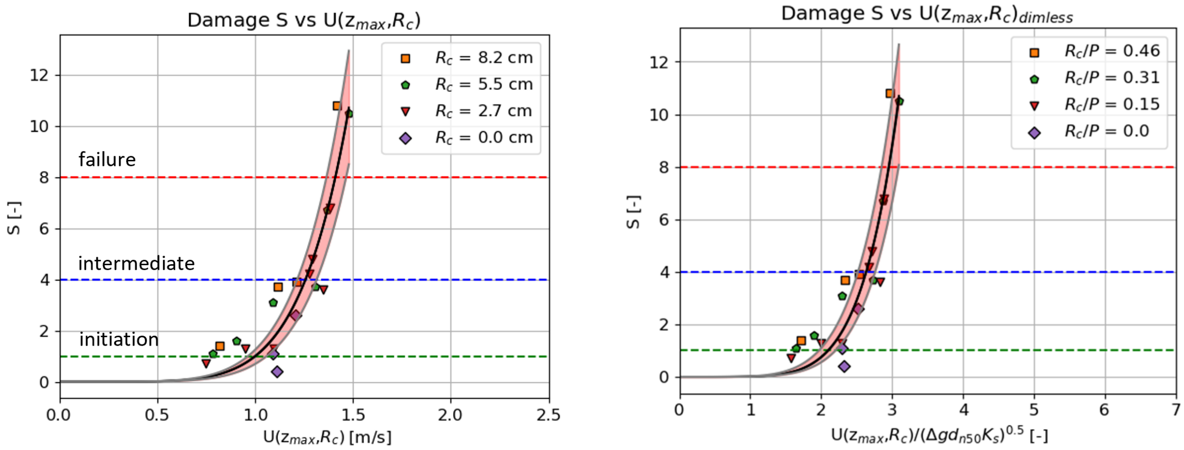

(a) S vs U(z_{max},R_c,θ,d_{n50})

(b) S vs U(z_{max},R_c,θ,d_{n50})$_{dimless}$, Equation 7.3

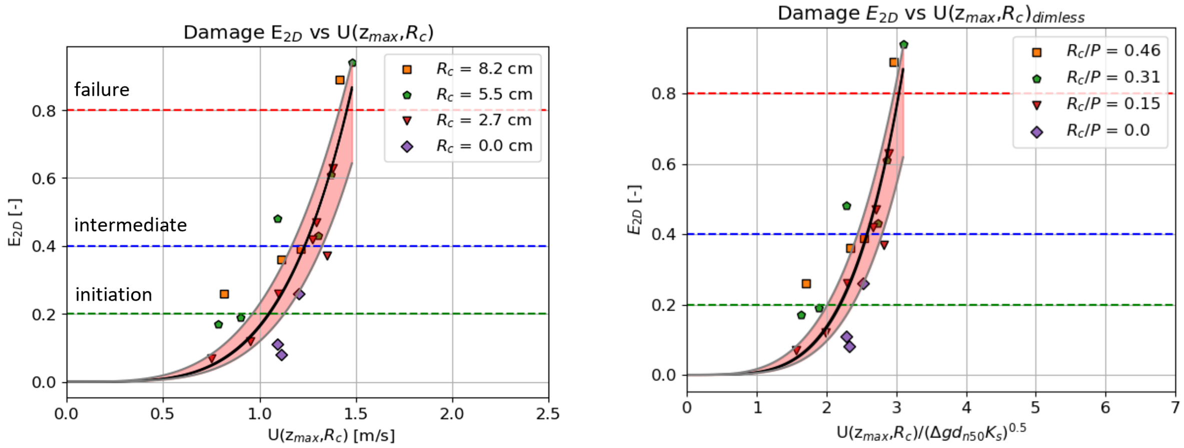

(c) E_{2D} vs U(z_{max},R_c,θ,d_{n50})

(d) E_{2D} vs U(z_{max},R_c,θ,d_{n50})$_{dimless}$, Equation 7.4

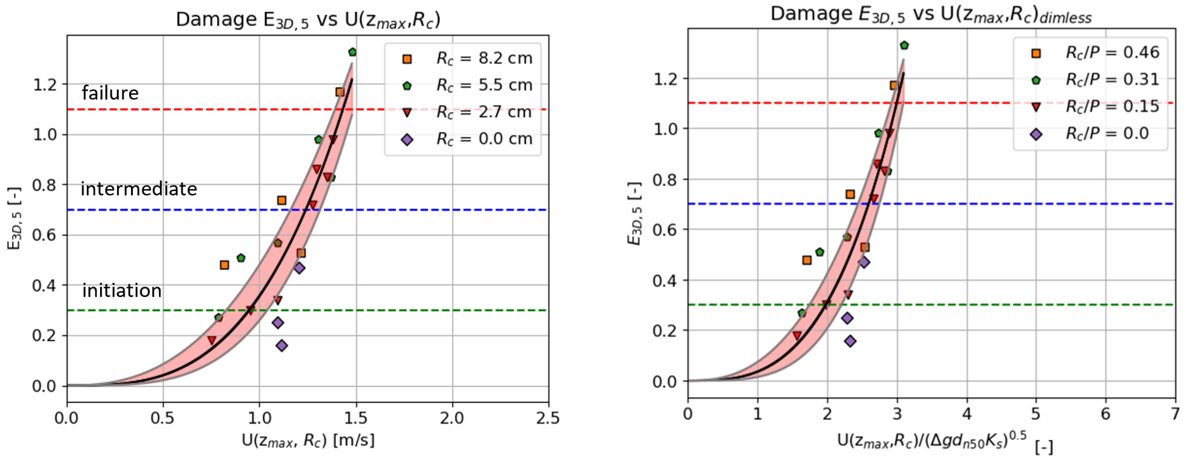

(e) $E_{3D,5}$ vs U(z_{max},R_c,θ,d_{n50})

(f) $E_{3D,5}$ vs U(z_{max},R_c,θ,d_{n50})$_{dimless}$, Equation 7.5

Figure 7.3: S, E_{2D} and $E_{3D,5}$ for measured velocities at the lee side water level position with corresponding damage limits damage initiation, intermediate damage and failure.

The dimensionless damage-flow equations are all expressed in the same form. Namely, the damage parameters S, E_{2D} and $E_{3D,5}$ are expressed by $a * (U(z_{max}, R_c, \theta, d_{n50})/\sqrt{\Delta g d_{n50} K_s})^b$. Parameters a and b are determined by a regression analysis based on the least square method. Both parameters are presented in Table 7.1 with the corresponding standard deviation (σ), coefficient of variation (CV) and the overall R^2 of the regression curve through the data.

Table 7.1: Parameters a and b for damage parameters S, E_{2D} and $E_{3D,5}$

Parameter	mean (μ)		st. dev. (σ)		CV (σ/μ)		R^2
	a	b	a	b	a	b	
S	0.011	6.1	0.0094	0.83	0.88	0.14	0.84
E$_{2D}$	0.0067	4.3	0.0048	0.70	0.72	0.16	0.77
E$_{3D,5}$	0.034	3.2	0.018	0.51	0.51	0.16	0.75

As can be observed in Table 7.1, the R^2 value for damage parameter S is the highest. It indicates that the S parameter is performing slightly better in expressing the damage for overflowing waves with the corresponding flow velocity. However, some important remarks must be made which are discussed in the next section.

7.4. Discussion sub-question 5

This section reviews the answer for research sub-question 5: *'How could the overflow velocity equation be linked to the damage profile at the crest and lee side for a groyne exposed to primary ship wave loadings?'.*

The damages measured during the damage experiment occur at the lee side of the structure and rarely at the crest. It is observed that the maximum erosion is located around the location of the lee side water level. Only in cases with smaller freeboard levels (R$_c$/P = 0.15 and 0.31) and waves larger z_{max}/P > 0.55, the maximum erosion occurs significantly lower at the slope than at the position of the freeboard. An explanation of this lower position is the position of the hydraulic jump occurring at the interaction between the overflowing and lee side water level. For larger wave heights and small freeboard levels, the hydraulic jump is pushed down along the slope, resulting in lower-positioned maximum erosion.

As the flow velocities are measured under free-flow conditions, the occurring turbulence due to hydraulic jump isn't taken into account. Therefore, the flow velocities can be used until the overflow interacts with the lee side water level. After this position, the flow starts to be highly turbulent and the flow velocities measured during the flow experiment do not represent the correct condition anymore. However, it is expected that the amount of turbulence is related to the overflowing flow velocities and therefore indirectly represented by the damage-flow equations.

Consequently, the flow and damage experiments are linked by taking the velocities measured during the flow experiment at the position of the freeboard water level and the corresponding damage due to an overflowing wave. This results in a damage-flow equation in which the damage initiation starts around 1.0 m/s at the physical model. The corresponding flow velocities at the prototype need to be around 3.7 m/s to reach the damage initiation.

The equation for the damage expressed in the dimensionless form (Equation 7.3, Equation 7.4 and Equation 7.5) can be rewritten into the Izbash Equation for d$_{n50}$. The Izbash constant K was determined by Izbash based on free-flow conditions over rockfill dams and presented the critical flow velocity when rock starts to move. The constant can be determined for the prototype structure by using the characteristics of the groyne and the flow velocity when the damage initiation starts. These equations are presented in Equation 7.7 and 7.8 for the damage parameter S with a corresponding damage initiation of S = 1.

The Izbash constant (K) for the tested physical model of the groyne for damage initiation is equal to 1.72. The constant is 6 % smaller than the constant derived by Izbash (K = 1.84). Nevertheless, the constant contains two components, namely the effect of turbulence and friction. These effects differ per structure and therefore a difference in the Izbash equation can be clarified. The found constant is smaller, which could indicate that the structure is slightly less stable than the constant defined by Izbash. This could be explained as there is an initial lee side water level. A bore occurs at the point where the overflowing wave interacts with the lee side water level interacts. This bore is an increase in turbulence and could result in extra damage. During the Izbash experiments, there was only a constant free flow and therefore no bore was present. This could be the explanation for why the Izbash equation is slightly smaller.

$$\frac{U(z_{max}, R_c, \theta, d_{n50})}{\sqrt{\Delta g d_{n50}}} = K \tag{7.7}$$

$$K = \sqrt[6.1]{S/0.011} * \sqrt{K_s} = 1.72 \tag{7.8}$$

The damage due to overflowing expressed in the flow velocities is the best performing by using the S parameter (Equation 7.3, R^2 = 0.84). However, a few side notes must be made. The S parameter expresses the width averaged erosion and therefore some erosion could be hidden. Furthermore, the failure limits of the S parameter at the lee-side for overflowing are different compared to the failure limits for wind waves at the wave-facing side. This could result in confusion as the same parameter could be used for both loading mechanisms. Therefore, one could suggest using damage parameter $E_{3D,5}$ instead of the damage parameter S. Although the $E_{3D,5}$ parameter performs slightly worse (R^2 = 0.77) than the S parameter, it measures the actual erosion and has the same damage limits as for wind wave loads. Besides, the relative variation at the damage limits is smaller for $E_{3D,5}$ compared to S, as presented in Chapter 6. Therefore, it is advised to use the $E_{3D,5}$. This would result in a more general way to express damages to rubble mound structures for different kinds of loading mechanisms and the damage limits are more accurately defined.

8

Conclusions and recommendations

8.1. Conclusion

The aim of this experimental study was to express the damage to a groyne structure overflown by a primary ship-induced wave into an equation, which can used as a design tool for groynes exposed to these types of waves. When a ship moves through water, the resistance due to the ship's cross-section causes disruptions in the water level consisting of primary and secondary waves. The primary wave includes a bow wave at the front of the ship, a stern wave at the end of the ship and a drawdown in between. These waves are the result of the ship pushing the water in front when it moves forward. The pushed water flows under and along the ship's hull and increases the flow velocity. The increase in velocity is even larger in water ways which are limited in its cross-section, with a drop in water level named the drawdown and is followed by the stern wave. When a ship wave passes a groyne in a limited confined waterway, the stern wave can overflow the groyne. During this overflow, high flow velocities occur at the lee side of the structure and can create damage on the lee side. To express the damage of the groynes during this overflow, two experiments were conducted to determine the flow velocities and the damages. These are connected to each other to describe the structure response during overflowing waves.

An LED PIV setup was used during the first experiment to measure the crest and lee side flow velocities of four physical models representing a groyne. One of these is the physical model based on the prototype. The PIV setup includes an LED light, tracer particles and a high speed camera. The tracer particles were injected at the toe of the physical models at the wave-facing side throughout the water depth. The LED light was positioned above the models and illuminates the centre of the structure from the crest to 70% of the lee side slope. The tracer particles reflected the light from the LED into the high speed camera. The displacement of the particles can be measured between two frames taken by the camera. Since the time interval between the two frames is known, a complete flow velocity field of the overflow was determined. Four different overflowing water levels in free-flow conditions were measured three times, resulting in flow velocities accelerating from 0.7 to 2.2 m/s.

All PIV measurements were taken for free flow conditions with no preset lee side water level. The corresponding flow velocities were determined by taking the depth and time-averaged flow velocities at four positions along the lee side slope for all hydraulic conditions tested. This resulted in a flow velocity equation for the lee side overflow of a groyne structure. The equation can be used for free flow conditions and for waves that can be described by the quasi-steady approximation in combination with supercritical flow conditions. This resulted in a dimensionless flow velocity equation. The equation describes the flow velocities for a maximum water level (h) above the crest measured in front of the structure and the position at the assumed lee side water level expressed by the freeboard R_c. The equation is based on flow velocities for slopes Θ = 1:3 and 1:4 with model rock diameters d_{n50} = 0.013 and 0.019m and can be used for $R_c > 0$.

$$U_{avg}/\sqrt{(gh)} = 1.95 - 0.88exp(-0.51\Theta R_c/d_{n50}) \tag{8.1}$$

The flow velocities are linked to the damage caused by overflow. These damages due to overflowing with a preset lee side water level were determined by measuring the erosion and quantifying it in damage parameters S, E$_{2D}$ and E$_{3D,5}$. Measurements were taken for a single overflowing wave, after which the physical model was rebuilt. A characterisation width of 21 d$_{n50}$ was used to determine the damage parameters. An increase in damage was observed for increasing wave heights. Furthermore, increasing the lee side freeboard led to a more significant increase in damage.

The corresponding damage limits for overflowing long-period waves at the lee side of a groyne structure with a 2 d$_{n50}$ thick rock layer, are presented in Table 8.1. The damage limits were described as initial, intermediate and failure. These were defined as respectively a 1 d$_{n50}$ wide hole of 1 d$_{n50}$, 1.5 d$_{n50}$ and nd$_{n50}$ deep. Here, n is the number of rock layers in the armour layer.

Table 8.1: Damage limits at lee side of rubble mound structure for overflowing long period waves

Damage concepts	**E$_{3D,1}$**	**S** ($\mu \pm 2\sigma$)	**E$_{2D}$** ($\mu \pm 2\sigma$)	**E$_{3D,5}$** ($\mu \pm 2\sigma$)
Damage initiation	1.0	1 ± 0.9	0.2 ± 0.1	0.3 ± 0.2
Intermediate damage	1.5	4 ± 0.9	0.4 ± 0.1	0.7 ± 0.2
Failure	2.0	9 ± 0.9	0.9 ± 0.1	1.2 ± 0.2

The flow velocity equation describes the flow along the lee side structure for continuous supercritical free-flow conditions. As the overflowing ship's primary waves are quasi-steady, the measured flow velocities for continuous free flow represent the maximum flow velocities of an overflowing wave. Therefore, the damage can be expressed in terms of the measured overflow velocities. Most damages occur around the lee side freeboard level. Only at a small freeboard, in combination with wave heights larger than measured on the prototype, is the maximum erosion significantly lower positioned than the freeboard water level. Damage parameters S, E$_{2D}$ and E$_{3D,5}$ express the damage based on the dimensionless flow velocity equation rewritten in dimensional form. It is recommended that the E$_{3D,5}$ parameter is used as this parameter is based on the actual erosion and the damage limits are the same as other loading mechanisms.

$$E_{3D,5} = 3.4 * 10^{-2} * \left(\frac{U(h = z_{max}, R_c, \Theta, d_{n50})}{\sqrt{\Delta g d_{n50} K_s}} \right)^{3.2} \tag{8.2}$$

This damage equation for damages expressed in flow velocities during overflowing primary ship waves is the answer to the formulated main research question of this research:

How can the overflowing flow velocity at the lee side of a groyne structure and the corresponding damage caused by primary ship waves be determined?

The damage equation can be used as a design tool for the construction of groynes exposed to overflowing waves which the quasi-steady approximation can describe. The flow velocities expressed by the dimensionless flow equation are based on supercritical conditions and are therefore the maximum occurring flow velocities. Supercritical conditions occur when the lee side freeboard levels are significant. Based on the prototype, these supercritical conditions are relatively rare, which indicates that this damage equation is a conservative but safe approach when used as a design equation. In case it is known that the overflowing at a structure is in supercritical condition or when the effects of supercritical conditions are studied, the damage equation can also be used in a probabilistic manner. In these cases, the flow velocities combined with damages are based on the experimental test conditions.

8.2. Recommendations

The following recommendations are defined for future research into the effects of overflowing primary ship-induced waves on groyne structures. These recommendations include improvements to the experimental setup and hydraulic elements that could affect the overflowing and damage to the structure.

Recommendations flow experiments

- The flow velocities during the flow experiments were measured without an initial lee side water level. This resulted in supercritical free flow conditions and therefore the upper limit of the flow velocities that can occur on the prototype. Although this is a safe approach, when used for a design tool, the prototype overflow velocities are also in sub-critical conditions due to the lee side water level. Therefore, the overflow velocities should be measured for conditions with a lee side water level. However, these measurements should be performed with a different PIV setup. The water surface becomes irregular and a flat surface is needed to measure the flow velocities. These irregularities and why these cause the invalid measurements are explained in Appendix H. By placing the LED close to the flume wall, it is expected that velocities could be measured with an initial water level. However, the flume walls could cause some unwanted friction resulting in slightly smaller flow velocities.

- With a scaling ratio of Lr = 13 and using the PIV setup, overflow water levels smaller than 5.4 cm could not be measured due to the same irregularities as during the initial lee side water level, see Appendix H for further explanation. To measure these scaled water levels larger physical models could be used. For the same-sized models, placing the LED close to the flume wall would result in measurable small water levels.

- During the flow experiments were the tracer particles injected at the toe of the structure. The flume led the flow, including the particles, to the central laboratory basin. This basin is used by other experimental flumes. As the tracer particles have a density which is close to the density of water, they could contaminate other experimental flumes because the particles settle slowly. Therefore, in this experiment, it was tried to minimize the amount of particles by placing the injection system close to the structure. This led to a smaller spreading over the width of the flume and therefore a smaller amount of particles was needed. However, as a result, the particles were sometimes grouped together which resulted in a small drop in measured flow velocities. See Appendix H for more details. By closing off the flume from the central basin and creating a closed pump system, a better mixture of particles could be added to the closed pump system. This would result in an evenly spread number of particles throughout the entire water column. Consequently, the grouped particles are probably reduced leading to more accurate measurements.

Recommendations damage experiment

- Regarding the position of the hydraulic jump that occurs at the interaction of the lee side water level and the corresponding overflow, the intensities and the exact position of the hydraulic jump for overflowing waves should be further investigated. The position of the hydraulic jump is likely to be correlated with the lee side freeboard and the height of the overflowing wave. Although the turbulence is captured indirectly by considering the full damaged profile, the damage equation could be extended to express the corresponding turbulence.

- The damages were caused by single overflowing waves. The model was rebuilt after each wave. Consequently, the rocks were not fully settled and the measured damage could be slightly larger than fully settled stones. For future research, a cumulative damage test should be performed to overcome this effect.

- The damage was caused by overflowing and the structure had an impermeable core. The effects of overflowing long-period waves cause large pressure changes in the core of the structure. Further research is needed to determine the impact of these pressure changes to determine their effect on the damage.

- During the damage experiments, the waves and lee side water levels were created and controlled manually. Therefore, the position of the physical model should be considered carefully during these types of tests. Efforts were made to maintain a constant lee side water level, and an unwanted increase in water level was counteracted by manually opening the weir gate at the end of the flume. It was observed that there were reflection waves at the lee side and wave-facing side. These reflection waves create unwanted events and could even increase the damage. Therefore it is important to improve the setup to encounter this reflection. One way could be by moving the physical model closer to the end of the flume. It is expected that the reflection will be reduced as it will be easier to maintain the lee side water level at a constant level. However, reducing the distance between the end of the flume and the physical model results in an increase in the distance between the inlet and the physical model. This increase results in an increase in the difficulty of accurately obtaining the desired wave height as the wave height seemed to be slightly smaller at the toe of the model compared to the visually confirmed wave height at the flume entrance. Therefore, the position of the physical model should be tested prior to experimentation to determine which position gives the most consistent results. In this research, the model was placed in the centre of the flume. For future research, the model may be better placed at 75% of the flume length or to shorten the flume. Shortening the flume could be done by constructing a temporary end weir gate and placing it closer to the physical model. Ideally, a downstream water level should be controlled automatically in which the added water volume of the created wave at the entrance water is extracted via a pumping system and wave absorbers are placed at the end of the flume to counter the reflection.

- Structure from Motion principles were used to measure the damages. This is an effective, cheap and precise method to capture the changes to a rubble mound structure. The main focus should be on the placement of the GCPs. It was observed that the GCPs placed close to the structure (at the toe of the structure so GCPs are wet) were more accurate compared to the GCPs placed above the structure (at the top of the flume so GCPs stay dry). The GCPs are printed on aluminium, therefore it is no problem that the markers become wet as long as they are dried before a measurement. To increase the accuracy, extra GCPs could be placed close to the structure at the walls of the flume. However, the walls should be covered by a non-reflecting material to ensure that the SfM software positions the GCPs correctly.

Bibliography

Abt, S., & Johnson, T. (1991). Riprap design for overtopping flow. *Journal of Hydraulic Engineering*, *117(8)*. https://doi.org/10.1061/(ASCE)0733-9429(1991)117:8(959)

Abt, S., Ruff, J., Wittler, R., & LaGrone, D. (1987). Gradation and layer thickness effects on riprap. *Proceedings of the National Conference on Hydraulic Engineering ASCE*.

Abt, S., Thornton, C., Scholl, B., & Bender, T. (2013). Evaluation of overtopping riprap design relationships. *Journal of the American Water Resources Association*, *49(4)*. https://doi.org/10.1111/jawr.12074

Adrian, R., & Westerweel, J. (2011). *Particle image velocimetry*. Cambridge University Press.

Ahmad, H., Hasan, M., & Tanaka, N. (2010). Analysis of flow around impermeable groynes on one side of symmetrical compound channel: An experimental study. *Water Science and Engineering*, *3(1)*, 56–66. https://doi.org/10.3882/j.issn.1674-2370.2010.01.006

Allsop, N., & Jones, R. (1994). *Stability of rock armoured beach control structures*. HE Wallingford.

Allsop, W., Wolters, G., van Gent, M., & Mühlestein, D. (2007). *Guidelines for physical model testing of breakwaters: Rubble mound breakwaters*. Hydralab.

Azimi, A., Rajaratnam, N., & Zhu, D. (2013). Discharge characteristics of weirs of finite crest length with upstream and downstream ramps. *Journal of irrigation and drainage engineering*, *139(1)*. https://doi.org/10.1061/(ASCE)IR.1943-4774.0000519

Bakker, W., Verhaart, F., de Fockert, A., & Oldenziel, G. (2019). Pulsed light emitting diodes for particle image velocimetry in a vertically submersible pump. *38th IAHR World Congress*. https://doi.org/10.3850/38WC092019-0129

BAW. (2010). Bemessung der strombauwerke in der außenweser unter berücksichtigung von schiffswellenbelastungen (baw-gutachten, a39550210120). *Bundesanstalt für Wasserbau*.

BAW. (2019). Pilotporjekt zur stablität von optimierten strombauwerken im untersuchungsabschnitt juelssand: Hopperbagger in fahrt [image]. https://www.flickr.com/photos/bundesanstalt_fuer_wasserbau/46711301684/in/photostream/

Bertram, V. (2011). *Practical ship hydrodynamics*. Elsevier.

Bhowmik, N. G., Demissie, M., & Osakada, S. (1981). Waves and drawdown generated by river traffic on the illinois and mississippi rivers. *ISWS Contract Report CR 271*.

Biabani, R., Salmasi, F., Nouri, M., & Abraham, J. (2021). Flow over embankment gabion weirs in free flow conditions. *Journal of Hydro-environment Research*, *44*, 65–76. https://doi.org/10.1016/j.jher.2022.08.001

Broderick, L. L., & Ahrens, J. P. (1982). Riprap stability scale effects.

Burcharth, H. (2006). Structural stability of detached low crested breakwaters. *Coastal Engineering*, *53(4)*, 381–394. https://doi.org/10.1016/j.coastaleng.2005.10.023

Chanson, H. (2004). *Hydraulics of open channel flow*. Butterworth-Heinemann. https://doi.org/10.1016/B978-0-7506-5978-9.X5000-4

Cheng, X., & Gulliver, J. (2011). Velocity profile for developing flow over stepped spillway. *AIP Conf. Proc.*, *1376(1)*, 343–350. https://doi.org/10.1063/1.3651914

CIRIA, CUR, & CETMEF. (2007). The rock manual. the use of rock in hydraulic engineering (2nd edition). *C683*.

de Almeida, E., van Gent, M., & Hofland, B. (2019). Damage characterization of rock slopes. *Journal of Marine Science and Engineering*, *7(1)*. https://doi.org/10.3390/jmse7010010

Franco, L., & Tomsicchio, G. (1992). Hydraulic and mathematical modelling of historical and modern seawalls for the defence of venice lagoon. *Coastal Engineering 1992*. https://doi.org/10.1061/9780872629332.144

Hofland, B., Disco, M., & van Gent, M. (2014). Damage characterization of rubble mound roundheads. *Coastlab 2014*.

Hofland, B., Raaijmakers, T., van Gent, M., & Liefhebber, F. (2011). Damage evaluation using the damage depth. *Proc. Coastal structures 2011*, 812–823. https://doi.org/10.1142/9789814412216_0070

Hudson, R. (1953). Laboratory investigation of rubble-mound breakwaters. *Journal of the Waterways and Harbors Division, ASCE*, *85(3)*. https://doi.org/10.1061/JWHEAU.000014

Hughes, S. (1993). *Physical models and laboratory techniques in coastal engineering*. World Scientific. https://doi.org/10.1142/2154

Irribaren, R. (1938). *Una fómula para el calculo de los diques de escollera*. Guipuzcoa, Spain.

Izbash, S. (1935). *Construction of dams by depositing rock in running water*. International Congress on Large Dams.

Jansen, P., & Schijf, J. (1953). The relation between the form of cross section the cross section, the method of revetment and the distribution of the water velocities in a waterway. *PIANC*, *18*, section SI C1.

Khan, D. (2011). Stabilization of angular-shaped riprap under overtopping flows. *World Academy of Science, Engineering and Technology*, *59*.

Kindsvater, C. (1964). Discharge characteristics of embankment shaped weirs. *U.S. Geological Survey Water Supply Paper*, *1617-A*.

Kramer, M., & Burcharth, H. (2004). Stability of low-crested breakwaters in shallow water short crested waves. *Proc. Coastal Structures 2003*. https://doi.org/10.1061/40733(147)12

Krishna, P., Indulekna, K., & Balan, K. (2016). Analysis of groyne placement on minimising river bank erosion. *Procedia Technology*, *24*, 47–53. https://doi.org/10.1016/j.protcy.2016.05.008

Lague, D., Brodu, N., & Leroux, J. (2013). Accurate 3d comparison of complex topography with terrestrial laser scanner: Application to the rangitikei canyon (n-z). *ISPRS Journal of Photogrammetry Remote Sensing*, *82*, 10–26. https://doi.org/10.1016/j.isprsjprs.2013.04.009

Lap, A. (1956). Fundamentals of ship resistance and propulsion. *International Shipbuilding Progress*, *3*(22).

Malik, S., & Pal, S. (2019). Is the construction of groynes accelerating the degradation of channel morphology and paved the way for human encroachment in the bengal basin? *Advances in Space research*, *64(8)*, 1549–1576. https://doi.org/10.1016/j.asr.2019.07.024

Melby, J., & Kobayashi, N. (1998). Progression and variability of damage on rubble mound breakwaters. *Journal of Waterway, Port, Coastal, and Ocean Engineering*, *124(6)*. https://doi.org/10.1061/(ASCE)0733-950X(1998)124:6(286)

Melling, G., Jansch, H., Kondziella, B., Uliczka, K., & Gätje, B. (2020). Evaluation of optimised groyne designs in response to long-period ship wave loads at juelssand in the lower elbe estuary. *Die Küste*, *89*, 29–56. 10.18171/1.089103

Schiereck, G., & Verhagen, H. (2012). *Introduction to bed bank and shore protection* (Second). VSSD Delft.

Schijf, J. (1949). Influence on the form and dimensions of the cross-section of the canal, of the form, of the speed and the propulsion system of vessels. *PIANC*, *17*, section 1.

Seemann, A., & Melling, G. (2021). A design method for rock groynes exposed to overtopping from long-period ship wave loads [manuscript submitted for publication]. *Journal of Coastal and Hydraulic Structures*.

Thielicke, W., & Stamhuis, E. (2014). Piv-lab - towards user-friendly, affordable and accurate digital particle image velocimetry in matlab. *Journal of Open Research Software*, *2(1)*. https://doi.org/10.5334/jors.bl

Thompson, D., & Shuttler, R. (1975). *Riprap design for wind-wave attack. a laboratory study in random waves*. HR Wallingford.

Thornton, C., Abt, S., Scholl, B., & Bender, T. (2014). Enhanced stone sizing for overtopping flow. *Journal of Hydraulic Engineering*, *140(4)*. https://doi.org/10.1061/(ASCE)HY.1943-7900.0000830

Uijttewaal, W. (2005). Effects of groyne layout on the flow in groyne fields: Laboratory experiments. *Journal of Hydraulic Engineering*, *131(9)*. https://doi.org/10.1061/(ASCE)0733-9429(2005)131:9(782)

Van der Wal, M. (1990). Heranalyse van m1155 onderzoeksresultaten. *Delft Hydraulics*, *Q902*.

van der Meer, J. (1988). *Rock slopes and gravel beaches under wave attack*. Delft Hydraulics Laboratory.

Vidal, C. (1995). Stability of low-crested rubble-mound breakwater heads. *Journal of Waterway Port Coastal and Ocean Engineering*, *121(2)*. https://doi.org/10.1061/(ASCE)0733-950X(1995)121:2(114)

WSABhv. (2021). Strombaulicher bericht zur bauwerksunterhaltung und zum ufersicherungs - konzept am niedersächischen ufer. *WSA Cuxhaven*.

WSACux. (2009). Strombaulicher bericht über den derzeitigen stand der bauwerksunterhaltung an den buhnen und leitwerken in der außenweser. *WSA Bremerhaven*.

Xiang, K., Yang, Z., Wu, S., Goa, W., & Li, D. (2020). Flow hydrodynamics of the mixing layer in consecutive vegetated groyne fields. *Physics of Fluids*, *32(6)*. https://doi.org/10.1063/5.0006317

A

Appendix: Dimensional analysis flow equation

A dimensional analysis is performed to express the flow velocity at the lee side of the groyne structure in a dimensionless form, based on the Buckingham-Pi theorem. A function (f) is determined based and the important variables during the Flow experiment:

$$f(u, h, \rho_w, R_c, g, \mu, \sigma, d_{n50,a}, \theta) \tag{A.1}$$

Where u = flow velocity along lee-side [m/s], h = water depth at wave facing side above crest [m], R_c = Free-board due drawdown [m], μ = dynamic viscosity of water [$kg/m^2/s$], ρ_w = water density [kg/m^3], σ = surface tension [N/m], $d_{n50,a}$ = rock diameter armour layer [m], θ = slope of structure [-].

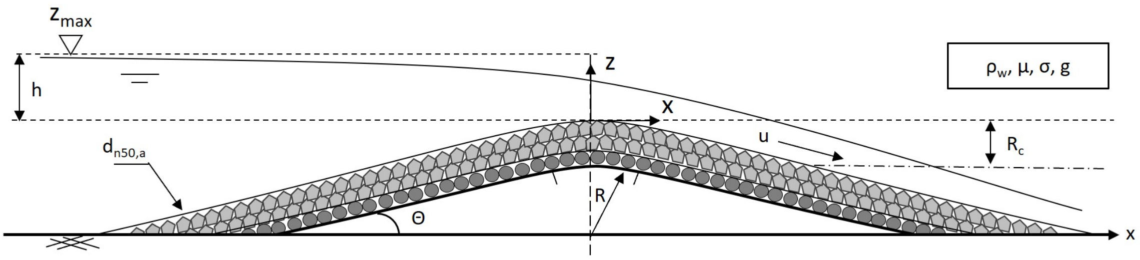

Figure A.1: Groyne during continuous overflow with corresponding parameters for dimensional analysis

The parameters h, ρ_w and g are used as dimensional independent variables in the Buckingham-Pi analysis, as these parameters describe the length, fluid and flow characteristics. The theorem states that for a physical system with n variables, there are n - k dimensionless groups that can be formed, in which k is the number of independent variables. There are in total n = 9 used variables and k = 3 dimensional quantities - mass [M], length [L] and time [T]. This results in n-k = 9 - 3 = 6 dimensionless groups and is denoted as Π_i.

Each variable n can be expressed in [M], [L], [T] and are made dimensionless by $\rho_w h^3$, h and $g^{-1/2}h^{1/2}$:

- Π_1: Flow velocity u
  u = [LT^{-1}] = h * $g^{1/2}h^{-1/2}$

$$\Pi_1 = \frac{u}{gh^{1/2}} \tag{A.2}$$

- Π_2: Assumed free-board R_c due drawdown
  R_c = [L] = h

$$\Pi_2 = \frac{R_c}{h} \tag{A.3}$$

- Π_3: Slope θ
  θ = [-]

$$\Pi_3 = \theta \tag{A.4}$$

- Π_4: Dynamic viscosity μ
  μ = [ML^{-1}T^{-1}] = $\rho_w h^-3$ * h^-1 * $g^{1/2} h^{-1/2}$

$$\Pi_4 = \frac{\mu}{\rho_w h^{3/2} g^{1/2}} \tag{A.5}$$

- Π_5: Surface tension σ
  σ = [MLT^{-2}L^{-1}] = ρ_w h^3 * $h^{-1/2}$ $g^{1/2}$

$$\Pi_5 = \frac{\sigma}{\rho_w h^2 g} \tag{A.6}$$

- Π_6: Rock diameter $d_{n50,a}$
  $d_{n50,a}$ = [L] = h

$$\Pi_6 = \frac{d_{n50,a}}{h} \tag{A.7}$$

Applying all new dimensionless equations (Π_1 to Π_6) into the functional equation (Equation A.1), results in the new dimensionless functional equation which expresses Π_1:

$$\Pi_1 = f(\Pi_2, \Pi_3, \ldots, \Pi_6) \tag{A.8}$$

New dimensionless groups can be formed by products of the powers of the dimensionless groups obtained in the previous step. This results in new Π groups.

$$\Pi_{1,1} = \frac{{\Pi_1}^2}{2} = \frac{u^2}{2gh} \tag{A.9}$$

$$\Pi_{1,4} = \frac{\Pi_1}{\Pi_4} = \frac{\rho u h}{\mu} = Re \tag{A.10}$$

$$\Pi_{1/5} = \frac{1}{\Pi_5} = \frac{\rho_w h^2 g}{\sigma} = We \tag{A.11}$$

$$\Pi_{2,6} = \frac{\Pi_2}{\Pi_6} = \frac{R_c}{d_{n50,a}} \tag{A.12}$$

For experimental measurements on scaled physical modelled structures are the effects of the Reynolds number and the Weber number only significant for low values. If the water depth during an experiment is larger than 5 cm, it can be assumed that the Weber number is too small and could be neglected (Chanson, 2004). For the Reynolds number, one can neglect if there is fully rough turbulence (Re > 30000) (Chanson, 2004). By taking these two statements into account, the functional equation can be rewritten into a reduced and final form:

$$\Pi_1 = f(\Pi_{2,6}, \Pi_7) \tag{A.13}$$

$$\frac{u^2}{gh} = f(\frac{R_c}{d_{n50,a}}, \theta) \tag{A.14}$$

B

Appendix: Cross-section scans prototype

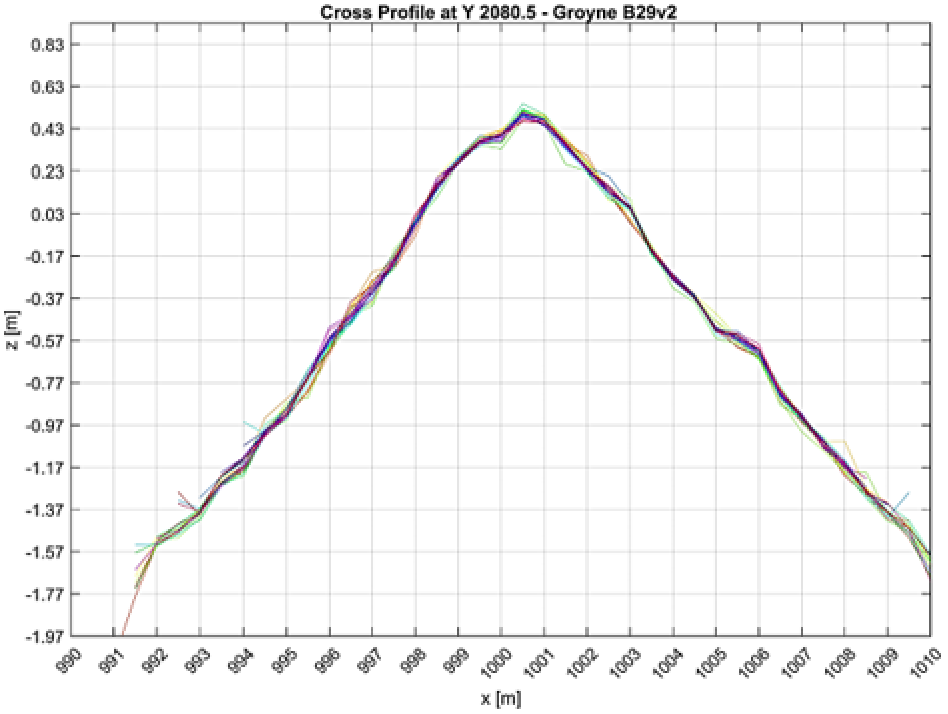

Figure B.1: Cross-section scans of prototype groyne

C

Appendix: Physical model design calculation

Physical model ratio

To get the least scale distortions during the experiments is the largest model the best (Chanson, 2004) and it must fulfil the requirements presented in Section 2.4 Physical Modelling guidelines. For the Flow experiment the measurements must be conducted through the windows of the flume by a camera. This results in a limitation of the size of the model. Therefore, the model height + the overflowing water depth must be within the range of the transparent sides of 34 by 75 cm in height and length. The maximum overflowing hydraulic head over the model (h) is going to be increased by 50 % as stated in the previous section. This results in the following limitation for the physical model:

$$P_m + 1.5h_{max} < 0.34 \tag{C.1}$$

For:

$$0 < h/P < 0.9 \tag{C.2}$$

Here, P_m is the crest height of the physical model and h is the maximum hydraulic head. The next step is to determine which scaling ratio (L_r) provides the largest model within the mentioned limitation.

The following scaling ratios are tested: L_r = 12, 13, 14 and 15. By applying the Froude similarity the following dimensions are calculated and presented in Table C.1. Here, it is shown that the largest scaling ratio within the height of the transparent flume of 34 cm is L_r = 13 and is used for the scaling of the model.

Table C.1: Groyne height P and hydraulic head h for scaling ratios L_r = 1 and 12 to 15

L_r	P [m]	1.5*h_{max} [m]	P+1.5*h_{max} [m]
1	2.33	1.5*1.40 [m]	4.43
12	0.195	1.5*1.116 [m]	0.369
13	0.179	1.5*1.107 [m]	0.340
14	0.166	1.5*1.100 [m]	0.316
15	0.155	1.5*1.093 [m]	0.295

Physical model dimensions

The physical model will be scaled to a scaling ratio Lr = 13, as this results in the largest model possible in the flume which still allows measurements of the flow velocities and water depth through the transparent side. The outer dimensions for each model, scaled with Lr = 13 ratios, are derived via the Froude similarity and results are as shown in Table C.2.

Table C.2: Dimensions of the prototype groyne scaled into the physical model for scaling ratio L_r = 13

	Prototype [-]	Model 1 Flow	Model 2 Flow	Model 3 Flow	Model 4 Flow	Model 5 Damage
P [m]	2.33	0.179	0.179	0.179	0.179	0.179
W_c [m]	2	0.154	0.154	0.154	0.154	0.154
W_s [m]	8.5	0.654	0.654	0.508	0.508	0.654
W [m]	19	1.462	1.462	1.170	1.170	1.462
θ [-]	1:4	1:4	1:4	1:3	1:3	1:4
R [m]	3.9	0.3	0.3	0.3	0.3	0.3
Armour material	Iron silicate	Basalt	Granite	Basalt	Granite	Basalt
Attachment	Loose	Fixed	Fixed	Fixed	Fixed	Loose

Rock dimensions armour layer

The prototype rock grading used in the armour layer is LM$_{b5/40}$ with a corresponding d$_{50}$ = 18-23 cm and a d$_{85}$/d$_{15}$ ratio of 1.7 (EN 13383-1, 2011). The material of these rocks is iron-silicate which has a specific density of approximately 3.8 t/m^3. This material is relatively uncommon for the construction of rock structures in the Netherlands and therefore it is hard to get hold of, let aside that the correct model rock diameters should be available. This resulted in the required rock density cannot be reached for the physical model design. Therefore, an additional scaling method is applied next to the Froude scaling and is based on the Izbash equation.

The armour layer of Models 1, 3 and 5 are scaled by the Izbash equation, whereas Models 2 and 4 are still scaled by the Froude similarity. The Izbash stability equation includes the density of the rock and water (via the relative density $\Delta = (\rho_s - \rho_w)/\rho_w$), rock diameter (d$_{50}$) and critical flow velocity (u$_c$). The unknown model rock diameter is determined by equalizing the Izbash formula of the prototype to the model, as shown in Equation 4.2.

$$\left(\frac{u_c}{\sqrt{\Delta g d}}\right)_p = \left(\frac{u_c}{\sqrt{\Delta g d}}\right)_m \tag{C.3}$$

The physical model of the groyne is going to be scaled into a 1:13 ratio (Lr = 13) via Froude similarity, which states that the ratio of the flow velocity of the model and the prototype can be expressed in the square root of the scaling ratio:

$$\sqrt{L_r} = \frac{u_{c,p}}{u_{c,m}} \tag{C.4}$$

As stated, the prototype stone material iron-silicate (ρ_s = 3800 kg/m^3) is unavailable to use for the physical model of the groyne structure. Normally, standard stone material like Granite has a specific weight of approximately 2600 kg/m^3. An available material with a higher specific weight compared to normal stone material is Basalt, which has a specific weight of approximately ρ_s = 3000 kg/m^3.

By using Equations C.3, C.4 and the specific weight of the material is the diameter of the rocks in the physical model calculated.

$$\frac{\sqrt{13}}{\sqrt{\Delta_p * g * d_{50,p}}} = \frac{1}{\sqrt{\Delta_m * g * d_{50,m}}} \rightarrow d_{50,m,a,basalt} = 0.022m \tag{C.5}$$

This results in a model rock diameter $d_{50,m,basalt}$ = 0.022m to be applied as rock armour for the physical models 1, 3, and 5 when the stone material Basalt is used.

Rock armour of Models 2 and is made from of common stone material Granite and scaled by Froude similarity as the specific density is unimportant for the glued armor layer. This results in the $d_{50,m,a,granite}$ = 0.015m.

Rock dimensions filter layer

The prototype rock grading used in the filter layer is CP 90/250 with a corresponding d_{50} of approximately 17 cm (EN 13383-1, 2011). The material of these rocks is also iron-silicate which has a specific density of approximately 3.8 t/m^3. The scaled rock dimension of this filter material is going to be glued to the aluminium core of all models and therefore the specific density is unimportant for the scaling. Therefore, this filter layer can be scaled via the Froude similarity, which results in a rock size of the filter material at the model of $d_{50,f}$ = 0.013 meters.

All dimensions of all models are summarized in Table C.3 with d_{n50} = 0.84 *d_{50}.

Table C.3: Dimension of parameters of the physical models with nominal stone diameter.

	Prototype [-]	Model 1 Flow	Model 2 Flow	Model 3 Flow	Model 4 Flow	Model 5 Damage
P [m]	2.33	0.179	0.179	0.179	0.179	0.179
W_c [m]	2	0.154	0.154	0.154	0.154	0.154
W_s [m]	8.5	0.654	0.654	0.508	0.508	0.654
W [m]	19	1.462	1.462	1.170	1.170	1.462
θ [-]	1:4	1:4	1:4	1:3	1:3	1:4
R [m]	3.9	0.3	0.3	0.3	0.3	0.3
Armour material	Iron silicate	Basalt	Granite	Basalt	Granite	Basalt
$d_{n50,a}$ [m]	0.168	0.019	0.013	0.019	0.013	0.019
$d_{n50,f}$ [m]	0.143	0.010	0.010	0.010	0.010	0.010
Attachment	Loose	Fixed	Fixed	Fixed	Fixed	Loose

D

Appendix: Division of tasks

During this thesis and the corresponding experiments, a collaboration with Dr Ahmad alYousif was carried out. For the flow experiment, we worked together to measure the flow velocities using the PIV setup. Dr. Ahmad alYousif did the image processing for the PIVlab, while I started the damage experiment.

Table D.1: Division of tasks during the flow and damage experiments

Experiment steps	Explanation	Tobias van Batenburg	Dr. Ahmad alYousif
Flow experiment		x	x
Model fabrication	Model fabrication, ordering material, determine dimensions.	x	
Experimental Setup	Designing PIV setup (determine particle concentration, illumination time, camera frequency etc.)	x	x
Performing experiment		x	x
Image processing PIV	All taken PIV frames are processed (apply filters, masking, processing methods, etc.) in Matlab Package PIVlab to obtain flow velocity data per extraction line.		x
Data analysis	Flow velocity per extraction lines are analysed by Python code to construct flow velocity equations.	x	
Writing Thesis	All parts in the thesis about everything that has to do with the flow experiments.	x	
Writing a paper	A paper about the flow experiment.		x
Damage experiment		x	
Model fabrication	Model fabrication, ordering material, determine dimensions.	x	
Experimental Setup	Design damage experiment setup (placement GCPs, camera positions, wave-structure interaction etc.)	x	
Performing experiment		x	
Constructing 3D models	All images are processed by Agisoft Metshape software and Cloudcompare.	x	
Data analysis	Profile changes are analysed by Python code to obtain damage parameters.	x	
Writing Thesis	All parts in the thesis about everything that has to do with the damage experiments.	x	
Writing paper		x	

E

Appendix: Damage measurements

This Appendix presents the changes in the profile per measured wave.

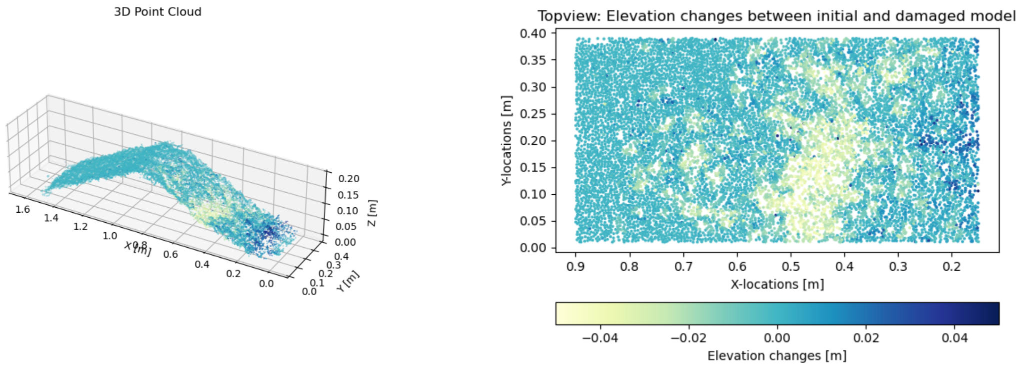

(a) 3D view profile changes

(b) Top view profile change crest and lee side

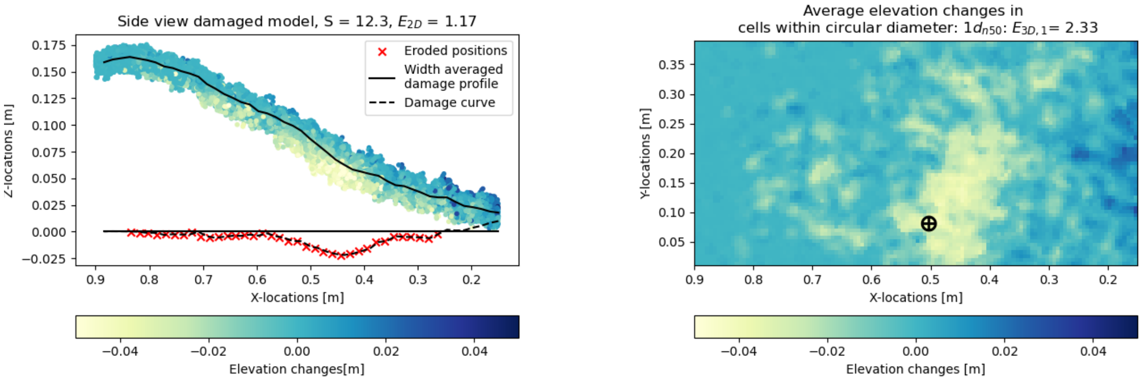

(c) Side view profile changes

(d) Spatially averaged top view profile changes crest and lee side

Figure E.1: 3D view, width-averaged side view and spatially averaged top view of damaged profile for wave height H = 6.89 cm and freeboard R_c = 10.9 cm.

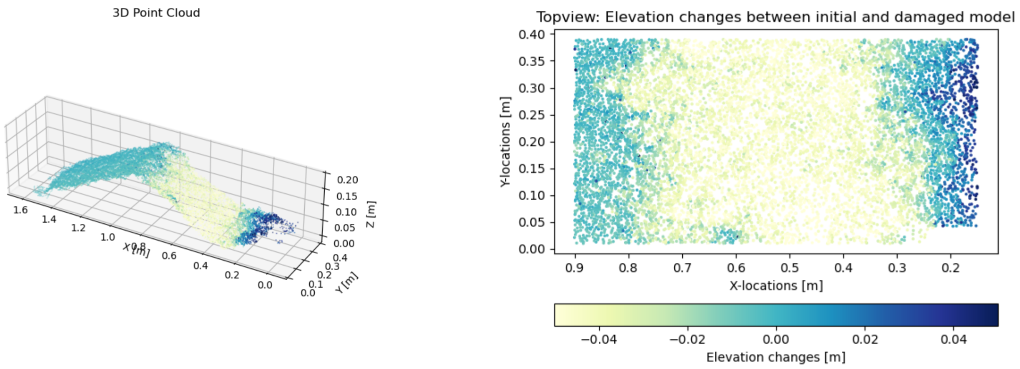

(a) 3D view profile changes

(b) Top view profile change crest and lee side

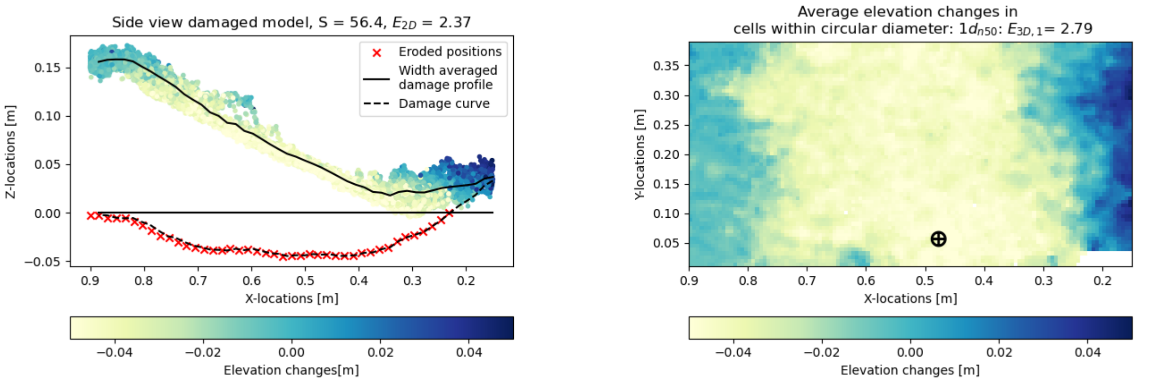

(c) Side view profile changes

(d) Spatially averaged top view profile changes crest and lee side

Figure E.2: 3D view, width-averaged side view and spatially averaged top view of damaged profile for wave height H = 10.89 cm and freeboard R_c = 10.9 cm.

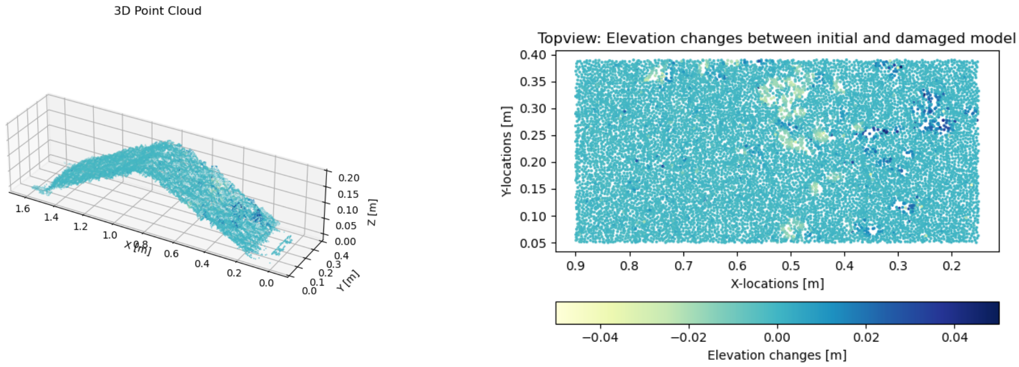

(a) 3D view profile changes

(b) Top view profile change crest and lee side

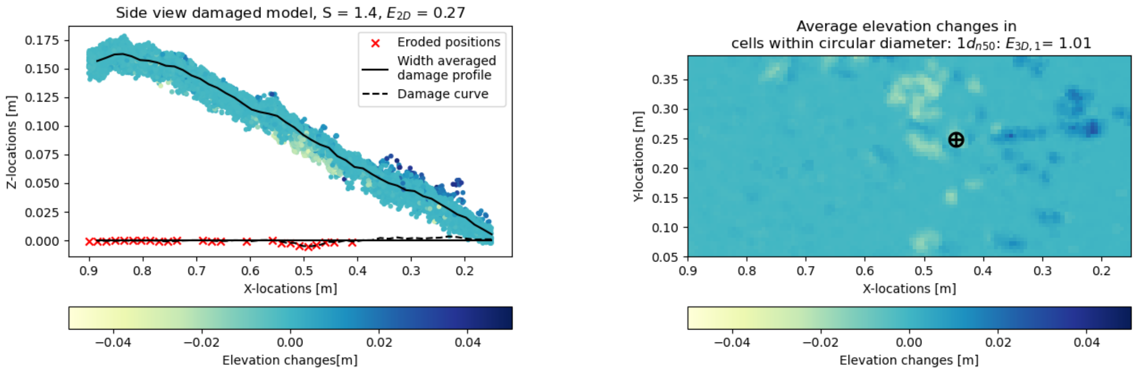

(c) Side view profile changes

(d) Spatially averaged top view profile changes crest and lee side

Figure E.3: 3D view, width-averaged side view and spatially averaged top view of damaged profile for wave height H = 3.27 cm and freeboard R_c = 8.2 cm.

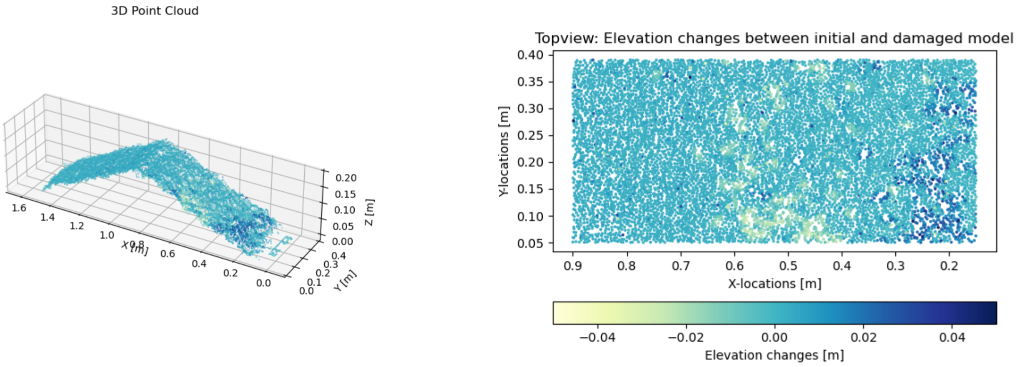

(a) 3D view profile changes

(b) Top view profile change crest and lee side

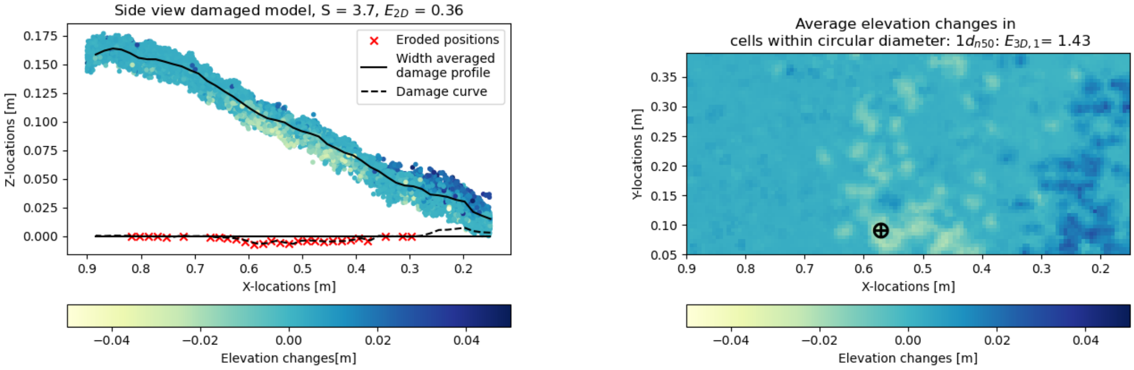

(c) Side view profile changes

(d) Spatially averaged top view profile changes crest and lee side

Figure E.4: 3D view, width-averaged side view and spatially averaged top view of damaged profile for wave height H = 6.09 cm and freeboard R_c = 8.2 cm.

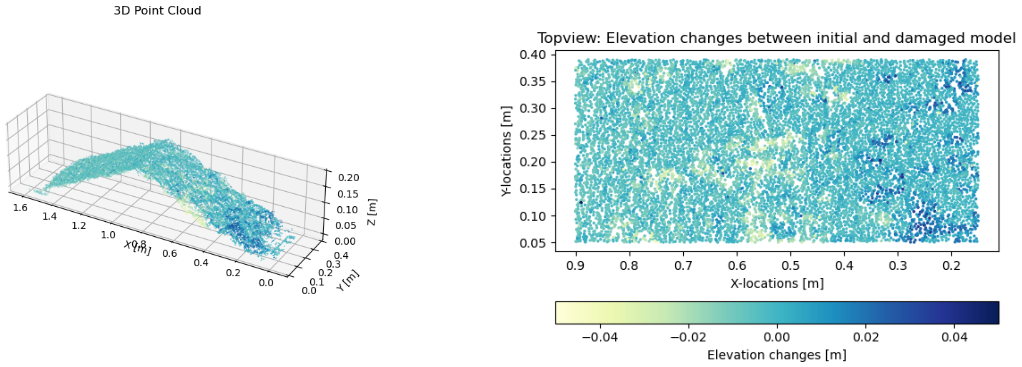

(a) 3D view profile changes

(b) Top view profile change crest and lee side

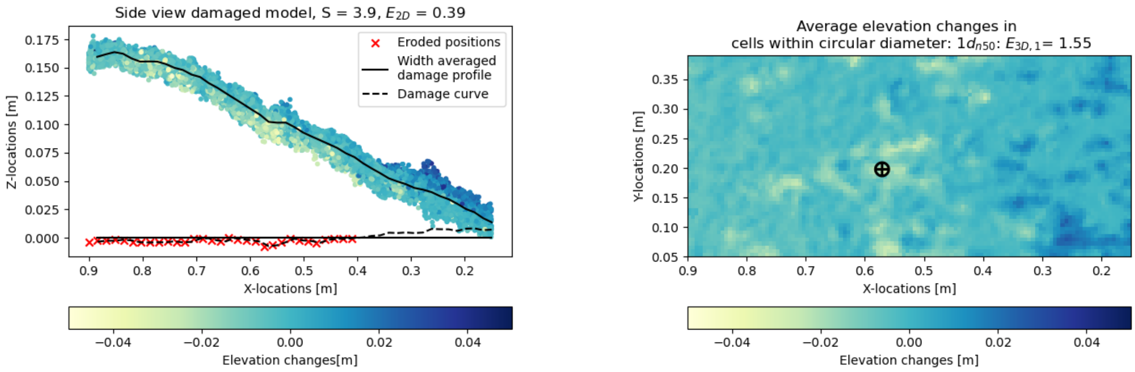

(c) Side view profile changes

(d) Spatially averaged top view profile changes crest and lee side

Figure E.5: 3D view, width-averaged side view and spatially averaged top view of damaged profile for wave height H = 7.2 cm and freeboard R_c = 8.2 cm.

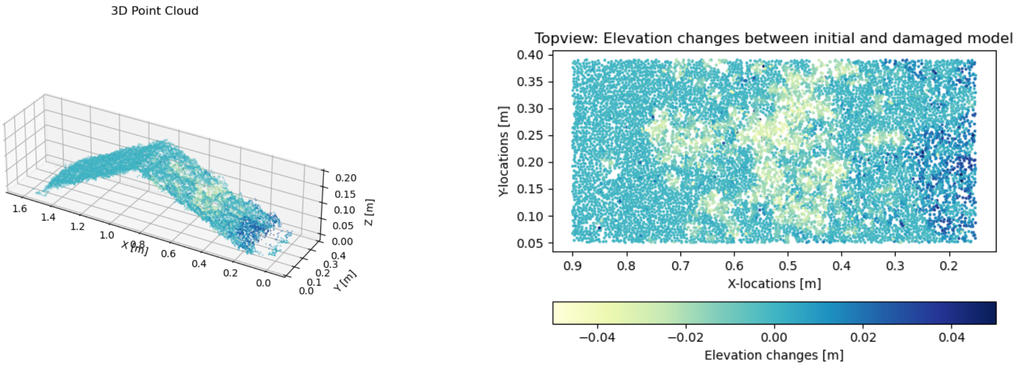

(a) 3D view profile changes

(b) Top view profile change crest and lee side

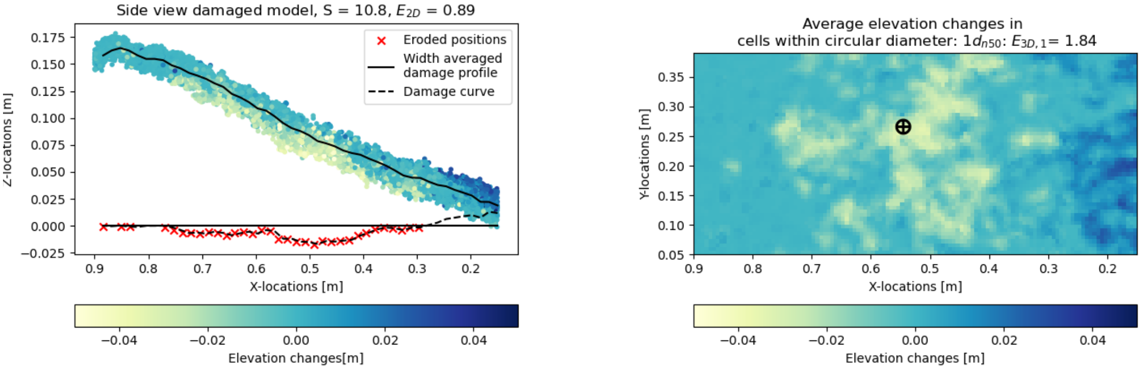

(c) Side view profile changes

(d) Spatially averaged top view profile changes crest and lee side

Figure E.6: 3D view, width-averaged side view and spatially averaged top view of damaged profile for wave height H = 9.84 cm and freeboard R_c = 8.2 cm.

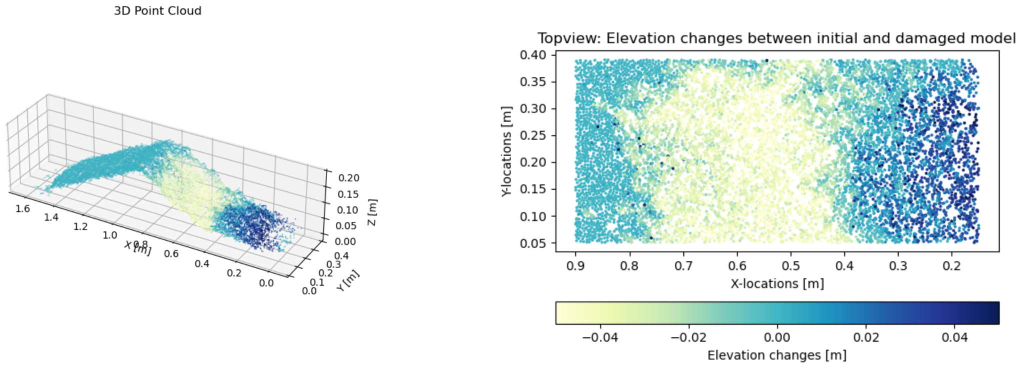

(a) 3D view profile changes

(b) Top view profile change crest and lee side

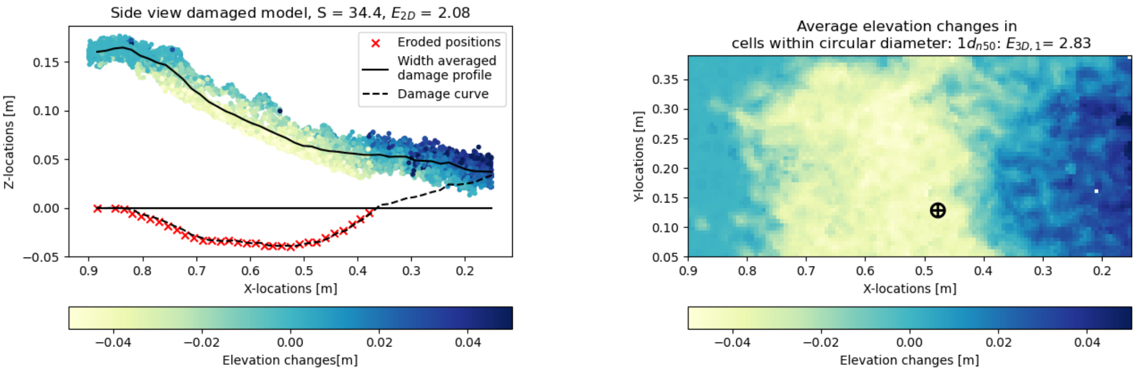

(c) Side view profile changes

(d) Spatially averaged top view profile changes crest and lee side

Figure E.7: 3D view, width-averaged side view and spatially averaged top view of damaged profile for wave height H = 11.86 cm and freeboard R_c = 8.2 cm.

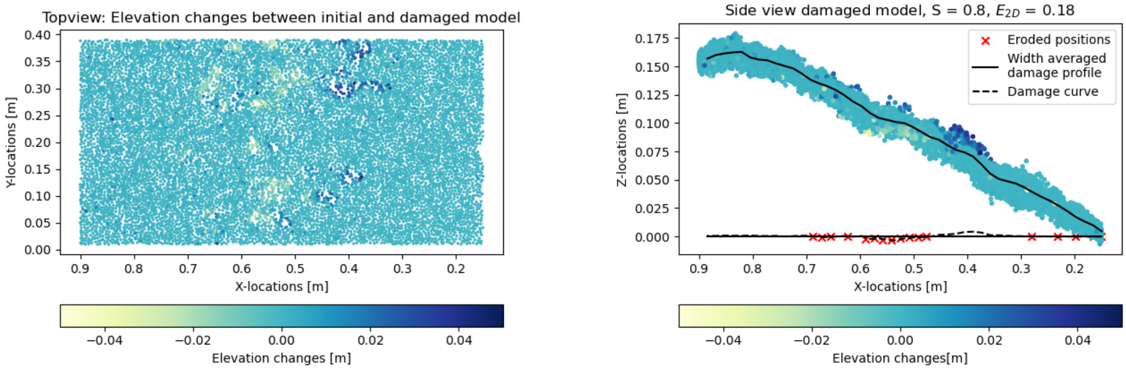

(a) Top view profile change crest and lee side

(b) Side view profile changes

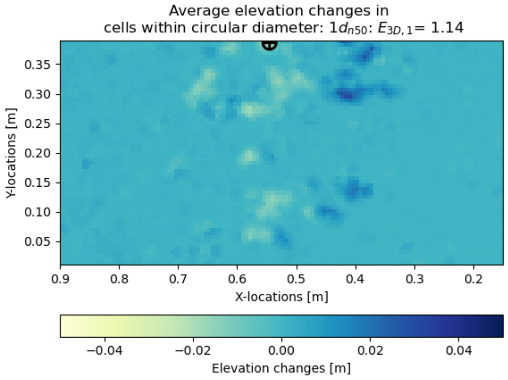

(c) Spatially averaged top view profile changes crest and lee side

Figure E.8: 3D view, width-averaged side view and spatially averaged top view of damaged profile for wave height H = 3.84 cm and freeboard R_c = 5.5 cm.

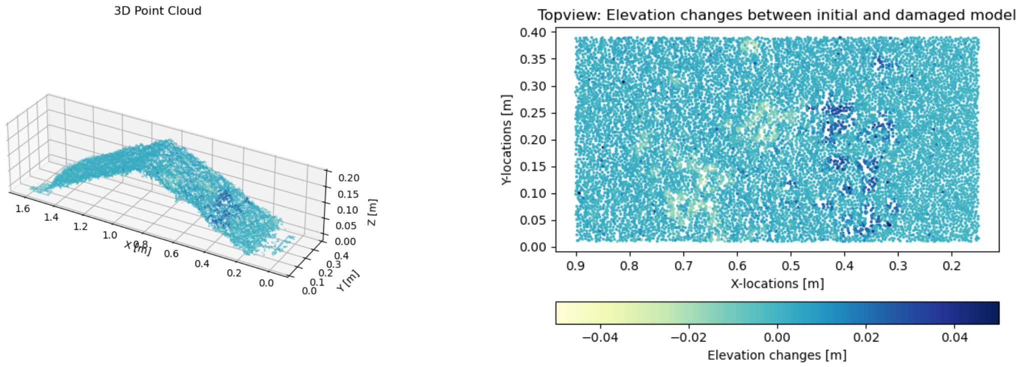

(a) 3D view profile changes

(b) Top view profile change crest and lee side

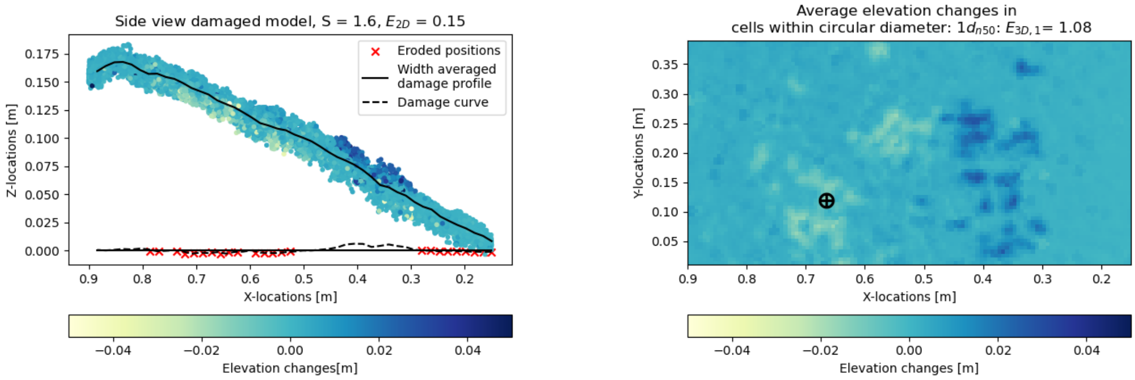

(c) Side view profile changes

(d) Spatially averaged top view profile changes crest and lee side

Figure E.9: 3D view, width-averaged side view and spatially averaged top view of damaged profile for wave height H = 4.62 cm and freeboard R_c = 5.5 cm.

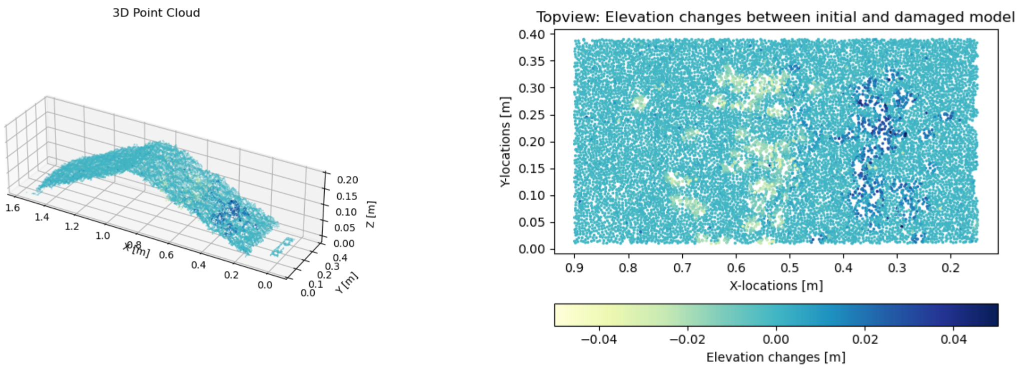

(a) 3D view profile changes

(b) Top view profile change crest and lee side

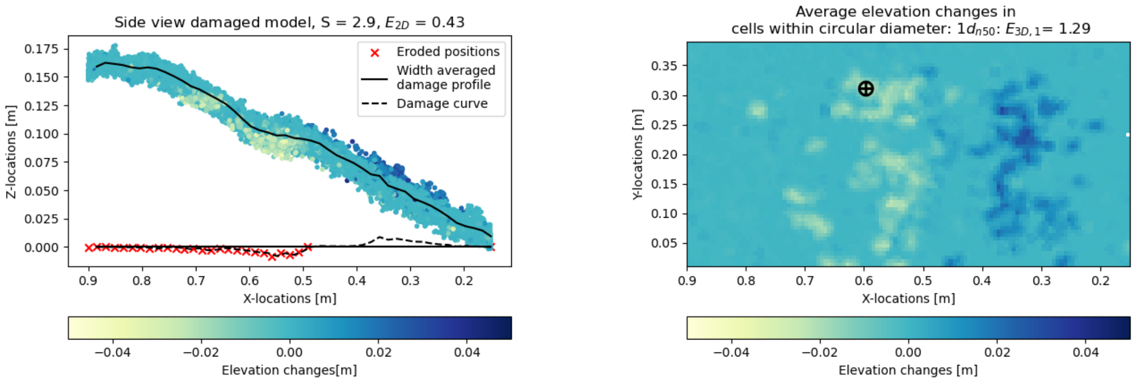

(c) Side view profile changes

(d) Spatially averaged top view profile changes crest and lee side

Figure E.10: 3D view, width-averaged side view and spatially averaged top view of damaged profile for wave height H = 6.77 cm and freeboard R_c = 5.5 cm.

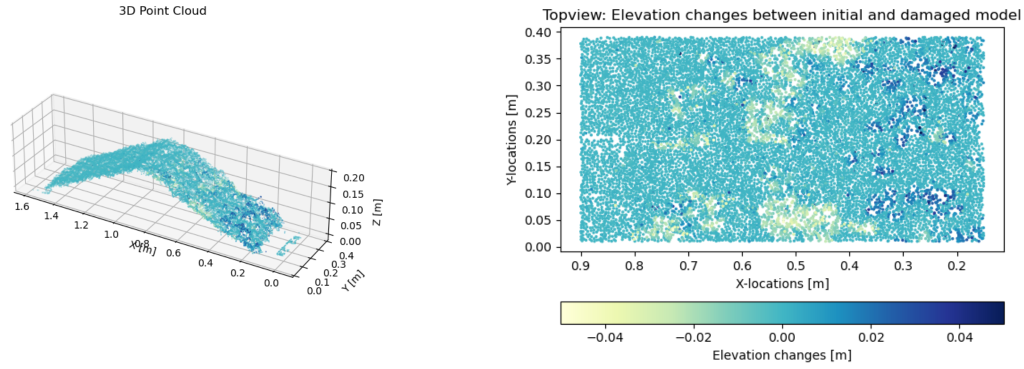

(a) 3D view profile changes

(b) Top view profile change crest and lee side

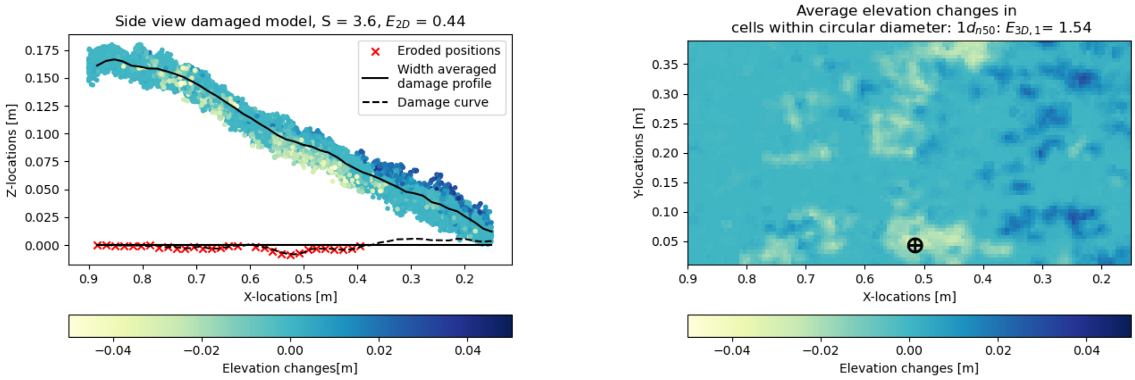

(c) Side view profile changes

(d) Spatially averaged top view profile changes crest and lee side

Figure E.11: 3D view, width-averaged side view and spatially averaged top view of damaged profile for wave height H = 9.65 cm and freeboard R_c = 5.5 cm.

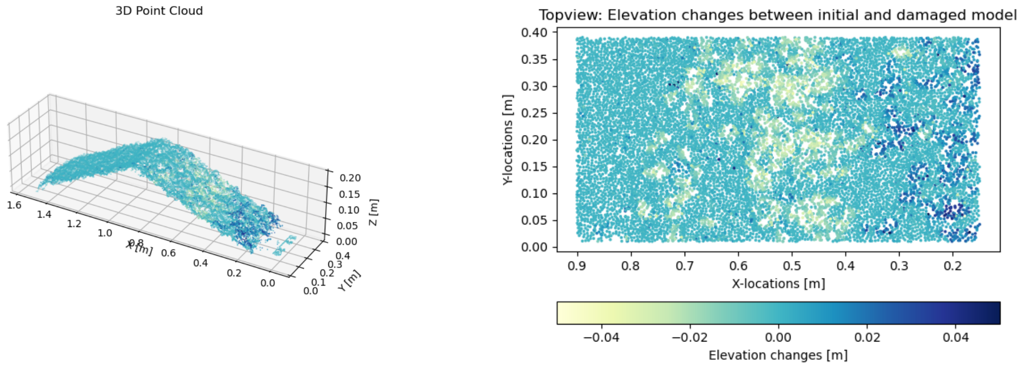

(a) 3D view profile changes

(b) Top view profile change crest and lee side

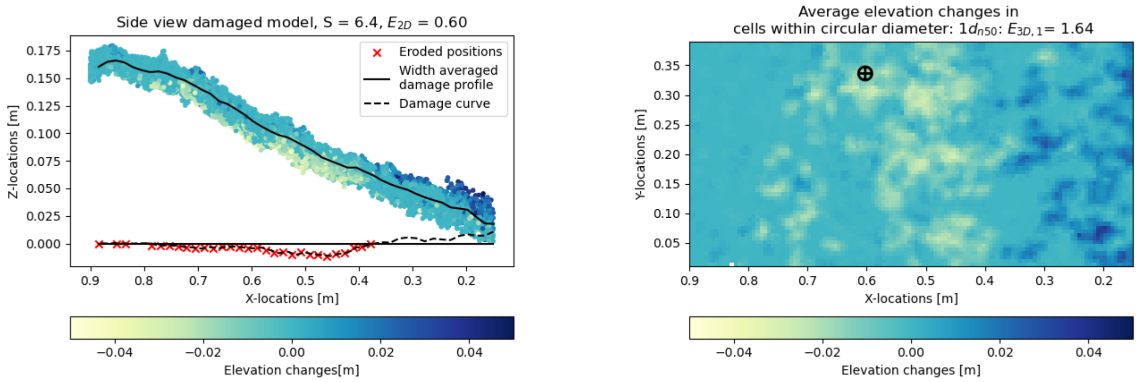

(c) Side view profile changes

(d) Spatially averaged top view profile changes crest and lee side

Figure E.12: 3D view, width-averaged side view and spatially averaged top view of damaged profile for wave height H = 10.61 cm and freeboard R_c = 5.5 cm.

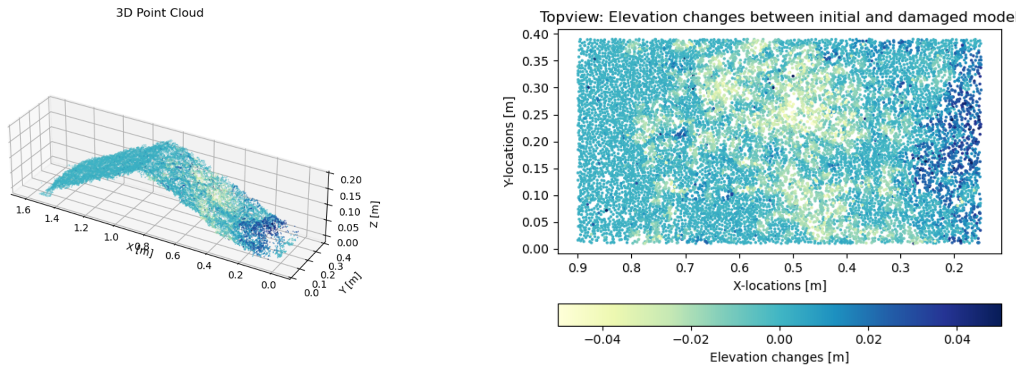

(a) 3D view profile changes

(b) Top view profile change crest and lee side

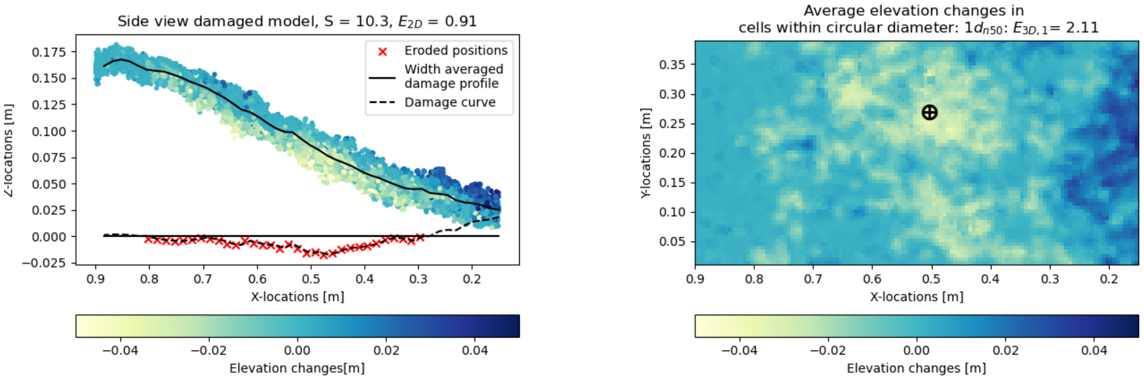

(c) Side view profile changes

(d) Spatially averaged top view profile changes crest and lee side

Figure E.13: 3D view, width-averaged side view and spatially averaged top view of damaged profile for wave height H = 12.4 cm and freeboard R_c = 5.5 cm.

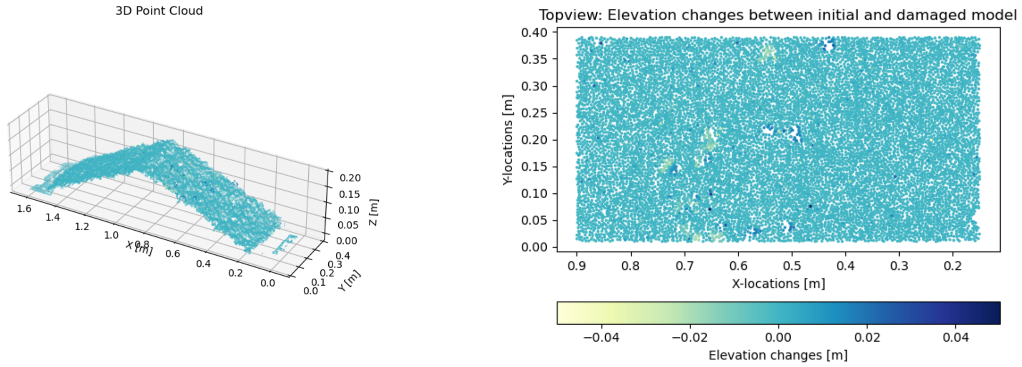

(a) 3D view profile changes

(b) Top view profile change crest and lee side

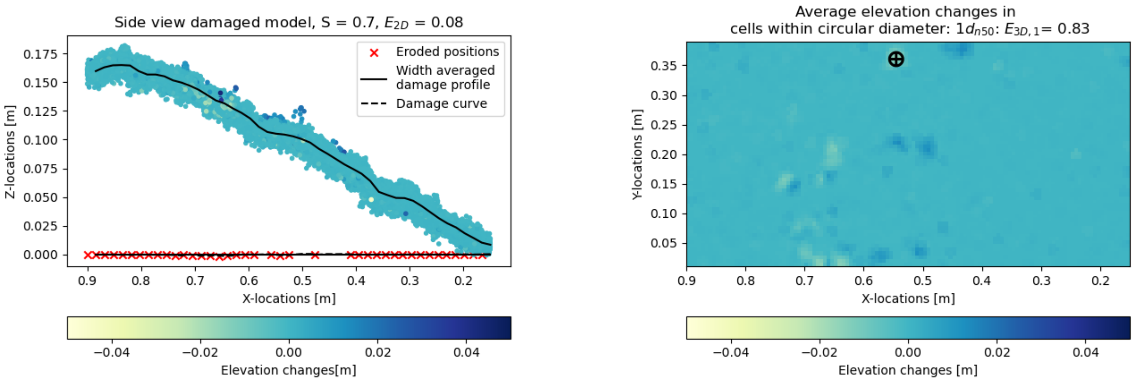

(c) Side view profile changes

(d) Spatially averaged top view profile changes crest and lee side

Figure E.14: 3D view, width-averaged side view and spatially averaged top view of damaged profile for wave height H = 3.86 cm and freeboard R_c = 2.7 cm.

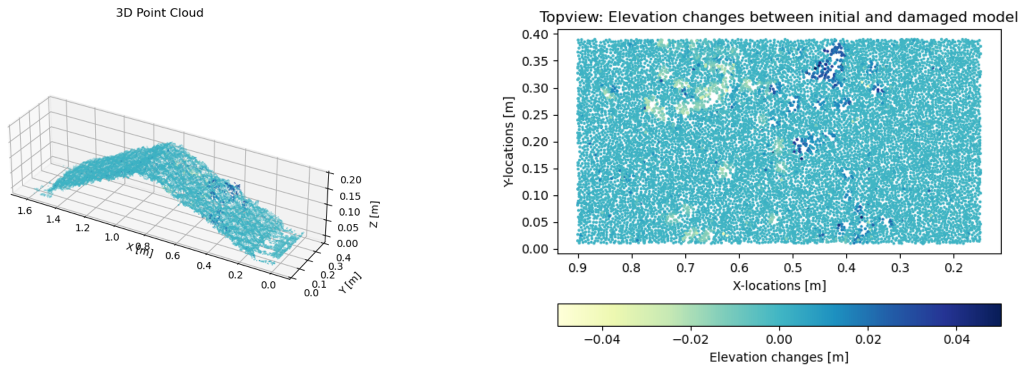

(a) 3D view profile changes

(b) Top view profile change crest and lee side

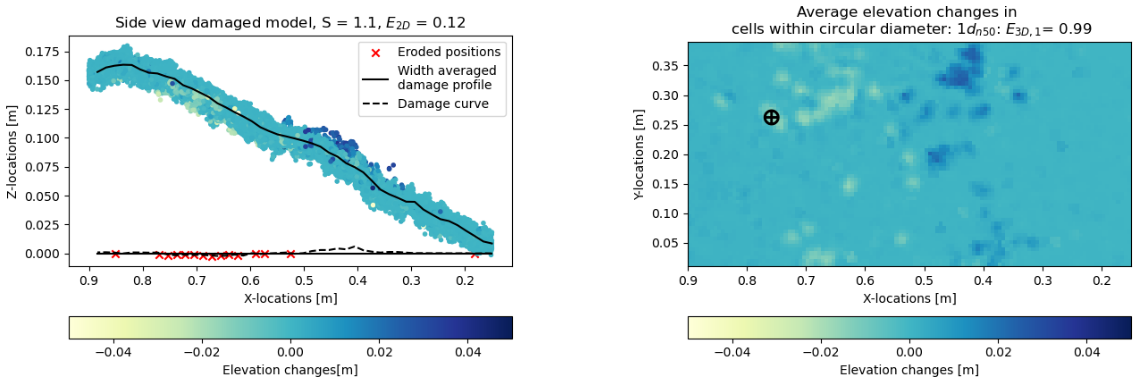

(c) Side view profile changes

(d) Spatially averaged top view profile changes crest and lee side

Figure E.15: 3D view, width-averaged side view and spatially averaged top view of damaged profile for wave height H = 6.25 cm and freeboard R$_c$ = 2.7 cm.

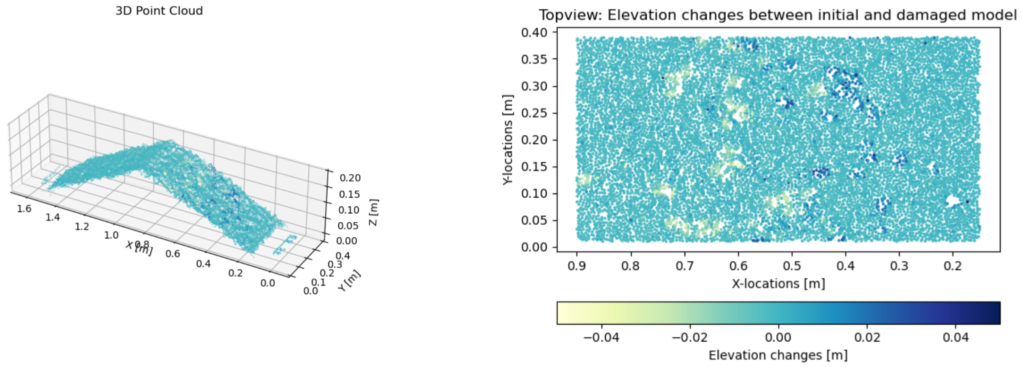

(a) 3D view profile changes

(b) Top view profile change crest and lee side

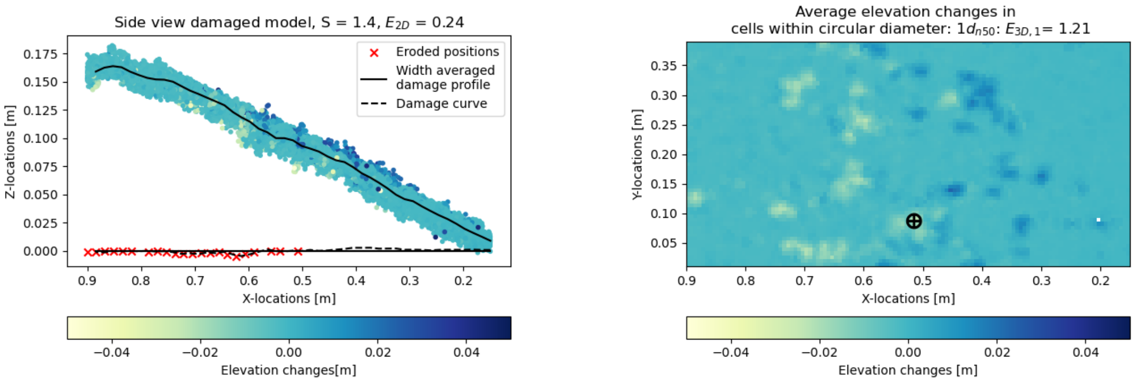

(c) Side view profile changes

(d) Spatially averaged top view profile changes crest and lee side

Figure E.16: 3D view, width-averaged side view and spatially averaged top view of damaged profile for wave height H = 8.28 cm and freeboard R_c = 2.7 cm.

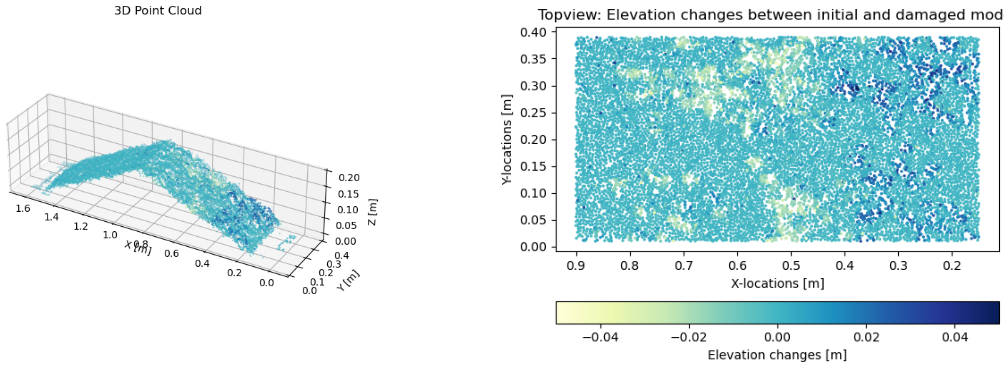

(a) 3D view profile changes

(b) Top view profile change crest and lee side

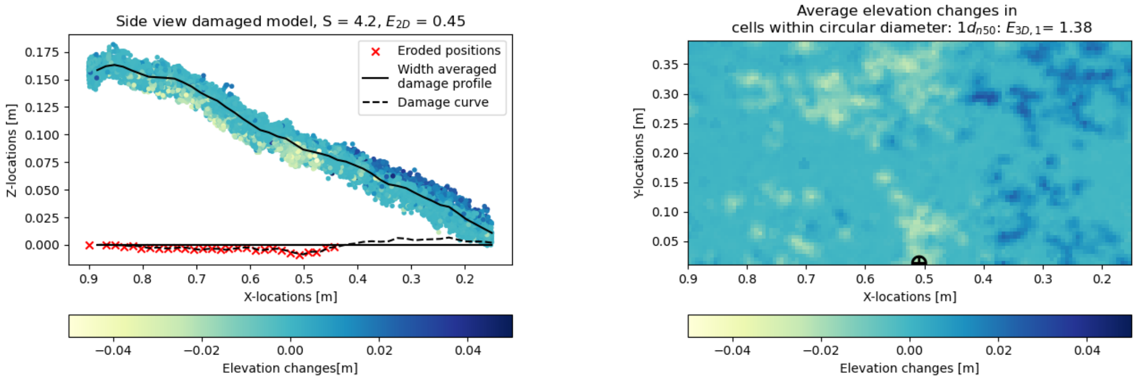

(c) Side view profile changes

(d) Spatially averaged top view profile changes crest and lee side

Figure E.17: 3D view, width-averaged side view and spatially averaged top view of damaged profile for wave height H = 11.23 cm and freeboard R_c = 2.7 cm.

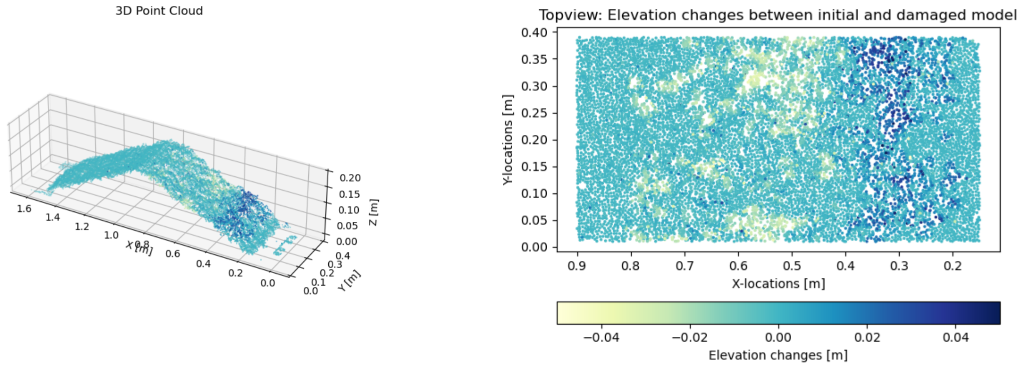

(a) 3D view profile changes

(b) Top view profile change crest and lee side

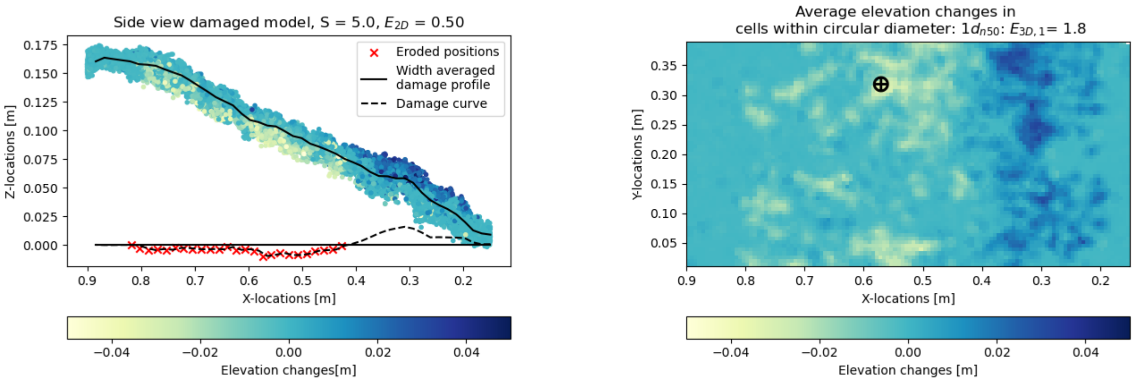

(c) Side view profile changes

(d) Spatially averaged top view profile changes crest and lee side

Figure E.18: 3D view, width-averaged side view and spatially averaged top view of damaged profile for wave height H = 11.56 cm and freeboard R_c = 2.7 cm.

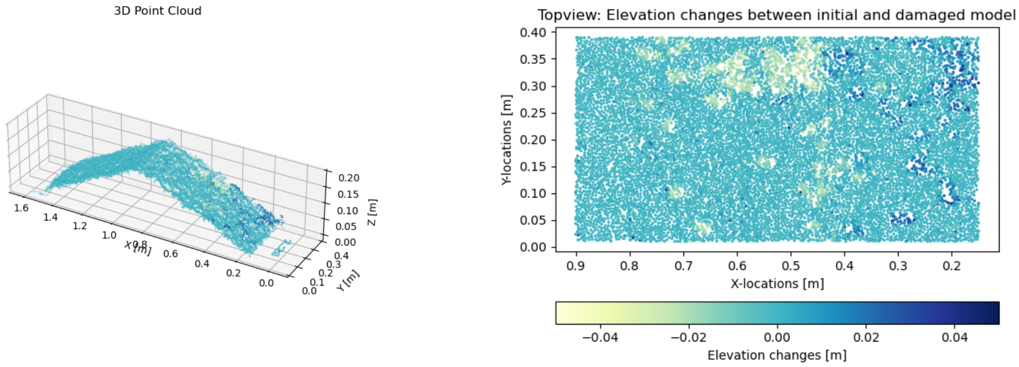

(a) 3D view profile changes

(b) Top view profile change crest and lee side

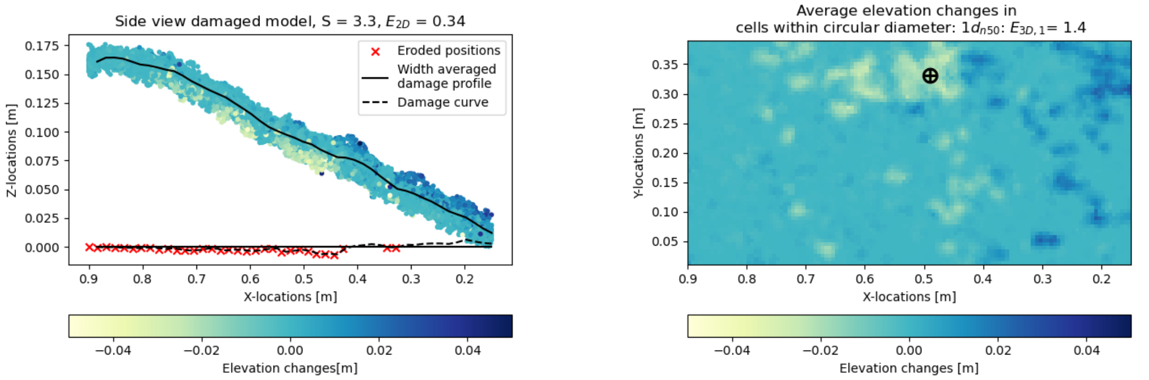

(c) Side view profile changes

(d) Spatially averaged top view profile changes crest and lee side

Figure E.19: 3D view, width-averaged side view and spatially averaged top view of damaged profile for wave height H = 12.55 cm and freeboard R_c = 2.7 cm.

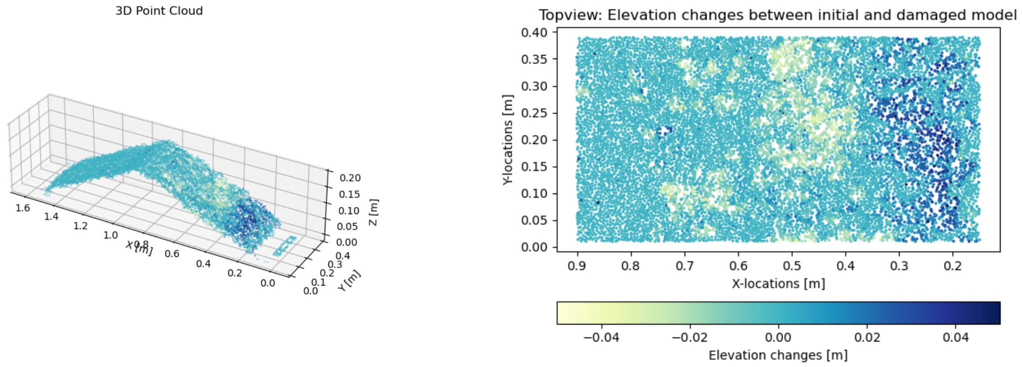

(a) 3D view profile changes

(b) Top view profile change crest and lee side

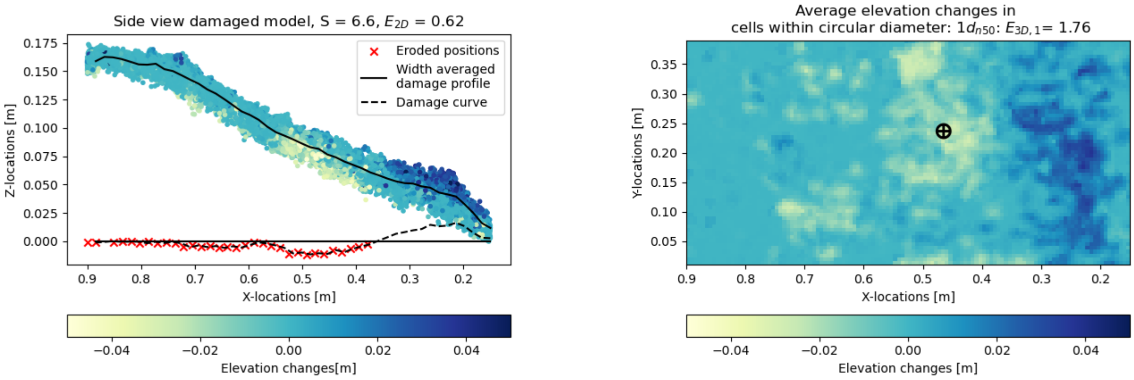

(c) Side view profile changes

(d) Spatially averaged top view profile changes crest and lee side

Figure E.20: 3D view, width-averaged side view and spatially averaged top view of damaged profile for wave height H = 13.15 cm and freeboard R_c = 2.7 cm.

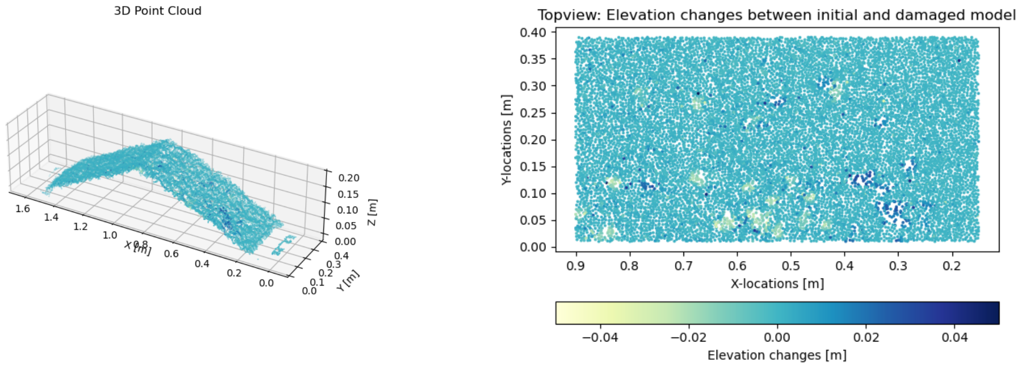

(a) 3D view profile changes

(b) Top view profile change crest and lee side

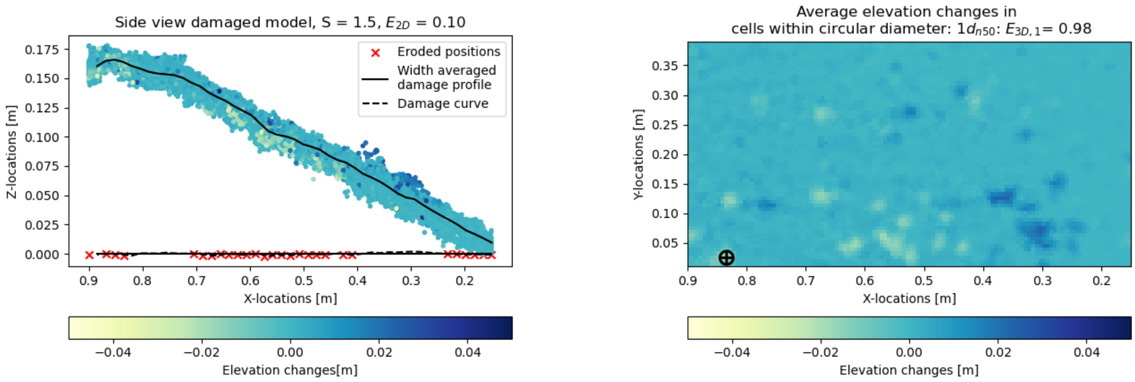

(c) Side view profile changes

(d) Spatially averaged top view profile changes crest and lee side

Figure E.21: 3D view, width-averaged side view and spatially averaged top view of damaged profile for wave height H = 10.64 cm and freeboard R_c = 0 cm.

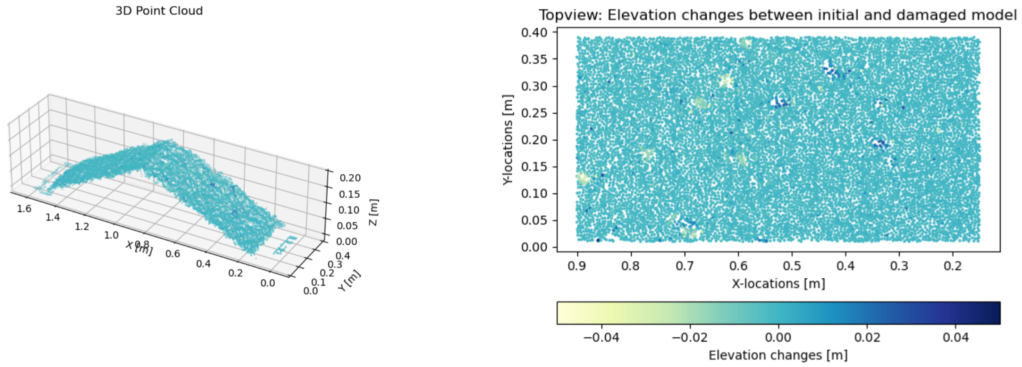

(a) 3D view profile changes

(b) Top view profile change crest and lee side

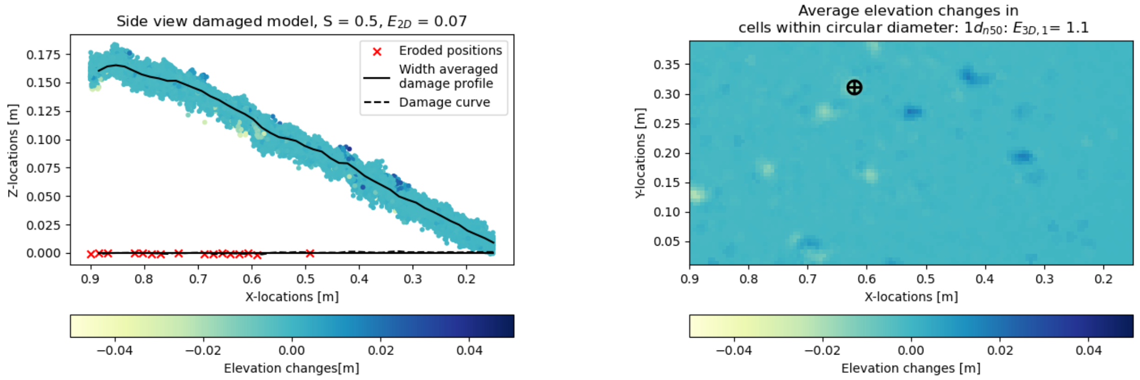

(c) Side view profile changes

(d) Spatially averaged top view profile changes crest and lee side

Figure E.22: 3D view, width-averaged side view and spatially averaged top view of damaged profile for wave height H = 11.01 cm and freeboard R_c = 0 cm.

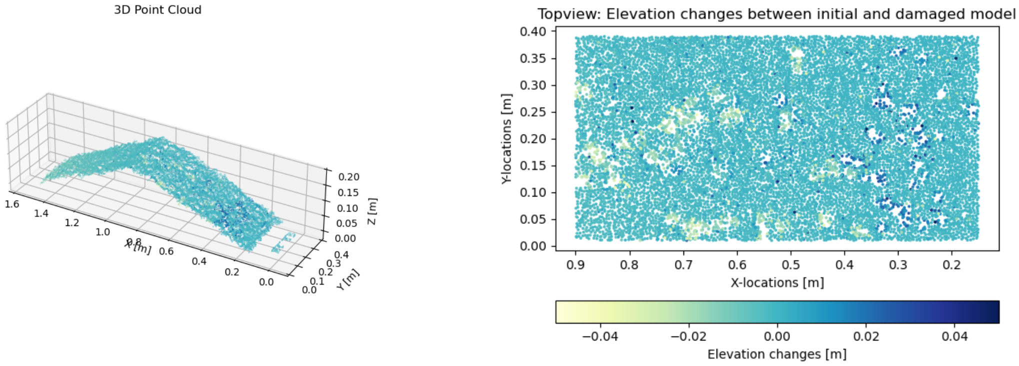

(a) 3D view profile changes

(b) Top view profile change crest and lee side

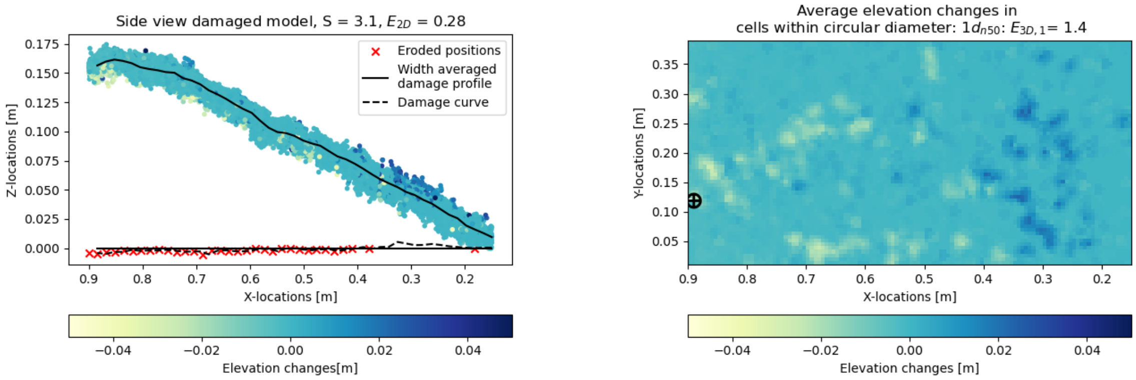

(c) Side view profile changes

(d) Spatially averaged top view profile changes crest and lee side

Figure E.23: 3D view, width-averaged side view and spatially averaged top view of damaged profile for wave height H = 12.94 cm and freeboard R_c = 0 cm.

F

Appendix: PIV setup details

PIV design rules
Four hydraulic heads are tested per physical model during the flow experiments. For each hydraulic head are different setups needed to perform PIV measurements. All setups must fulfil the following four design rules (Adrian & Westerweel, 2011).

- High image density: The number of tracer particles within an interrogation window (N_I) should be larger than 10: N_I > 10.
- In-plane pair loss: During the time between two frames (Δt) within a frame pair, particles could leave or enter the interrogation area (D_IxD_I). This in-plane loss is limited by the in-plane quarter rule: X_p < D_I/4.
- Out-plane pair loss: Particles could leave the light sheet during Δt and can be limited by Z < z_0 / 4. Where Z is the distance travelled perpendicular to the light sheet and z_0 is the thickness of the light sheet.
- Spatial gradients: local variation of the image displacement of the particles during Δt should be smaller than the image particle size d_τ. This can be limited by: $M_0 u_p \Delta t$ < d_τ. With M_0 as the magnification of the lens.

The possible combinations of different components for the setup are numerous. To design the right setup, the integral velocity-, length- and time scales of the flow can be estimated beforehand. Combining these with the characteristics of the other components will result in an estimate of the dimensions of the experimental setup. These setups with the expected flow conditions are presented in Table F.1 and F.2. The expected maximum and minimum flow velocities are presented respectively. Each setup per hydraulic head was the same per physical model.

The setup is tested to check if the design results are met. The corresponding output is presented in Table F.3 and F.4. These are calculated by using the following equations.

Assuming a lens with focal length f and a perpendicular distance from the lens to the light sheet y_0, the Gaussian lens law is met: $1/Y_0 + 1/y_0 = 1/f$. Where Y_0 is the image distance between the chip and the lens. The lateral magnification of the lens is defined as $M_0 = Y_0/y_0$. The corresponding location of the tracer particle ($\mathbf{x}_p$)(t) is mapped onto the image location $\mathbf{X}_p$(t) by using equation F.1 (Adrian & Westerweel, 2011).

$$\begin{pmatrix} X_p \\ Y_p \end{pmatrix} \cong M_0 \begin{pmatrix} x_p \\ y_p \end{pmatrix} \tag{F.1}$$

By using the same equation, but now for the field of view, the width (x_s) and height (y_s) can be approximated.

To ensure that the particles are in focus during the measurements, it is demanded that the depth of field is larger than the light sheet thickness z_0. This field of depth can be approximated by Equation F.2. Selecting equipment for appropriate values for $f^{\#}$ and M_0 must result in $\delta z > z_0$ (Adrian & Westerweel, 2011).

$$\delta z \cong 4(1 + \frac{1}{M_0})^2 f^{\#2} \lambda \tag{F.2}$$

$f^{\#}$ is the f-number of the lens and can be defined as $f^{\#} = f/D_a$, with D_a representing the aperture and λ the wavelength of the LED light sheet.

Besides the four PIV design rules, there are two additional design checks that must be used: the ratio between the particle image diameter and the pixel distance (d_τ/d_r) and the image blur parameter (β_{ib}). The ratio (d_τ/d_r) should be around the value of 1 (Adrian & Westerweel, 2011) and the image blur should be smaller than 2 (Bakker et al., 2019). Equations F.3 and F.4 are used to determine the particle image diameter and the diffraction-limited spot diameter. The d_a is the diameter of an aberrated image of a point, which is assumed to be negligibly small.

$$d_\tau = (M_0^2 d_p^2 + d_s^2 + d_a^2)^{1/2} \tag{F.3}$$

$$d_s = 2.44(1 + M_0) f^{\#} \lambda \tag{F.4}$$

The image blur parameter indicates when the particle travels a too large distance during the illumination time. This results in the particles on the image being elongated. This image blur effect is expressed by the particle image ratio (β_{ib}) and should be smaller than 2:

$$\beta_{ib} \frac{d_\tau + d_l}{d_{tau}} \tag{F.5}$$

$$d_l = M_0 u_p \tau_{ill} \tag{F.6}$$

The number of particles observed in an interrogation window is determined based on the discharge of the injection system and the corresponding particle concentration of the injection mixture. The discharge of the pump was 0.015 L/s with a corresponding particle concentration of 50 grams/L. Therefore, the injected mass was 0.75 gram/s. These particles spread out slowly over the width of the flume when they travel downstream. Approximately 10% of the injected particles are illuminated by the LED light source. Depending on the tested hydraulic head, the illuminated volume (V_{tot}) can be approximated. The size of the interrogation windows (D_I x D_I) is approximated when the M_0 is known. The entire width of the light sheet (z_0) is used to observe the particles. Therefore the number of particles is estimated by the following equation:

$$N = N_s * z_0 * D_I^2 \tag{F.7}$$

$$N_s = \frac{0.10 * m_p}{\rho_p V_p} * \frac{1}{V_{tot} * 1000} \tag{F.8}$$

The time between the two frames (Δt) is determined based on the 'In-plane pair loss rule', which states that the particles must not travel more than 1/4th of an interrogation window during Δt. As the windows are 32 pixels, the particles should travel 8 pixels maximum. However, the velocity at the crest is lower than the velocity at the toe and particles should always travel a certain number of pixels to measure their travelled distance. Therefore, a minimum travelled distance of 3 pixels was used to determine the delay time. So, the Δt is based on the predetermined assumed integral velocities in which the particles are travelling at least 3 pixels at the crest and a maximum of 8 pixels during the maximum flow velocities.

Table F.1: Flow experiments setup details for flow velocities at lowest position (maximum velocities)

COMPONENT	PROPERTIES	PARAMETER	H = 8.1 cm	H = 10.8 cm	H= 13.5 cm	H = 16.0 cm
CAMERA	resolution width [pix]		2448	2448	2448	2448
Oryx ORX-10GS-51S5M-C	resolution height [pix]		2048	2048	2048	2048
	pixel distance [µm]	d_r	3.45	3.45	3.45	3.45
	sensor size width [mm]	X_s	8.4	8.4	8.4	8.4
	sensor size height [mm]	Y_s	7.1	7.1	7.1	7.1
LENS	focal length [mm]	f	12.5	12.5	12.5	12.5
Fujinon TV Lens HF12.5SA-1	f# [-]	f-number	1.8	1.8	1.8	1.8
1:1.4/12.5mm	aperture [mm]	D_a	6.94	6.94	6.94	6.94
LIGHTSOURCE	light wave length [nm]	λ	530	530	530	530
LED DrewLear VLX2-500	illumination time [µs]	τ_{ill}	100	100	100	100
	light sheet thickness [mm]	z_0	6	6	6	6
	focal length [mm]	f_{led}	350	350	350	350
TRACER PARTICLES	avg. particle diameter [µm]	d_p	100	100	100	100
Vestosint 1101	mass density [kg/m3]	ρ_p	1060	1060	1060	1060
	particle volume [mm3]	V_p	5.24E-04	5.24E-04	5.24E-04	5.24E-04
	added mass particles [gr/s]	m_p	0.75	0.75	0.75	0.75
	Stokes number [-]	$St_p = \tau_p/\tau_0$	9.49E-05	1.01E-04	1.07E-04	1.13E-04
PIV PROCESSING	interrogation window size [pix]	D_i	32	32	32	32
MATlab Package PIVLab	overlap [%]	D_0	50	50	50	50
	trigger frequency [Hz]	f_{acq}	20	20	20	20
	time delay [µs]	Δt	1300	1100	950	800
SET UP DIMENSIONS	object distance [m]	z	1	1	1	1
	min. width of field of view [m]		0.535	0.535	0.535	0.535
	min. height of field of view [m]		0.445	0.445	0.445	0.445
	volume of complete set up light [m3]	V_{tot}	0.001733	0.00231	0.00278	0.00342
FLUID PROPERTIES	mass density [kg/m3]	ρ_f	998.2	998.2	998.2	998.2
	kinematic viscosity [m2/s]	v_f	1.05E-06	1.05E-06	1.05E-06	1.05E-06
FLOW CONDITIONS	integral in plane velocity scale [m/s]	u_0	1.6	1.7	1.8	1.9
	integral out of plane velocity scale [m/s]	v_0	0.2	0.2	0.2	0.2
	integral length scale [m]	l_0	0.55	0.55	0.55	0.55
	integral time scale [s]	τ_0	0.343	0.323	0.305	0.289
	Reynolds number [-]	$u_0 * l_0 / v_f$	8.35E+005	8.88E+05	9.40E+05	9.92E+05

Table F.2: Flow experiments setup details for flow velocities at crest position (lowest velocities)

COMPONENT	PROPERTIES	PARAMETER	H8.1	H10.8	H13.5	H16.0
CAMERA	resolution width [pix]		2448	2448	2448	2448
Oryx ORX-10GS-51S5M-C	resolution height [pix]		2048	2048	2048	2048
	pixel distance [µm]	d_r	3.45	3.45	3.45	3.45
	sensor size width [mm]	X_s	8.4	8.4	8.4	8.4
	sensor size height [mm]	Y_s	7.1	7.1	7.1	7.1
LENS	focal length [mm]	f	12.5	12.5	12.5	12.5
Fujinon TV Lens HF12.5SA-1	f# [-]	f-number	1.8	1.8	1.8	1.8
1:1.4/12.5mm	aperture [mm]	D_a	6.94	6.94	6.94	6.94
LIGHTSOURCE	light wave length [nm]	λ	530	530	530	530
LED DrewLear VLX2-500	illumination time [µs]	τ_{ill}	100	100	100	100
	light sheet thickness [mm]	dz_0	6	6	6	6
	focal length [mm]	f_{led}	350	350	350	350
TRACER PARTICLES	avg. particle diameter [µm]	d_p	100	100	100	100
Vestosint 1101	mass density [kg/m3]	ρ_p	1060	1060	1060	1060
	particle volume [mm3]	V_p	5.24E-004	5.24E-004	5.24E-004	5.24E-004
	added mass particles [gr/s]	m_p	0.75	0.75	0.75	0.75
	Stokes number [-]	$St_p = \tau_p/\tau_0$	4.33418E-05	4.98727E-05	5.58099E-05	6.05597E-05
PIV PROCESSING	interrogation window size [pix]	D_i	32	32	32	32
MATlab Package PIVLab	overlap [%]	D_0	50	50	50	50
	trigger frequency [Hz]	f_{acq}	20	20	20	20
	time delay [µs]	Δt	1300	1100	950	800
SET UP DIMENSIONS	object distance [m]	z	1	1	1	1
	min. width of field of view [m]		0.535	0.535	0.535	0.535
	min. height of field of view [m]		0.445	0.445	0.445	0.445
	volume of complete set up light [m3]	V_{tot}	0.001733	0.00231	0.00278	0.00342
FLUID PROPERTIES	mass density [kg/m3]	ρ_f	998.2	998.2	998.2	998.2
	kinematic viscosity [m2/s]	v_f	1.05E-006	1.05E-006	1.05E-006	1.05E-006
FLOW CONDITIONS	integral in plane velocity scale [m/s]	u_0	0.73	0.84	0.94	1.02
	integral out of plane velocity scale [m/s]	v_0	0.2	0.2	0.2	0.2
	integral length scale [m]	l_0	0.55	0.55	0.55	0.55
	integral time scale [s]	τ_0	0.753424658	0.654761905	0.585106383	0.539215686
	Reynolds number [-]	$u_0 * l_0 / v_f$	3.81E+005	4.39E+005	4.91E+005	5.33E+005

Table F.3: Output PIV requirements for maximum flow velocity

	PARAMETER	REQUIREMENT	H = 8.1 cm	H = 10.8 cm	H = 13 cm	H = 16 cm
IMAGE DIMENSIONS						
image distance [mm]	Y_0		12.66	12.66	12.66	12.66
lateral magnification [-]	M_0		0.01266	0.01266	0.01266	0.01266
field of view width [mm]	x_s		667	667	667	667
field of view height [mm]	y_s		558	558	558	558
depth of field [mm]	Δ_z		44	44	44	44
IMAGED PARTICLE						
diffraction limited spot diameter [µm]	d_s		2.4	2.4	2.4	2.4
image particle size [µm]	d_τ		2.7	2.7	2.7	2.7
ratio d_τ / d_r		$d_\tau / d_r \approx 1$	0.8	0.8	0.8	0.8
image particle length [µm]	d_l		2.0	2.2	2.3	2.4
image blur parameter [-]	β_{ib}	$\beta_{ib} < 2$	1.8	1.8	1.9	1.9
particle concentration [# /mm3]	N_s		0.08	0.06	0.05	0.04
PROCESSING						
interrogation window image size [mm]			8.7	8.7	8.7	8.7
vector spacing [mm/vector]	x_{vec}		4.4	4.4	4.4	4.4
PIV DESIGN RULES						
# particles per interrogation window	N_I	N>10	36	27	22	18
in plane motion [pix]	X_p	$X_p < 8$	7.6	6.9	6.3	5.6
out of plane motion [mm]	ΔZ_{max}	$\Delta Z_{max} < 6$	0.26	0.22	0.19	0.16
spatial gradient [µm]	Δu_p	$\Delta u_p < d_\tau$	2.6	2.4	2.2	1.9

Table F.4: Output PIV requirements for crest flow velocity

	PARAMETER	REQUIREMENT	H = 8.1 cm	H = 10.8 cm	H = 13 cm	H = 16 cm
IMAGE DIMENSIONS						
image distance [mm]	Y_0		12.66	12.66	12.66	12.66
lateral magnification [-]	M_0		0.01266	0.01266	0.01266	0.01266
field of view width [mm]	x_s		667	667	667	667
field of view height [mm]	y_s		558	558	558.18	558
depth of field [mm]	Δz		44	44	44	44
IMAGED PARTICLE						
diffraction limited spot diameter [µm]	d_s		2.36	2.36	2.36	2.36
image particle size [µm]	d_τ		2.7	2.7	2.7	2.7
ratio d_τ / d_r		$d_\tau / d_r \approx 1$	0.8	0.8	0.8	0.8
image particle length [µm]	d_l		0.9	1.1	1.2	1.3
image blur parameter [-]	β_{ib}	$\beta_{ib} < 2$	1.4	1.4	1.4	1.5
particle concentration [# /mm3]	N_s		0.08	0.06	0.05	0.04
PROCESSING						
interrogation window image size [mm]			8.7	8.7	8.7	8.7
vector spacing [mm/vector]	x_{vec}		4.4	4.4	4.4	4.4
PIV DESIGN RULES						
# particles per interrogation window	N_I	N > 10	35	26	22	18
in plane motion [pix]	X_p	$X_p < 8$	3.5	3.4	3.3	3.0
out of plane motion [mm]	ΔZ_{max}	$\Delta Z_{max} < 6$	0.26	0.22	0.19	0.16
spatial gradient [µm]	Δu_p	$\Delta u_p < d_\tau$	1.2	1.2	1.1	1.0

PIV camera-light signal

The light and the camera systems are triggered via a counter system to trigger the LED light sheet and the camera to capture the displacements of the particles. This signal is presented in Figure F.1. Three different signals are identified; Counter, Camera and Light. It starts with the Counter signal which counts the time of the predefined frame rate (f_{acq}) minus the illumination time (τ_{ill}) and delay time (Δt). When this time has been reached, the Counter signal drops and the Light signal starts. The LED light sheet gives a light pulse of duration τ_{ill}, waits Δt seconds and gives a second light pulse of τ_{ill}. During the drop of the Counter signal, the Camera signal drops during the delay time of the Light signal. The camera signal indicates when the camera lens is open and a frame is captured. Because the measurements are taken in a dark area, the frames only capture light from the LED light. The time the camera closes is marked by t_c and is set to 100 microseconds. So, the camera lens is open during the first light pulse, closes and opens when the second pulse is present. Because the camera closes between the two pulses, there are two frames which are used for one frame pair. To capture the next two frames, the camera lens closes after each $1/2f_{acq}$-t_c and two new frames can be captured.

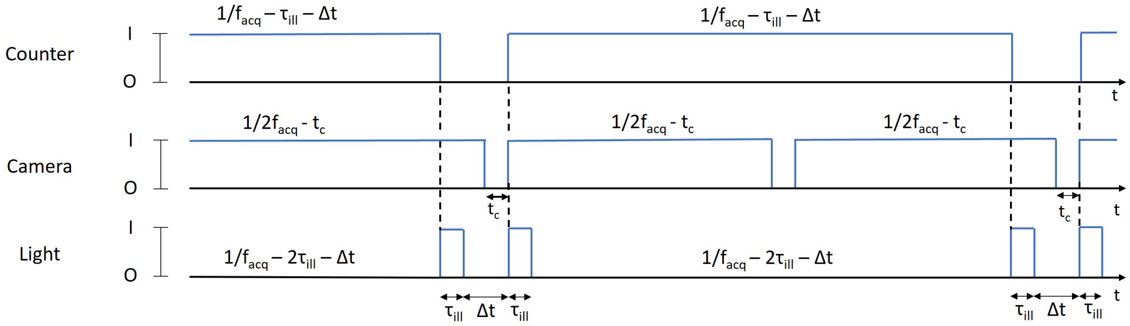

Figure F.1: PIV on/off signal for Counter, Camera and Light.

PIV calibration and reference points

Each physical model is different from the other and therefore the calibration is executed per model. This is also the case for the reference point per model. These known reference points are presented in Table F.5. Each reference point is positioned at the bottom right corner of the checkerboard that was used for the calibration of the PIV measurements. This checkerboard has squares of 10 mm x 10 mm. Before the measurements on a physical model, the front of the checkerboard was positioned in the light sheet in a filled flume and a single picture was taken. This picture was used as a calibration picture for the corresponding physical model and is shown in Figure F.2. The reference point was measured before the measurements (x_1, z_1) and after the measurements (x_2, z_2) to check if the model was located at the same position. All reference points were measured from the bottom centre of each model.

Table F.5: Reference points per model before and after PIV measurements

Model	x_1 (cm)	x_2 (cm)	z_1 (cm)	z_2 (cm)
1	11.8	11.7	16.9	17
2	9.9	9.8	17.2	17.2
3	12.2	12.3	17.3	17.3
4	26.4	26.4	13.3	13.3

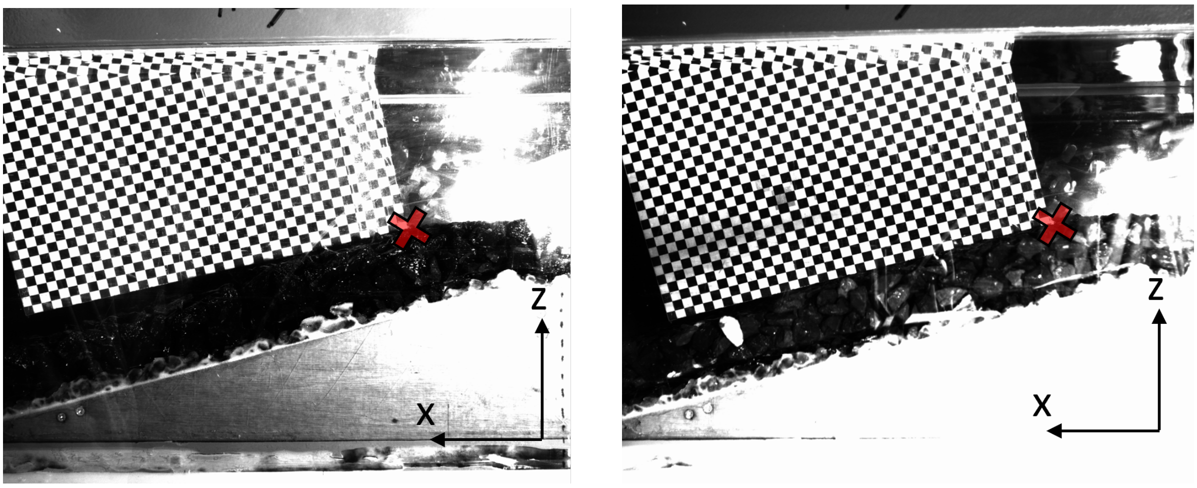

(a) Calibration picture model 1

(b) Calibration picture model 2

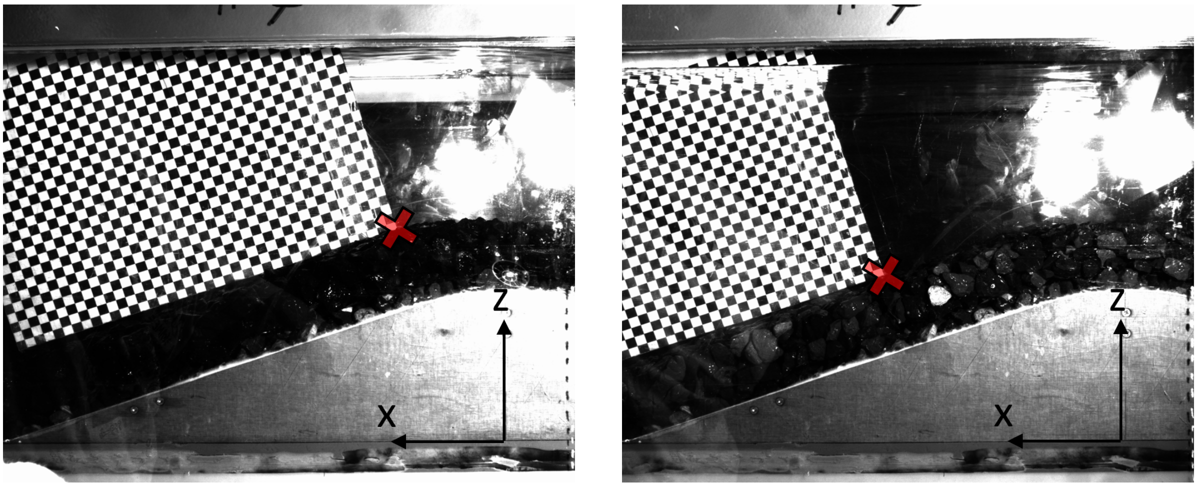

(c) Calibration picture model 3

(d) Calibration picture model 4

Figure F.2: Calibration pictures for models 1 to 4 during the flow experiments with corresponding reference point marked by the red cross

G

Appendix: SfM process and accuracy

The damage measurements are performed via Structure from Motion principles (SfM). All models are made by taking a series of at least 21 pictures using the Canon EOS 2000D camera. The EFS18-55 mm lens was used and fixed at a focal length of 29mm in combination with an aperture of F/22. This resulted in an overlap of at least 50%. Pictures were taken at ISO 1600 with a shutter speed of 1/10th of a second.

To increase and also to check the accuracy of the SfM models, ground control points (GCP) are placed around the physical model. The position of these GCPs is known and presented in Table G.1. The GCPs are placed in pairs of two with a known distance and are called Scale bars. All scale bars are 90 mm. The known GCPs positions and known Scale bar distances are used to increase the accuracy of the models and to check the error of the models. The errors are presented in Table G.2. On average, the GCP positions have a 0.17 pixel error, which is equal to 0.582 mm. The Scale bar error is on average 0.685 mm. Therefore, it can be concluded that solely based on the scale bar, the accuracy of the models is 99.2%.

To obtain this accuracy the following steps were applied in Agisoft MetaShape during the construction of the 3D models. For each initial and damage 3D model are the taken images imported into Agisoft as a so-called ’Chunk’ and the image quality is estimated by the program. When the quality of an image is lower than 0.5, it is recommended to remove the image. Therefore, the number of images per model differs. The high-quality group of pictures are aligned with accuracy settings ’Medium’, key point limit of 60.000 and tie point limit of 4.000. This will result in a ’Sparse point cloud’ and all the unique features of the physical are identified. Next, the GCPs are identified and the pre-defined locations and scale bars are imported. This increases the accuracy of the Sparse point cloud. To increase the accuracy even further the following three filters were applied. It is filtered by Reconstruction Uncertainty (uncertainty based on triangulation), Projection accuracy and Reprojection Error (difference between points’ calculated 3D position and their marked position on images). In practice, the filtering results in removing 90% of the Spare point cloud. After the filtering, the final dense point cloud is constructed. The average number of data points per cm^2 per model is presented in Table G.2.

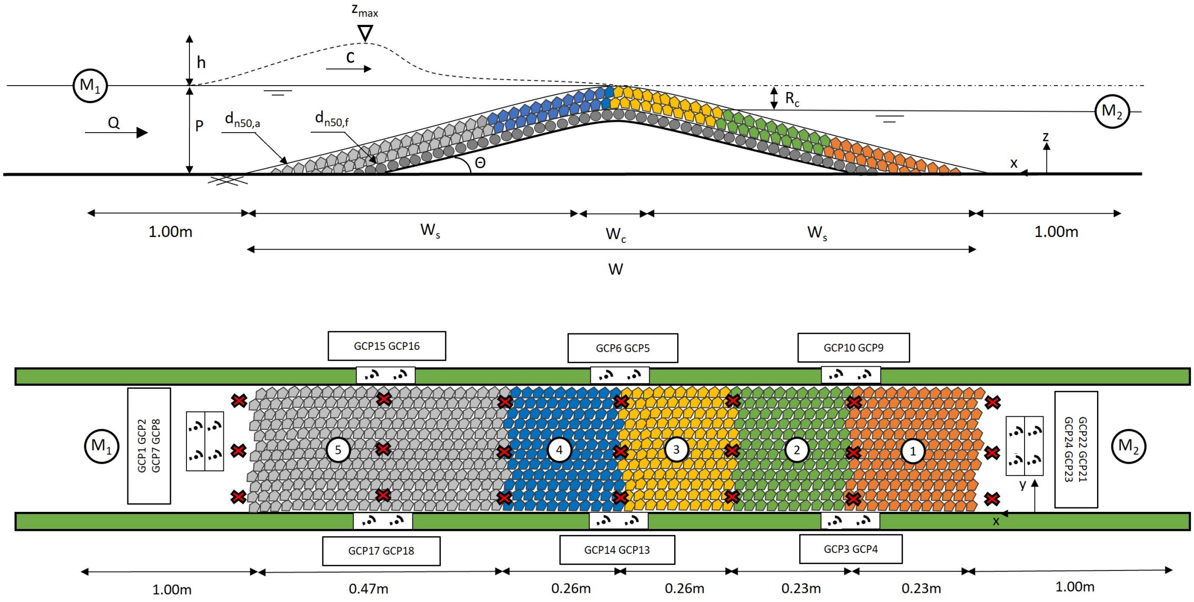

Figure G.1: Side view of the test setup in the flume during the damage experiment. Top: side view of physical model 5 with the assigned colours at different locations. Bottom: Top view with an overview of the Ground Control Points (GCP) and camera positions (red crosses).

Table G.1: Positions of GCPs during damage experiment

GCP	x (mm)	y (mm)	z (mm)
1	1665	155	0
2	1665	245	0
3	431	-37	433
4	340	-37	433
5	792	435	436
6	882	435	436
7	1665	155	0
8	1665	245	0
9	342	434	434
10	432	435	433
13	790	-38	427
14	880	-37	427
15	1324	435	434
16	1234	435	434
17	1324	-35	434
18	1234	-35	434
21	0	155	0
22	0	245	0
23	27	155	0
24	27	245	0

Table G.2: Accuracy of SfM models during damage experiment

h_{target} (cm)	R_c (cm)	$z_{max,meas}$ (cm)	T_{meas} (sec)	T_{st} (sec)	Q_{max} (L/s)	Model	# pictures	GCP Error (pix)	GCP Error (mm)	Scale bar Error (mm)	Points total	points/cm^2
3.6	10.9	3.75	23.8	8.4	13.32	initial	28	0.405	0.591	0.709	9.82E+06	1.44E+03
						damage	26	0.083	0.568	0.678	8.97E+06	1.32E+03
5.4	10.9	6.89	24	6.8	33.2	initial	26	0.331	0.564	0.742	8.77E+06	1.29E+03
						damage	28	0.667	0.578	0.754	9.99E+06	1.47E+03
10.8	10.9	10.55	25.4	6.6	49.92	initial	29	0.242	0.572	0.734	9.37E+06	1.38E+03
						damage	29	0.342	0.574	0.127	9.27E+06	1.36E+03
3.6	8.2	3.27	20.6	7	16.69	initial	34	0.171	0.605	0.766	9.40E+06	1.38E+03
						damage	35	0.434	0.641	0.843	9.01E+06	1.33E+03
5.4	8.2	7.2	24.2	5.8	33.2	initial	23	0.171	0.847	0.104	8.73E+06	1.28E+03
						damage	25	0.106	0.55	0.792	8.15E+06	1.20E+03
5.4	8.2	6.09	27.2	6.6	29.9	initial	25	0.366	0.586	0.779	8.54E+06	1.26E+03
						damage	24	0.403	0.546	0.707	8.40E+06	1.23E+03
8.1	8.2	9.84	25.6	6.8	48.32	initial	23	0.526	0.612	0.718	8.59E+06	1.26E+03
						damage	23	0.521	0.599	0.756	9.07E+06	1.33E+03
10.8	8.2	11.86	27.4	6	53.74	initial	27	0.146	0.592	0.763	8.69E+06	1.28E+03
						damage	30	0.056	0.581	0.676	9.94E+06	1.46E+03
3.6	5.5	3.48	27.2	5.8	14.27	initial	32	0.157	0.608	0.894	6.18E+06	9.09E+02
						damage	33	0.126	0.58	0.855	6.26E+06	9.20E+02
3.6	5.5	4.62	21.4	5.8	22.4	initial	30	0.13	0.669	0.744	8.80E+06	1.29E+03
						damage	32	0.08	0.547	0.537	8.79E+06	1.29E+03
5.4	5.5	6.77	21	7	32.22	initial	21	0.097	0.639	0.767	7.02E+06	1.03E+03
						damage	24	0.119	0.581	0.665	7.31E+06	1.07E+03
8.1	5.5	10.61	24.6	5.6	51.29	initial	25	0.06	0.563	0.73	8.25E+06	1.21E+03
						damage	26	0.059	0.558	0.667	8.42E+06	1.24E+03
8.1	5.5	9.65	24.8	5.8	42.89	initial	24	0.057	0.567	0.668	7.70E+06	1.13E+03
						damage	23	0.155	0.562	0.648	7.76E+06	1.14E+03
10.8	5.5	12.4	23.6	7.4	63.85	initial	26	0.062	0.57	0.744	8.02E+06	1.18E+03
						damage	25	0.083	0.619	0.607	8.78E+06	1.29E+03
3.6	2.7	3.86	25	5.6	16.5	initial	32	0.095	0.585	0.638	9.70E+06	1.43E+03
						damage	31	0.094	0.584	0.713	8.55E+06	1.26E+03
5.4	2.7	6.25	27.4	5.6	26.74	initial	30	0.124	0.571	0.845	6.30E+06	9.27E+02
						damage	30	0.153	0.58	0.839	6.07E+06	8.92E+02
8.1	2.7	8.28	26.2	6.2	39.17	initial	22	0.055	0.548	0.674	7.54E+06	1.11E+03
						damage	25	0.09	0.552	0.725	7.55E+06	1.11E+03
10.8	2.7	11.23	24.6	6.2	53.98	initial	25	0.126	0.567	0.619	7.68E+06	1.13E+03
						damage	25	0.143	0.593	0.757	8.09E+06	1.19E+03
12.5	2.7	12.55	26.4	5.8	59.47	initial	24	0.121	0.589	0.705	8.30E+06	1.22E+03
						damage	22	0.091	0.564	0.678	7.45E+06	1.10E+03
12.5	2.7	11.56	25.2	5.8	53.03	initial	22	0.049	0.532	0.657	7.00E+06	1.03E+03
						damage	26	0.063	0.559	0.791	7.45E+06	1.09E+03
14.6	2.7	13.15	27.6	6.4	63.38	initial	24	0.165	0.57	0.682	7.86E+06	1.16E+03
						damage	28	0.128	0.557	0.742	8.10E+06	1.19E+03
10.8	0	11.01	26.4	5.6	47.89	initial	25	0.08	0.526	0.603	7.69E+06	1.13E+03
						damage	25	0.111	0.537	0.711	7.88E+06	1.16E+03
10.8	0	10.64	26.8	4.6	46.28	initial	24	0.131	0.565	0.659	7.84E+06	1.15E+03
						damage	23	0.069	0.526	0.568	7.58E+06	1.11E+03
12.5	0	12.94	25.8	6	58.75	initial	22	0.061	0.61	0.612	7.51E+06	1.10E+03
						damage	24	0.096	0.543	0.53	7.55E+06	1.11E+03

H

Appendix: PIV results remarks

PIV results for $h \leq 5.4$ cm

During the flow experiments were some difficulties experienced by measuring the flow velocities for hydraulic heads $h < 5.4$ cm. The hydraulic heads used for the flow velocity equation were 8.1 to 16.0 cm. The hydraulic head of 5.4 cm showed significant inaccuracies (see Figure 5.6 in Section 5.4) for flow velocities lower at the downward slope of the physical model.

By analysing the PIV frames taken for $h = 5.4$ cm, it is observed that the upper part of the overflowing water body does not show any tracer particles. Meanwhile, the lower part does show tracer particles indicating that light shines through the water body. This area increases when the water is going lower along the downward slope. This phenomenon was also observed for $h = 3.6$ cm and therefore not mentioned in the report. However, via visual observation, it is confirmed that there are tracer particles over the entire depth.

The cause of this problem can be explained due to the irregularities of the water's surface at smaller water depths. These irregularities start approximately when the water level is smaller than 4 centimetres in combination with a large roughness. This is a problem because the water surface should be flat in order to be penetrated by the LED light sheet and to be captured by the PIV camera. When the water surface isn't flat any more, the LED shines through the water but is refracted away from the camera. Resulting in a dark upper part of the overflowing water, but an illuminated part at the lower part. This phenomenon is schematically shown in Figure H.1.

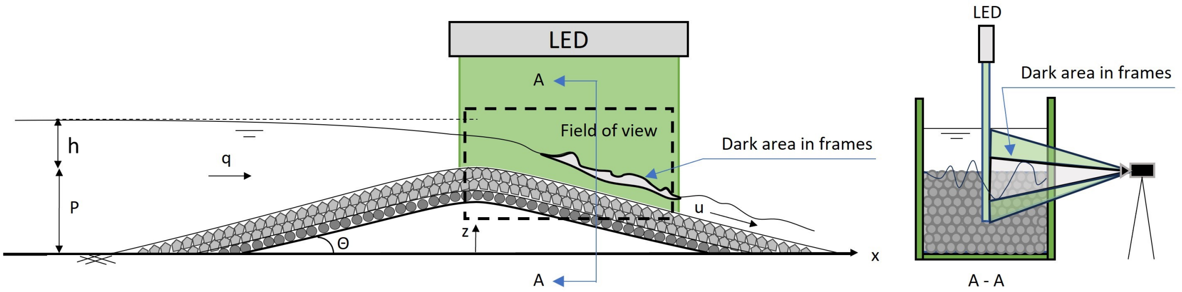

Figure H.1: Side view of the test setup in the flume during the flow and corresponding dark area within the illuminated field of view.

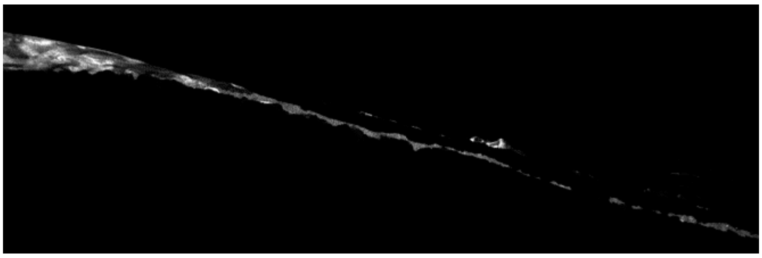

Figure H.2: Raw frame of the field of view during PIV measurement of h = 3.6 cm. Flow over the structure at the lower part shows a dark area with no particles.

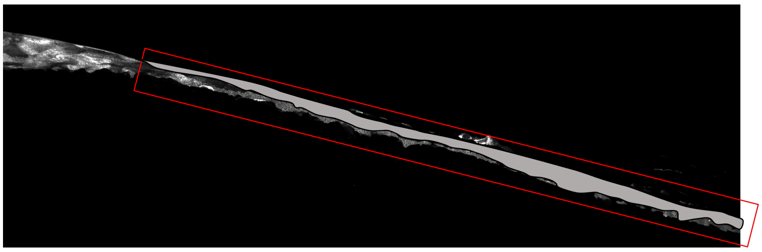

Figure H.3: Same raw frame as Figure H.2 of the field of view during PIV measurement of h = 3.6 cm. The dark area is marked.

Figure H.4: Same raw frame of the field of view during PIV measurement of h = 5.4 cm. Flow over the structure at the lower part shows a dark area with no particles.

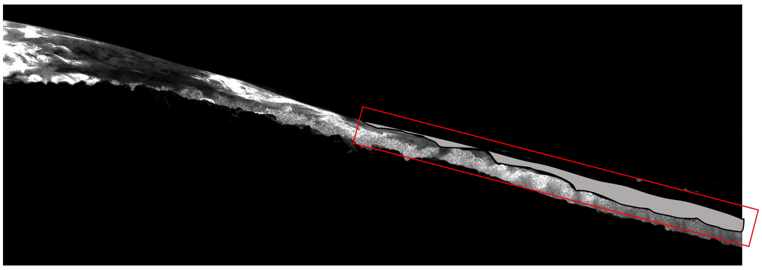

Figure H.5: Same raw frame as Figure H.4 of the field of view during PIV measurement of h = 5.4 cm. The dark area is marked.

PIV flow velocity drops remark

For the PIV measurements with h > 5.4 cm are all frames analysed to determine the flow velocity. By analysing these frames, at some time moments was a passing drop in velocity noticed. These passing velocity drops were only a few centimetres in width and covered a small part of the water depth. Figure H.6 presents two analysed frames at different time moments during the PIV measurement for h = 10.8 cm. The dashed red circle marks the drop in flow velocity at the water surface. Figure a at both frame pairs shows the velocity magnitude and Figure d presents the corresponding raw PIV frame. For both frame pairs is observed that the drop in flow velocity is caused by an increase in concentration of particles which are grouped together. These groups were unable to be analysed with the PIV software and flow velocities were interpolated leading to a lower flow velocity within the group. The grouped particles are expected to be caused due to the particle injection system. The injection system was placed at the toe of the structure and the particles were not yet fully mixed throughout the entire width of the flume. Nevertheless, these drops in velocities occurred only once every several seconds and are not expected to influence the depth- and time-averaged flow velocities significantly.

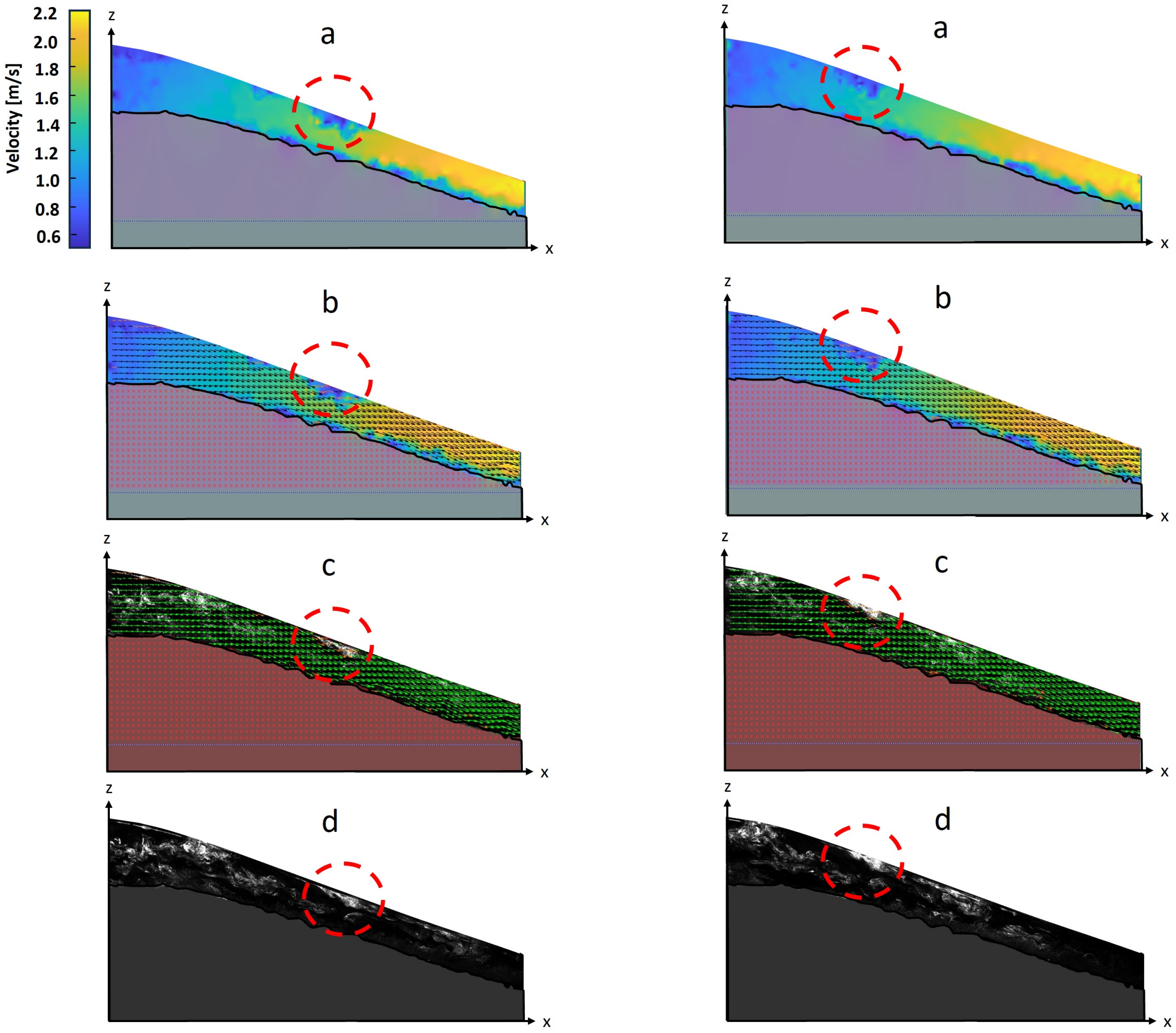

(a) Drop in flow velocity frame pair A

(b) Drop in flow velocity frame pair B

Figure H.6: Two frames at different time moments during PIV measurement for test h = 10.8 cm. a) Flow velocity field with a drop in velocity at the water surface and marked by red dashed circle. b) Same flow velocity field with flow velocity vectors. c) Raw PIV frame with only flow velocity vectors. d) Raw PIV frame without any flow velocities or directions.